Simulation of Plasmonic Nanoparticles in Thin Film Solar Cells

Dissertation zur Erlangung des Grades

eines Doktors der Naturwissenschaften (Dr. rer. nat.)

am Fachbereich Physik

der Freien Universität Berlin

von

Phillip Manley

Berlin, Juli 2016

Supervisor: Prof. Dr. Martina Schmid

Second examiner: Prof. Dr. Frank Schmidt

Datum der Disputation: 23.05.2016

Selbständigkeitserklärung

Hiermit versichere ich, die vorliegende Arbeit selbstständig und ausschließlich unter Benutzung der angegebenen Quellen und Hilfsmittel verfasst zu haben.

Ich erkläre weiterhin, dass die vorliegende Arbeit nicht im Rahmen eines früheren Promotionsverfahrens an einer anderen Stelle eingereicht worden ist.

Unterschrift: ______________________________

Datum: ______________________________

Abstract

Plasmonic nanoparticles are a promising technology for increasing the absorption in thin film solar cells. This thesis uses optical simulations to understand and optimise the role that plasmonics can play in thin film solar cells.

The basics of plasmonics may be covered using the analytical Mie theory which describes a plane wave interacting with a spherical object. This can be extended to include core-shell spherical objects. A key finding is that if the shell refractive index is higher than the surrounding medium refractive index, the plasmonic scattering and near field will be enhanced compared to shells with a lower refractive index.

In order to investigate more complex geometries the finite element method is introduced. In particular the method is used to simulate arrays of particles on a substrate to build the link between simulation and experiment. Simulations of large area arrays are very computationally expensive, therefore statistical averaging of single particle responses is performed. Using this method the experimental response of a particle array was able to be reproduced in simulations.

Ultra-thin film solar cells are then introduced and some of the issues surrounding these devices are investigated via the scattering matrix method. It is shown that moving away from a metallic back contact to a transparent contact with a separated metallic back reflector increases the absorption in the absorbing layer.

Having studied both plasmonics and ultra-thin film solar cells in isolation, they are then combined firstly using the finite element method. The effect of particle placement within the device structure is investigated. The result is that the best performance enhancement comes from particles integrated directly inside the absorbing layer.

Finally the previous methods of Mie theory for particle simulations and scattering matrix for layered stack simulations are combined to create a coupled method capable of rapid simulation of devices with integrated plasmonic nanoparticles. This model is then used to assess many different device structures with the optimum being found for Ag core / AlSb shell nanoparticles integrated into the absorbing layer of a device with a transparent back contact and an incoherent Ag back reflector. This ultra-thin device is able to reach 93% of the current of a conventional thin film while only using 20% of the absorber material.

Plasmonische Nanoteilchen sind eine vielversprechende Technologie für die Erhöhung der Absorption bei Dünnschichtsolarzellen. Diese Dissertation verwendet optische Simulationen um die Rolle von Plasmonen für Dünnschichtsolarzellen zu verstehen und zu optimieren.

Die Grundlagen der Plasmonik können mit der analytischen Mie-Theorie erfasst werden, die die Wechselwirkung zwischen einer ebenen Welle und einer Kugel beschreibt. Die Theorie kann auch auf Kern-Hülle-Teilchen erweitert werden. Ein zentraler Befund ist, dass bei einer Hülle mit einem Brechungsindex, der höher als der des umgebenden Mediums ist, die Streuung und das Nahfeld im Vergleich zu einer Hülle mit einem niedrigeren Brechungsindex erhöht sind.

Um komplexere Geometrien zu untersuchen wird die Finite-Elemente-Methode eingeführt. Die Methode wird eingesetzt um Teilchenverteilungen auf einem Substrat zu simulieren, um eine Verbindung zwischen Simulationen und Experimenten aufzubauen. Simulationen von großen Flächen sind rechnerisch sehr teuer, deshalb wird eine statistische Mittelung von Einzelpartikel-Reaktionen verwendet. Durch diese Methode konnte die experimentelle Reaktion einer Teilchenverteilung mit Simulationen wiedergegeben werden.

Ultradünnschichtsolarzellen werden vorgestellt und einige die Solarzellen betreffenden Probleme werden mit der Streumatrixmethode untersucht. Es wird gezeigt, dass der Wechsel von einem metallischen Rückkontakt zu einem transparenten Rückkontakt mit einem zusätzlichen metallischen Rückreflektor die Absorption der Absorberschicht erhöht.

Nachdem die Plasmonik und Ultradünnschichtsolarzellen isoliert betrachtet wurden, werden sie dann zuerst in der Finite-Elemente-Methode kombiniert. Die Wirkung der Teilchenstellung innerhalb der Solarzellenstruktur wird untersucht. Das Ergebnis ist, dass die stärkste Leistungsverbesserung durch in der Absorberschicht integrierte Teilchen erreicht wird.

Schließlich werden die vorherigen Methoden der Mie-Theorie für Teilchensimulationen und die Streumatrixmethode für Simulationen von geschichteten Stapeln kombiniert, um eine Methode zu entwickeln, die schnelle Simulationen von Solarzellen mit integrierten plasmonischen Nanoteilchen ermöglicht. Dieses Modell wird dann genutzt, um viele unterschiedliche Solarzellenstrukturen zu untersuchen. Es wurde eine optimale Struktur gefunden, die aus in die Absorberschicht integrierten Nanoteilchen mit einem Ag-Kern / einer AlSb-Hülle und einem transparenten Rückkontakt mit einem inkohärenten Ag-Rückreflektor besteht. Diese Ultradünnschichtsolarzelle erreicht 93 Prozent der Stromstärke eines gewöhnlichen Dünnfilms und nutzt dabei nur 20 Prozent des Absorbermaterials.

Acknowledgements

I would like to take this opportunity to thank my supervisor Martina Schmid for giving me the opportunity to conduct my PhD at the Helmholtz-Zentrum Berlin and for her continual support and interest in my work. Additionally I want to thank the entire NanooptiX group for their support and help throughout the last three years and for creating a very enjoyable working environment. In particular Guanchao Yin for providing many experimental results and for many interesting discussions on the topics of light management and solar cells. I am also very thankful for the great many experimental results of particle arrays obtained by Patrick Andrä and Min Song. I am also thankful for the funding from the Helmholtz Association for the Young Investigator group VH-NG-928 within the Initiative and Networking fund. I would also like to thank the BerOSE Joint lab for providing support for this work.

During the last three years I have also been a member of the computational nano-optics group at the Zuse Institue Berlin. Firstly I would like to thank Frank Schmidt for giving me the opportunity to work in the group and for teaching me the fundamentals of the finite element method. The entire group at ZIB has been a constant source of help and support and for that I would like to sincerely thank everyone involved. Particularly the support of Martin Hammerschmidt and Daniel Lockau for teaching me everything about the practicalities of the finite element method and for an enjoyable working environment in our office.

I would like to thank my family for their unreserved support over the years. Lastly I would like to thank Steph for her constant support, encouragement and care.

Contents

List of Figures

Abbreviations

Abs	Absorption
BC	Back Contact
BR	Back Reflector
CIGSe	Cu(In$_x$Ga$_{1-x}$)Se
EQE	External Quantum Efficiency
Exp	Experimental
Ext	Extinction
FEM	Finite Element Method
IR	infrared
ITO	In:SnO
Mie	Mie Theory
Nf	Near Field
NP	Nanoparticle
LSPR	Localised Surface Plasmon Resonance
PML	Perfectly Matched Layer
P	Plasma
rms	Root Mean Squared
Sca	Scattering
SC	Short Circuit
SEM	Scanning Electron Microscopy
Sim	Simulated
SM	Scattering Matrix
SPP	Surface Plasmon Polariton
UV	Ultra Violet

Symbols

a_n	Electric Mie Coefficient	
b_n	Magnetic Mie Coefficient	
$\mathbf{c}^{+,-}$	Amplitude of Waves	
A	Absorption	%
$\mathbf{B}$	Magnetic Induction Field	Vsm^{-2}
C	Cross Section	m^2
c	Speed of Light	ms^{-1}
$\mathbf{D}$	Electric Displacement Field	Cm^{-2}
$\hat{\mathbf{e}}$	Unit Vector	
$\mathbf{E}$	Electric Field	Vm^{-1}
$h_n^{1,2}$	Spherical Hankel Function Type 1 & 2	
h	Plank Constant	$\mathrm{m}^2\mathrm{kgs}^{-1}$
$\mathbf{H}$	Magnetic Field	Am^{-1}
$\tilde{\mathbf{H}}$	Normalised Magnetic Field	
i	Imaginary Unit	
I	Intensity	$(\mathrm{Vm}^{-1})^2$
j_n	Spherical Bessel Function Type 1	
J	Current Density	mAcm^{-2}
k	Refractive Index (imaginary part)	
k	Wavenumber	nm^{-1}
m	Relative Refractive Index	
$\mathbf{M}$	Electric Vector Harmonic	
$\mathbf{N}$	Magnetic Vector Harmonic	
n	Refractive Index (real part)	
L	Operator	

P_n^m	Associated Legendre Polynomials	
$\mathbf{P}$	Polarisation	Cm^{-2}
q	Electric Charge	C
Q	Normalised Cross Section	
r	Amplitude Reflection Coefficient	
R	Reflection	%
$\hat{S_{ij}}$	Scattering Matrix	
t	Layer Thickness	nm
T	Transmission	%
u	Vector	
V	Volume	m^3
$\hat{V}$	Magnetic Eigenvector Matrix	
$\hat{W}$	Electric Eigenvector Matrix	
v	Vector	
x	Size Parameter	
y_n	Spherical Bessel Function Type 2	
δ	Delta Function	
ϵ	Permittivity	Fm^{-1}
ξ_n	Riccati-Bessel Function	
μ	Permeability	Am^{-1}
λ	Wavelength	nm
$\hat{\lambda}$	Eigenvalue Matrix	
ρ	Charge Density	Cm^{-3}
σ	RMS Surface Roughness	nm
ψ	Scalar Wave Solution	
ψ_n	Riccati-Bessel Function	
ω	Angular Frequency	rads^{-1}
γ	Damping Frequency	rads^{-1}
Φ	Test Function	
$\Phi(\lambda)$	Solar Flux	Wm^{-2}nm^{-1}

Dedicated to my Father

Chapter 1

Introduction

One of the biggest challenges that the human race faces is that of energy production. Generating useful forms of energy is the basis of civilisation; when Prometheus created mankind he gifted us fire, energy in its purest form, that we might elevate our status above that of beasts. This myth has persisted in our cultural consciousness because of the fundamental role that energy plays in everything that we do. In modern society it is easy to forget, but without exploitation of energy we would not have food, warmth, shelter, society, art or even love. In short without energy, we would not be human.

But as Prometheus learnt, energy can also be dangerous. While he was punished by the gods for releasing the gift of fire, we mere mortals punish ourselves and our future

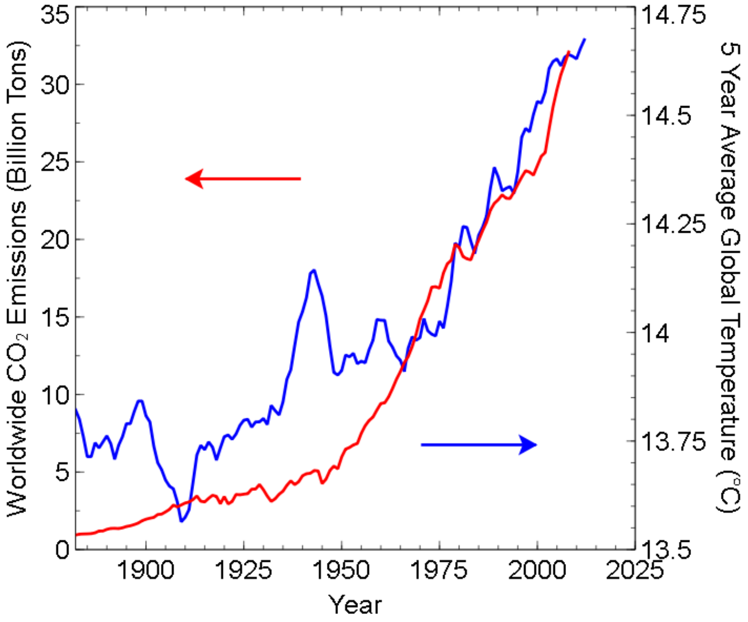

FIGURE 1.1: The worldwide CO$_2$ emissions due to human activities (red) and the 5 year rolling average global surface temperature (blue).

generations with current forms of energy production. Fossil fuel burning and the associated release of carbon dioxide into the atmosphere has unequivocally been shown to cause global warming. Figure 1.1 shows the global CO_2 emissions due to human activities [1], which has been exponentially increasing in the modern era. In the same time period the global average surface temperature [2] has increased at an astounding rate. Climate science has ruled out other contributing factors as being the dominant source of this global temperature increase, we are left with only one conclusion: our energy production is literally costing us the Earth.

The solution to this problem cannot come from any one course of action. The problem is so multifaceted that it must be dealt with in all areas of society. Having said that, turning away from fossil fuels for energy production towards a clean form of energy would certainly help to reduce carbon emissions. Carbonless energy sources essentially fall into two main categories, nuclear energy and renewable energy. Nuclear fission has been employed to produce energy since the 1950's, despite the lack of carbon production this technology suffers from fundamental problems which limit its use as a basis for our energy supply. Nuclear fission produces dangerous radioactive waste with a half life of millions of years which is difficult if not impossible to store in a safe way. Furthermore the potential for a catastrophic failure is much higher with this technology than for others, the recent tragedy in Fukushima being a prime example.

The methods for large scale energy production listed so far have all involved extracting something from the Earth, be it coal, oil, gas or uranium, and then consuming that resource for energy production. All of these sources are practically speaking finite ones, one day they will run out. Although the production of fossil fuels will continue as long as there is life on Earth, the rate at which they are created is so far below the rate of usage as to make it almost nonexistent. If we instead turn our attention away from the ground beneath us to the sky above, we may find an energy source which is practically infinite. The sun provides an average 1000 W of power to each square meter of the Earth's surface. This energy has been used by humans to grow crops since the beginning of the agricultural era. Moreover, all complex life on Earth ultimately draws energy from the sun via photosynthesis. This immense source of power is extremely underutilised, taking the surface area of the Earth into account, the total power supplied to Earth is 173,000 TW, which completely dwarfs the current world power consumption of 17.7 TW averaged over the year. This means that if only a small fraction of this power can be utilised, it would comfortably fulfill our energy needs. Figure 1.2 shows the spatial distribution of the solar irradiance on the Earth's surface including the day-night cycle and the effect of cloud cover, averaged over three years. If the land areas highlighted with black circles were completely covered with photovoltaics with a mere 8% energy conversion efficiency, they would produce 18 TW of electrical power, more than the

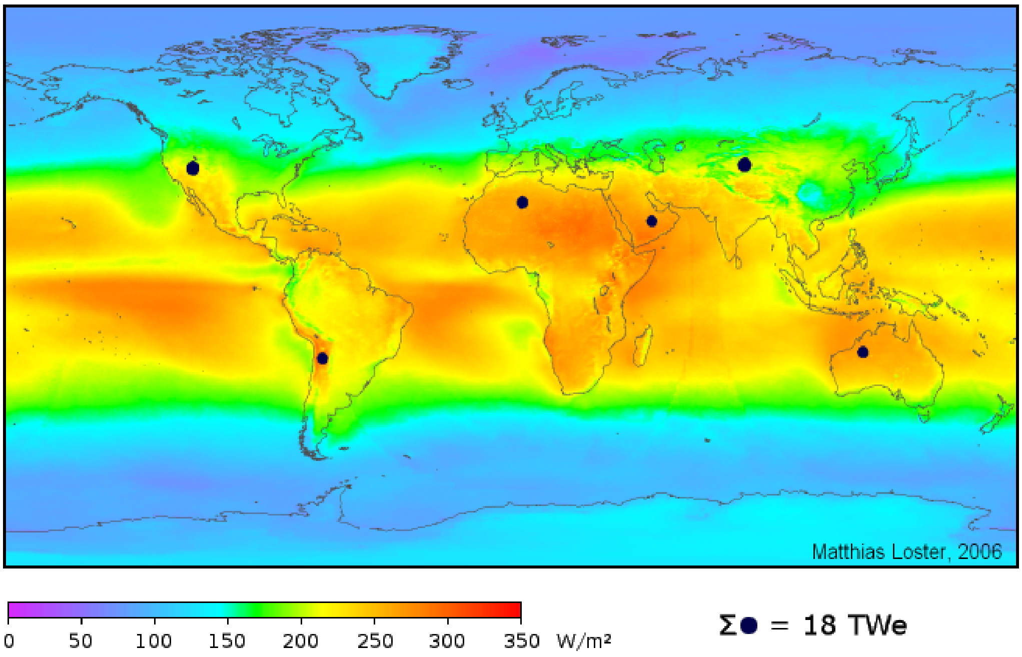

FIGURE 1.2: The spatial distribution of solar irradiance at the Earth's surface taking into account the day night cycle and cloud cover, averaged over three years. The black dots represent the fraction of land that could be covered in 8% efficient solar cells in order to supply the world energy demand. Image courtesy of Matthias Loster.

world power consumption. In real terms energy production from solar energy would not be concentrated into just six power plants worldwide. In fact one of the advantages of solar energy is that large power plants are not required, solar panels distributed on residential rooftops can significantly contribute to the world energy supply.

Drawbacks to solar energy exist; the limitation of the day-night cycle, seasonal variations in irradiance and the ability to only generate electricity are major hurdles. However many solutions to these problems already exist and are being actively developed. Energy storage via flywheels, supercapacitors or conversion to hydrogen are just some of the options available. Other forms of renewable energy are able to contribute to the energy supply, however none of them have the same potential in terms of possible energy production as that of solar, even though other forms such as wind currently produce more renewable energy than solar. Figure 1.2 already proves that with current technology a solar revolution could occur, the principle roadblock is purely an economic one. Although solar will become cheaper than conventional energy sources in the long term, in the here and now solar energy still has to compete with the likes of coal, gas and oil. In order to make solar energy competitive, we wish to produce solar cells with higher efficiencies at lower costs.

Although different technologies exist for producing solar energy, in almost all cases a key trade-off to be made is between the optical and electric properties of the device. In terms of optical properties, even a very poorly absorbing material could come close to complete absorption if it is thick enough. However as we shall see, absorbing light is the first step, the electrons and holes generated from the absorption must also be electrically collected. Due to this a device is limited in the thickness that can be used in order to be able to collect the generated carriers. Improving the electrical properties in order to be able to increase the thickness is generally very difficult to achieve. Therefore the only remaining solution is to increase the absorption in the layer. To this end we propose the use of novel optical designs to trap light inside the absorbing layer thereby increasing the absorption.

That is where the topic of this thesis comes in, here we analyse the potential for plasmonics as a light management technique. This will be conducted by simulating the performance of solar cells with integrated plasmonic concepts.

The thesis is laid out in the following manner. The second chapter reviews the literature present on light trapping as a concept, the conclusion to this will motivate the focus on plasmonics as a light trapping concept. The chapters from chapter three onwards follow a distinct patten, the odd chapters focusing on theoretical concepts while the even chapters show applications of the theoretical frameworks presented in the previous chapter.

Chapter 3 introduces Mie theory as a framework for simulating the light interaction with single spherical nanoparticles. This leads to the investigation of different material comparisons in chapter 4, in particular the optimum implementation of plasmonic core / dielectric shell type particles which could be key for successful device integration. Since metallic particles usually need to be electrically and chemically isolated from the device a dielectric shell should be incorporated. Dielectric materials which have a higher and lower refractive index than the surrounding material are compared, with the result that a shell with a refractive index higher than the surrounding will enhance the plasmonic resonance compared to shells with a lower refractive index. This result informs the choice of particle geometry and material choice in later chapters.

We then expand the toolbox of methods for simulating plasmonics to including the finite element method in chapter 5. This can then be used to simulate different geometries of single particles and also two particle interactions and arrays of particles in chapter 6. This chapter builds the link between the plasmonic simulations and experimental measurements. We compare measurements of reflection, transmission and absorption for Ag nanoparticle arrays on glass substrates to the simulated values. Since large arrays of particles are very computationally expensive we turn to using a statistical average of different single particle simulations. When including the effect of multiple reflections inside the glass substrate, the simulations are shown to be in good agreement with the experimental data.

Having developed a strong basis in the area of plasmonics we move to thin and ultra-thin film solar cells, first presenting the scattering matrix method for simulating layered media in chapter 7. This is then used to analyse and optimise ultra-thin film chalcopyrite solar cells without the addition of nanoparticles in chapter 8. The parasitic absorption in the Mo back contact is identified as a key source of loss, therefore simulations are introduced to verify if changing the back contact to a transparent conducting oxide and a separate back reflector can reduce the optical losses. This can be implemented in a coherent way in which there is only a thin film between the solar cell device and the back reflector, or in an incoherent way if the back reflector is separated by a thick glass substrate. Although the coherent integration might possibly provide a higher absorption benefit due to certain resonances, the tolerance with which the coherent structure would need to be fabricated may not be physically realisable, therefore we focus more on the incoherent back reflector. Both types of back reflector are shown to increase the absorption compared to the standard Mo back contact.

We then move to bringing together the physical insight built from the previous chapters in order to simulate ultra-thin film solar cells with integrated plasmonic particles in chapters 9 and 10 using the finite element method. We show that particle integration directly inside the absorbing layer leads to the largest absorption enhancement.

We also present in chapters 11 and 12 a method that brings not just the physical insight but also the analytical techniques from chapters 3 and 7 together, this culminates in a coupled method capable of simulating solar cells with integrated plasmonics very rapidly. This method also provides a fast way to simulate devices which contain both incoherent layers and nanoparticles. Due to the speed of this method we use it to optimise the device with integrated nanoparticles, reaching 93% of the thin-film current with only 20% of the material usage.

Finally a conclusion as well as an extended publication list are given.

Chapter 2

Light Management - A Review of the Literature

Now that we have established the goal of developing a light management strategy for photovoltaics, it will be useful to review the literature on light management. Since the majority of the work on light management has been done on various material classes, we focus on the different concepts as they can, in principle, be applied to any material.

Since different solar cell types have slightly different configurations in terms of layers, we present in fig. 2.1 a schematic of a generic solar cell device in order to explain the goal of light trapping. The solar cell principally consists of a layer of an absorbing semiconductor with electric contacts above and below the absorbing layer. In order to allow a current to flow through the device, a pn-junction is usually present in the absorbing layer or at an interface with one of the contacts. Light can come from either above or below depending on design, however the electric contact which is on the side of the incident light should be transparent.

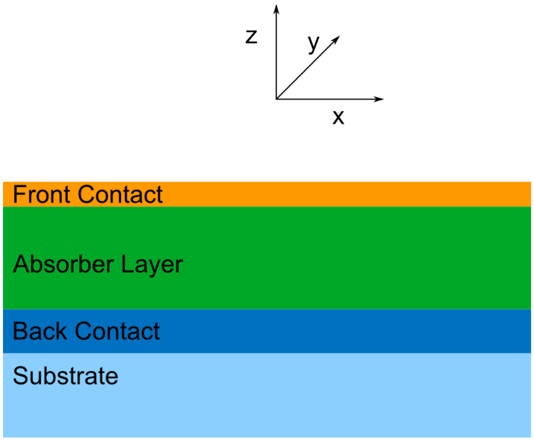

Figure 2.1: A schematic image of the principle layers required for a solar cell.

2.1 Geometrical Optics

From the perspective of a ray model of light (geometrical optics), the light path inside of a photovoltaic absorber can be increased by using the laws of refraction. For normally incident light onto a flat surface, the resulting light ray will still travel normally to the surface. The surface of the solar cell device may then be microstructured causing angled surfaces to be present at the macroscopically flat surface. Depending on the device this will mean structuring the transparent contact or the absorbing layer itself. A ray normally incident to the macroscopic surface will then be incident at an angle to the microscopic surface. This means it will be refracted when passing into the absorber layer, which will increase the angle of propagation inside the absorber layer. Although there will nominally be a higher reflection at this microsurface due to the higher incident angle, the reflections are likely to be reflected into the solar cell for sufficiently steep microstructuring, ensuring a net gain in absorption. This approach to light trapping has been successfully implemented in c-Si solar cells via selective etching of the (100) crystal planes leaving square based pyramids from the (111) planes [3]. Methods which seek to exploit geometrical optics clearly need to have feature sizes large compared to the wavelength in order for the geometrical limit to apply. For the case of thin films and especially ultra-thin films, these kinds of methods will not be applicable since the film thickness is of the same order of magnitude as the wavelength.

2.2 Wave Optics

For the case of thin film solar cells, we require concepts grounded in the wave optics regime. This is not a limitation, indeed as we shall discover, wave optical approaches are capable of providing light path enhancements above and beyond those of ray optical approaches due to interesting light matter interactions. Many of the wave optical concepts can be applied to both metallic and dielectric materials. The underlying physics in each case may be substantially different, nevertheless they will be presented together under a unified device heading (i.e. Grating for both a dielectric and metallic grating).

2.2.1 Random Texturing

One of the earliest works on the optical nature of rough surfaces comes from Rayleigh who described the effect of subwavelength microstructure on the scattering of light [4]. Chinmayanandam tackled the question more quantitatively by introducing the idea of phase shifts introduced by the varying propagation length in the two different materials at an interface caused by the roughness [5]. This idea was further developed by identifying the rough surface as a stochastic process, see for example Davies [6], Beckmann and Spizzichino [7], and Harbeke [8].

The use of surface roughness scattering for light management in solar cells has been suggested since at least 1982 when Yablonovitch and Cody presented a statistical model describing perfectly randomising surface textures. Such textures would lead to a $4n^2$ enhancement in the absorption where n is the refractive index of the absorbing layer. Practical applications include a-Si:H solar cells [9][10][11], where the front Al doped ZnO contact is structured. Although Al:ZnO will have free carriers necessary for a good conductivity, the amount is still much less than for a metal, therefore we can consider this close to being a dielectric material at visible wavelengths. The coupling between a random front surface texture and SPP modes on a metallic back contact has been considered for thin film c-Si [12], however losses in the metal where predicted to outweigh absorption enhancement due to SPP propagation in the silicon.

Texturing metallic surfaces is not beneficial for front side applications since, the metal cannot cover the entire front surface due to absorption in the metal (the case of extraordinary transmission through metal will be treated later) and roughness on the front surface will introduce surface plasmon polaritons which are not likely to be helpful as they would weakly couple to the underlying absorber layer. This is because the surface plasmon polaritons would be excited at the air/metal interface instead of the metal/absorber layer interface where they could potentially be beneficial. Random surface texturing has also been used as an intermediate reflector for the case of tandem a-Si:H / μ-Si solar cells [13], where an intermediate layer of typically SiO_2, Si_3N_4 or ZnO may be used [14] [15] [16].

Random Texturing of metallic back contacts is more promising than front contacts, since they can cover the entire back surface and the structured part is directly in contact with the absorber layer, meaning a high coupling between the metal and the absorber layer. This has been employed as the back contact for a-Si:H solar cells [17], which can show improvement over a flat surface for weakly absorbing cells. However, there is also extensive literature discussing how to remove the parasitic plasmonic absorption from randomly nanostructured metallic back contacts, which suggests that the benefits of coupling to SPP modes is outweighed by the absorption inside the metal [18].

2.2.2 Periodic Texturing or Gratings

Periodic texturing on the order of the wavelength of light allows for diffraction effects, which is the coherent version of the scattering from random surfaces. Due to the coherent nature, this will generally lead to scattering which is stronger for single wavelengths, but which is much more wavelength and angle dependent than for random surfaces. The limits of a grating structure for absorption enhancement have been discussed [19] [20], by placing a dielectric grating on a layer with an extremely low single pass absorption and calculating the absorption enhancement. It was found that 2D dielectric gratings can overcome the Yablonovitch limit over a large range of wavelengths for normal incidence, but for oblique incidence the absorption enhancement falls below the Yablonovitch limit, thus the generalised Yablonovitch limit of $4n^2/\sin(\theta)$ is not overcome when considering all angles.

A periodic structure developed with a form of nanosphere lithography has been shown to perform equally to the highest performing random texture for a-Si solar cells [21]. Additionally numerical strategies for the optimisation of 1D gratings have been presented [22].

A grating-like photonic crystal (a 1D grating comprising of two different material layers) has been theoretically compared to an embedded metallic grating for organic solar cells [23]. The result was that the plasmonic grating achieved a higher absorption enhancement, however since electric performance was not considered, the photonic crystal is likely to achieve a higher photocurrent in reality, due to recombination at the metal surface. MIM structures and plasmonic waveguides have also been shown to beat the Yablonovitch limit for organic materials [24] [25].

Silicon and GaAs nanowires have also been shown to be able to focus light into modes inside the material, causing a possible reduction in material consumption [26] [27].

2.2.3 Pseudoperiodic Texturing

As we have seen from the previous two examples, periodic texturing can provide a very high light path enhancement in certain wavelength regions, corresponding to geometrically resonant conditions. Whereas random texturing leads to an effect with a lower single wavelength response, which is however present at a broad range of wavelengths. This opens up an interesting question, namely, is it possible to combine the effects of periodic and random texturing to obtain a strong and spectrally broad light path enhancement? In recent years, there has been work in this direction [28, 29] that shows that the combination can indeed provide higher absorption enhancement than for either single concept.

2.2.4 Nanoparticles

Generally there is some crossover between the usage of the term nanoparticle and 2D grating, since a regular arrangement of identically shaped particles forms a grating. More generally nanoparticles may also form unordered structures and may have a range of size and shape distributions. The development of the usage of nanoparticles for light management in solar cells has been reversed compared to periodic structures with respect to material selection. Metallic nanoparticles were the first to be discussed [30–32], with dielectric nanoparticles becoming a subsequent research focus [33–35].

Ag plasmonic particles have shown to match the performance of surface textured back contacts in a-Si solar cells [36, 37] as long as the particles are isolated using a dielectric material. Embedding the particles inside the silicon has been investigated theoretically [38], while the absorption enhancement available is considerable, the likely recombination losses due to extra surfaces caused by the particle may outweigh the potential optical gains.

Ag particles have been integrated into organic solar cells [39], the result was that particles integrated on the front surface gave the best performance, while particles integrated into the absorber layer gave a higher optical absorption but a worse performance (due to a worse electric performance).

In conclusion there are many diverse and promising optical concepts for light trapping. We focus on a single concept in this thesis in order to follow that concept from basic principles to full integration. Due to this we are able to take advantage of the knowledge base gained earlier to speed up the process of finding an optimum device later in the thesis. Here we have chosen to focus on plasmonic nanoparticles since they have a large potential in absorption increase but also come with downsides which must be minimised in order to be successfully integrated. Therefore they present a challenging and interesting problem with a potentially large benefit.

Chapter 3

Mie Theory

This chapter will describe the analytical method of Mie theory which can be used to obtain the interaction of light with spherical nanoparticles.

3.1 Mie Theory

The most influential work on the interaction between light and metallic nanoparticles comes from Gustav Mie who in 1908 formulated a complete solution to Maxwell's equations for a plane wave incident to a spherical geometry. This solution is typically referred to as 'Mie Theory' [40]. The path to a solution comes from expressing the incident, scattered and internal fields in terms of a summation of orthonormal basis functions called the spherical vector harmonics. The weighting of each function is determined by the boundary conditions at the surface of the sphere which depend on the sphere size and the interior and exterior dielectric functions. The boundary conditions at the sphere surface are the continuity of the tangential E field and the normal D field. These weightings are called the Mie coefficients.

We will now present some of the most important results regarding Mie theory, these are taken from the book of Bohren and Huffmann [41]. As mentioned previously, the geometry considered has a spherical symmetry, meaning that the scattered and internal fields are well described by the spherical vector harmonics. The difficult part is to also describe the incident field using the same basis functions in order to know the incident amplitude for each mode of oscillation (i.e. each order of spherical vector harmonic). Even though an incident plane wave does not possess spherical symmetry, it is still possible to describe the incident fields in terms of the spherical vector harmonics.

Since we are free to orientate our axis at will, due to the spherical symmetry, let the incident plane wave be travelling parallel to the z axis with the E field pointing along the x direction

$$\mathbf{E}_{inc} = E_0 e^{ik_z z}\hat{\mathbf{e}}_x. \tag{3.1}$$

Where E_0 is the incident field amplitude, i is the imaginary unit, k_z is the z component of the wave vector, z is the distance along the z axis and $\hat{\mathbf{e}}_x$ is the unit vector of the x axis. We wish to re-express $\mathbf{E}_{inc}$ in terms of the spherical vector harmonics which we shall now briefly describe. The spherical vector harmonics are vector functions which solve the vector wave equation generated from scalar functions which solve the scalar wave equation. Therefore we first review the solution to the scalar wave equation. The scalar wave equation, without specifying a coordinate system, is

$$\nabla^2\psi + k^2\psi = 0. \tag{3.2}$$

The solution to this equation in spherical coordinates can be obtained by separation of variables and yields the following result

$$\psi_{emn} = \cos(m\phi)P_n^m(\cos\theta)z_n(kr), \tag{3.3}$$

$$\psi_{omn} = \sin(m\phi)P_n^m(\cos\theta)z_n(kr). \tag{3.4}$$

We have an even (subscript e) and an odd (subscript o) solution depending on the symmetry of the function for the azimuthal (ϕ) angle. The even form contains the even function cos while the odd form contains the odd function sin. Furthermore these azimuthal functions are dependent on the integer m. The associated Legendre polynomials $P_n^m(\cos\theta)$ determine the polar angle θ dependence and depend on both the integers m and n. The last part which gives the radial dependence of the solution is actually a placeholder for other functions. These functions are the suite of spherical Bessel functions, $j_n(\rho)$, $y_n(\rho)$, $h_n^1(\rho)$ and $h_n^2(\rho)$, which are the spherical Bessel function of the first, second, third and fourth kind, respectively. The first and second kind form a pair of linearly independent solutions to the Bessel differential equations, while the third and fourth kind offer a different possibility for linearly independent solutions. Two linearly independent solutions are required not only for these functions to form a complete set, but also for physical reasons. The different spherical Bessel functions have different limits at the origin ($j_n(\rho)$ is finite while $y_n(\rho)$ is divergent) meaning that only $j_n(\rho)$

can describe fields at the origin. In cases where we do not need to consider the origin (e.g. for the scattered field) we cannot a priori rule out either one of $j_n(\rho)$ or $y_n(\rho)$. However it turns out that we can simplify things by using the third and fourth spherical Bessel functions. In the asymptotic limit, these two functions describe an outgoing and incoming spherical wave respectively. Since the scattered wave is purely outgoing, we only need to use $h_n^1(\rho)$ in the expansion. Therefore only the functions $j_n(\rho)$ and $h_n^1(\rho)$ are needed for the Mie theory expansions containing the origin or infinite exterior.

Finally there is one more distinction to be made and that is how the spherical *vector* harmonics are generated from the spherical harmonics. There are two orthogonal choices for the generation of the vector functions

$$\mathbf{M} = \nabla \times (c\psi), \tag{3.5}$$

$$\mathbf{N} = \frac{\nabla \times \mathbf{M}}{k}, \tag{3.6}$$

where c stands for any constant, k is the wave number and ψ is the solution to the scalar wave equation. This turns out to be more than a mathematical necessity, the different choices represent physically different modes. The M type fields describe modes with no radial magnetic field components, these are referred to as electric type or transverse magnetic modes. The transverse magnetic part is due to the magnetic field only having transverse components, the electric name refers to these modes describing the effects of electric multipoles (e.g. dipole, quadrupole). The N type fields describe magnetic modes which have no radial electric components, and describe magnetic multipoles.

Considering the two different vector functions $\mathbf{M}$ and $\mathbf{N}$ and the fact that they both have an odd and even form and that two different spherical bessel functions can be used as generating functions we have in total 2x2x2 = 8 different functions needed to specify the vector fields in Mie theory. While this may seem like a lot of functions, it will end up with the expressions for the electric and magnetic fields being pleasingly simple.

Since the scattered and internal fields are dependent on the incident field, the first thing to describe using spherical vector harmonics is the incident field

$$\mathbf{E}_{inc} = E_0 \sum_{n=1}^{\infty} i^n \frac{2n+1}{n(n+1)} (\mathbf{M}^1_{o1n} - i\mathbf{N}^1_{e1n}), \tag{3.7}$$

$$\mathbf{H}_{inc} = \frac{-k}{\omega\mu} E_0 \sum_{n=1}^{\infty} i^n \frac{2n+1}{n(n+1)} (\mathbf{M}^1_{e1n} + i\mathbf{N}^1_{o1n}), \tag{3.8}$$

where ω and μ are the frequency of the wave and the permeability of the surrounding medium, respectively. Note that a sum over all m values is not required since the expression vanishes for all $m \neq 1$. This infinite series does not have to be evaluated directly, since the expression for the incident field is only used inside of expressions for the scattered and interior fields.

The expression for the scattered field in terms of the incident field is given by

$$\mathbf{E}_s = \sum_{n=1}^{\infty} E_{inc}(ia_n\mathbf{N}^3_{e1n} - b_n\mathbf{M}^3_{o1n}), \tag{3.9}$$

$$\mathbf{H}_s = \frac{k}{\omega\mu}\sum_{n=1}^{\infty} E_{inc}(ib_n\mathbf{N}^3_{o1n} - a_n\mathbf{M}^3_{e1n}). \tag{3.10}$$

E_{inc} and H_{inc} are the n^{th} coefficients of the expansion for the incident field. The a_n and b_n are called the Mie coefficients and their values are determined by boundary conditions at the interface of the sphere. A similar expression for the interior fields is given by

$$\mathbf{E}_i = \sum_{n=1}^{\infty} E_{inc}(c_n\mathbf{M}^1_{o1n} - id_n\mathbf{N}^1_{e1n}), \tag{3.11}$$

$$\mathbf{H}_i = \frac{-k_i}{\omega\mu_i}\sum_{n=1}^{\infty} E_{inc}(d_n\mathbf{M}^1_{e1n} + ic_n\mathbf{N}^1_{o1n}), \tag{3.12}$$

where k_i and μ_i are the wave number and permeability inside the sphere, respectively.

The only remaining step is to define the a,b,c and d coefficients used in these expansions. In order to simplify these expressions as much as possible, we first assume that the permeability inside and outside the sphere is unity, which is valid for non-magnetic materials. Secondly we introduce the Riccati-Bessel functions

$$\psi_n(x) = xj^1_n(x), \tag{3.13}$$

$$\xi_n(x) = xh^1_n(x). \tag{3.14}$$

Given these simplifications, the Mie coefficients can be written as

$$a_n = \frac{m\psi_n(mx)\psi_n'(x) - \psi_n(x)\psi_n'(mx)}{m\psi_n(mx)\xi_n'(x) - \xi_n(x)\psi_n'(mx)}, \tag{3.15}$$

$$b_n = \frac{\psi_n(mx)\psi_n'(x) - m\psi_n(x)\psi_n'(mx)}{\psi_n(mx)\xi_n'(x) - m\xi_n(x)\psi_n'(mx)}, \tag{3.16}$$

$$c_n = \frac{m\psi_n(x)\xi_n'(x) - m\xi_n(x)\psi_n'(x)}{\psi_n(x)\xi_n'(x) - m\xi_n(x)\psi_n'(mx)}, \tag{3.17}$$

$$d_n = \frac{m\psi_n(x)\xi_n'(x) - m\xi_n(x)\psi_n'(x)}{m\psi_n(mx)\xi_n'(x) - \xi_n(x)\psi_n'(mx)}. \tag{3.18}$$

The two arguments involved in these coefficients are the size parameter x and the relative refractive index m which are defined as

$$x = kr, \tag{3.19}$$

$$m = \frac{n_p}{n}, \tag{3.20}$$

where r is the sphere radius and n_p and n are the refractive index of inside and outside the sphere, respectively. Returning to the previous definition of n as the summation subscript for the expansion, we see that as the value of n increases, the value of all of these coefficients will eventually become negligible, meaning that the infinite sums for the fields can be evaluated since above a cutoff value for n, all the coefficients are negligible.

We now have the complete description of the fields inside and outside of the sphere. For a comparison to far field measurements, the cross sections in the far field are needed. These follow naturally from the definitions of the fields given; the scattering and extinction cross section for a sphere are

$$Q_{sca} = \frac{2}{x^2}\sum_{n=1}^{\infty}(2n+1)(|a_n|^2 + |b_n|^2), \tag{3.21}$$

$$Q_{ext} = \frac{2}{x^2}\sum_{n=1}^{\infty}(2n+1)\Re(a_n + b_n). \tag{3.22}$$

These are both a sum of contributions from the electric type (a_n) and the magnetic type (b_n) modes for different multipole orders (n). The absorption cross section can be obtained using the optical theorem as $Q_{abs} = Q_{ext} - Q_{sca}$. There is no simple expression for the absorption cross section, for a single particle this is not a problem, however for a particle with multiple layers, this will become problematic. This will be discussed later in the chapter. We also take a moment to mention that in contrast to the standard definition of optical cross section C which has units of area, we instead use the normalised cross section Q which is unitless. The relationship between the two is $Q = C/(\pi r^2)$

where r is the particle radius. This means that we normalise the cross section to the geometrical area perpendicular to the direction of incidence. This value is sometimes called the efficiency, however this terminology is confusing because usually an efficiency cannot become larger than one, which is not true for Q. Additionally we reserved the term efficiency to refer to the fraction of light converted into a particular channel, either scattering or absorption, e.g. the scattering efficiency is given by Q_{sca}/Q_{ext}.

Finally since we are also interested in the near field intensity we also would like to calculate the near field cross section, which is defined as [42]

$$Q_{nf} = \frac{2}{x^2} \int_0^{2\pi} \int_0^{pi} \mathbf{E_s} \cdot \mathbf{E_s^*} \sin\theta d\theta d\phi \bigg|_{R=a}, \tag{3.23}$$

which is simply the scattered field intensity evaluated at the sphere surface. This can be calculated by first computing $\mathbf{E_s}$ at points on the sphere surface and numerically integrating the result. A quicker method has been presented which uses the fact that we are in the near field to simplify the integral to the following expression in terms of the Mie coefficients

$$\begin{aligned} Q_{nf} = 2\sum_{n=1}^{\infty} &|a_n|^2 \left[(n+1)|h_{n-1}^2(x)|^2 + n|h_{n+1}^2(x)|^2\right] \\ &+ |b_n|^2 \left[(2n+1)|h_n^2(x)|^2\right], \end{aligned} \tag{3.24}$$

where $h_n^2(x)$ is the second spherical Hankel function (spherical Bessel function of the fourth kind).

3.2 Core Shell Particles

For practical applications to optoelectronic devices, nanoparticles embedded directly into a device material may be deleterious. This is due to two principle reasons:

- The nanoparticle may be chemically unstable, meaning that it will diffuse or otherwise cause some chemical reaction during the device processing which harms device performance.
- The nanoparticle may act as an electric loss center. Even for materials with low optical losses, the electrical loss due to recombination at the surface of the metal may be unacceptable.

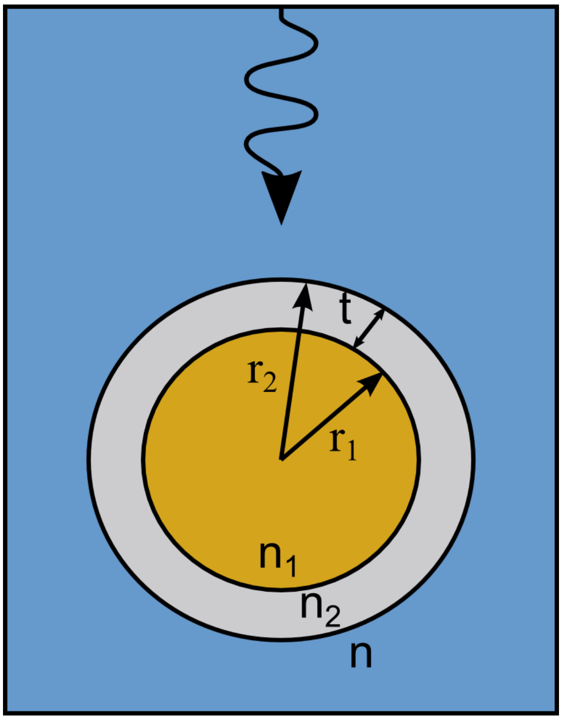

Figure 3.1: The simulation geometry for core shell particles.

To overcome both these challenges we can use instead a core-shell type structure. The core of the particle is metallic which provides the desired optical properties, while a thin shell of a different material, typically an isolator, is used to both provide chemical stability and electrical isolation. This idea for the implementation of core-shell particles into solar cell devices has already been studied in the literature. However until now the shell material was chosen to fulfill the previous aims but was not optimised for optical performance. We have instead taken the approach of looking for more exotic materials which, while being more difficult to prepare, may offer significant optical gains when device implementation is taken into account.

The first step to studying the properties of core-shell particles is to extend the Mie theory in order to account for shell layers. Since the problem remains in this case spherically symmetrical, most of the groundwork used in the formulation of the standard Mie theory still applies. We need only determine coefficients for the expansion of the scattered and two internal fields in terms of spherical vector harmonics.

Consider a plane wave incident onto a core-shell particle as shown in fig. 3.1. The particle has a core radius r_1 and a shell radius r_2 resulting in two size parameters $x_1 = kr_1$ and $x_2 = kr_2$ where k is the wave vector in the surrounding material. The refractive indices of the two materials will be n_1 and n_2 and the relative refractive indices are $m_1 = n_1/n$ and $m_2 = n_2/n$ where n is the refractive index of the surrounding material. Like with the single sphere, we may take the scalar generating solution inside the core to be expanded only in $j_n(r)$ terms (due to $y_n(r)$ being divergent at the origin) and the scattered field solution to be expanded only in $h_n^1(r)$ since this describes an outgoing spherical wave. For the fields inside the shell (E_2 and H_2) we cannot simplify in this way and we must keep the whole field expansion

$$\mathbf{E}_2 = \sum_{n=1}^{\infty} E_{inc}(f_n \mathbf{M}^1_{o1n} - i g_n \mathbf{N}^1_{e1n} + v_n \mathbf{M}^2_{o1n} - i w_n \mathbf{N}^2_{e1n}), \tag{3.25}$$

$$\mathbf{H}_2 = \frac{-k_2}{\omega \mu_2} \sum_{n=1}^{\infty} E_{inc}(g_n \mathbf{M}^1_{e1n} - i f_n \mathbf{N}^1_{o1n} + w_n \mathbf{M}^2_{e1n} - i v_n \mathbf{N}^2_{o1n}). \tag{3.26}$$

By applying the usual boundary conditions at the interfaces between core and shell, and shell and exterior, we obtain *eight* equations for the variables a_n, b_n, c_n, d_n, f_n, g_n, v_n and w_n. By once again assuming that all materials are non magnetic ($\mu_1 = \mu_2 = \mu = 0$) and introducing another Riccati-Bessel function

$$\chi_n(\rho) = -\rho y_n(\rho), \tag{3.27}$$

the system of equations can be solved for the various coefficients allowing for all the interior and scattered fields to be described. However, our definitions for the different cross sections (scattering, absorption, extinction and near-field) only required the a and b coefficients, that is, the coefficients associated with the scattered wave. Therefore for calculations of the scattering cross sections, we only need these two coefficients. The resulting value for the absorption cross section will be valid for the entire core-shell particle. It will not be possible to distinguish between absorption in the core from absorption in the shell using only the a and b coefficients. In order to separate out the two, we have to numerically integrate the fields inside the volume of the core and shell. This process is much more computationally demanding than evaluating just a and b. Therefore we consider only the case of nonabsorbing shell materials, meaning that all of the absorption can be attributed to the plasmonic core.

Chapter 4

Plasmonics with Symmetry

This chapter will be devoted to discussing analytical solutions to Maxwell's equations that are relevant to the field of plasmonics. Most of the chapter is focused on the optical properties of nanoparticles, in particular the localised surface plasmon resonance which is the most relevant to absorption enhancement in solar cells.

4.1 Maxwell's Equations

Plasmonics is essentially the study of solutions to Maxwell's equations with materials bearing free charge carriers, i.e. metals. Therefore we begin by stating the macroscopic Maxwell equations [43]

$$\begin{aligned} \nabla.\mathbf{D} =& \rho_f, && (4.1) \\ \nabla.\mathbf{B} =& 0, && (4.2) \\ \nabla \times \mathbf{E} =& -\frac{\partial \mathbf{B}}{\partial t}, && (4.3) \\ \nabla \times \mathbf{H} =& \mathbf{J_f} + \frac{\partial \mathbf{D}}{\partial t}. && (4.4) \end{aligned}$$

The macroscopic form differs from the microscopic form via the inclusion of the **D** and **H** fields. These fields incorporate not only the **E** and **B** fields, respectively, but also the polarisation **P** and magnetisation **M** which depend on the material in which the field is being evaluated. In real terms the macroscopic Maxwell equations describe the effect of electric and magnetic fields on matter made up of atoms, whereas the microscopic equations describe the effect of electric and magnetic fields on the constituents (electrons, protons) of atoms. This is a viable approach because the net effect of all the individual charges that make up the atoms in matter can be conveniently described by a single dielectric function. This function describes all the quantum effects which would have to be included explicitly in an approach using the microscopic equations. Thus the macroscopic equations, while exact from a mathematical view, are an approximation of reality, albeit a very good one. We should keep in mind that for length scales (of geometrical objects or of the wavelength of light) on the order of a few atoms, materials may no longer be well described by a dielectric function.

4.2 Dielectric Functions of Materials

Dielectric functions will allow us to classify materials and are essential to solving the macroscopic Maxwell equations. Here we state the general properties of the dielectric function for a dielectric material and state some analytical models for both dielectrics and metals. For further information on the topic see [44].

4.2.1 General Dielectric Function

Figure 4.1 shows the dielectric function of a generic dielectric material. The dielectric function otherwise known as the relative permittivity ϵ_r has a real and an imaginary part, $\epsilon_r = \epsilon_r^{'} + i\epsilon_r^{''}$. The real part describes the polarisation charge density in the material, while the imaginary part describes optical loss in the material (conversion of radiative energy to thermal energy in the material). Since we are interested in the optical properties of materials, we shall mainly focus on the dielectric function on the far right of fig. 4.1 which includes the near infrared, visible and ultra-violet spectrum. However a short description of the other processes will give us a more detailed understanding of dielectric functions. The general dielectric function is split up into contributions from different physical processes which each operate on their own timescale. Starting at the lowest end of the frequency spectrum on the left hand side, we see that $\epsilon_r^{'}$ has its maximum value, this is because at low frequencies all the possible contributions to the permittivity are present.

The atomic and electronic contributions come from dipoles induced by incident fields. The atomic or lattice contributions come from distortion in the positions of atoms in the crystal lattice which causes a dipole to form opposing the incident field. This dipole acts as a restoring force leading to simple harmonic motion for an oscillating incident field. The electronic contributions are similar but describe the distortion of the electronic cloud of the atoms themselves, which again induces a dipolar restoring force on the electron cloud. These kind of simple harmonic motions can be well described using the Lorentz oscillator model.

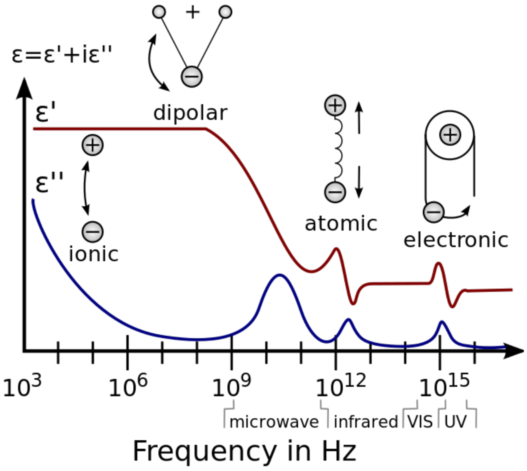

FIGURE 4.1: The general features of the complex dielectric function of a dielectric material. Contributions from ionic, dipolar, atomic and electronic resonances are shown.

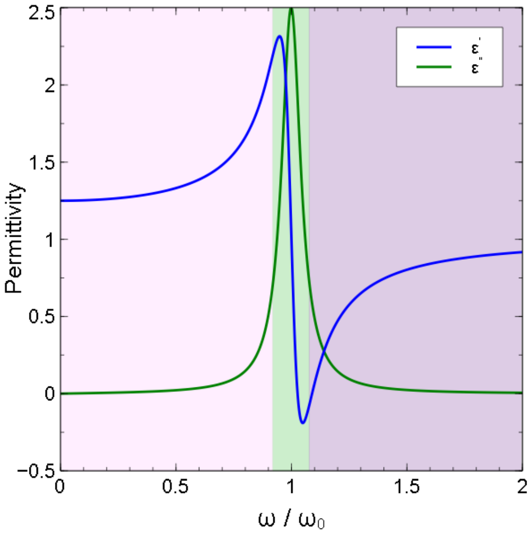

FIGURE 4.2: The complex permitivitty $\epsilon = \epsilon^{'} + i\epsilon^{''}$ of a Lorentz oscillator as a function of the Lorentz natural frequency ω_0. Three frequency regions are highlighted: below resonance (pink), at resonance (light green) and above resonance (purple).

4.2.2 Lorentz Oscillator

If we assume that all other contributions to the dielectric function are negligible at optical frequencies, then we need only describe the electronic contribution. The simplest model for the permittivity of dielectric materials is the Lorentz oscillator. This model assumes that each atom can be described as a sum of harmonic oscillators with the electrons behaving like masses on a spring where the restorative force is given by the Coulomb force. Although this is a simple model, it gives a good conceptual basis for understanding dielectric materials. The equation of motion for the position of the electron $x(t)$ can be

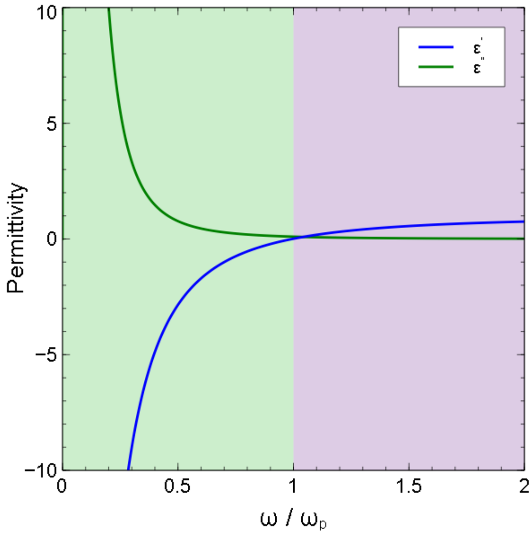

FIGURE 4.3: The complex permitivitty $\epsilon = \epsilon^{'} + i\epsilon^{''}$ of a Drude metal as a function of the plasma frequency ω_p. Two frequency regions are highlighted: below the plasma frequency (light green) and above the plasma frequency (purple).

written as

$$m\frac{d^2x}{d^2t} = -m\omega_0 x + qE_x - m\gamma\frac{dx}{dt}, \tag{4.5}$$

where m is the electron mass, ω_0 is the natural frequency of the electron oscillations, q is the electronic charge, E_x is the applied electric field and γ is the damping. On the left hand side of the equation, we have mass times the acceleration of the electron, therefore on the right hand side we assemble the forces acting on the electron. Firstly we have the restorative force of the nucleus which is described by the natural oscillation frequency. Secondly is the applied electric field. Thirdly we have the friction like force induced by losses that is proportional to the velocity of the electron. If we then assume that both the applied field and the motion of electron are time harmonic (i.e. the time dependence is given by $e^{-i\omega t}$), then the solution for the electronic position is

$$x(t) = \frac{q}{m}\frac{1}{(\omega_0^2 - \omega^2) - i\omega\gamma}E_x. \tag{4.6}$$

There are three distinct modes of motion depending on the frequency of the applied field ω. At low frequencies there is a medium response from the electron to the applied field and the motion of the electron is in phase with the applied field. When the frequency reaches the value which minimises the denominator of equation 4.6, called the resonance frequency, which for small damping γ is given by

$$\omega_r = \omega_0, \tag{4.7}$$

the oscillations will become very large in magnitude and a phase shift will occur with the oscillations moving from in phase to antiphase with respect to the applied electric field. At the resonance frequency the phase difference between the applied field and the motion of the electron will be exactly $\pi/2$. At frequencies above the resonant frequency, the amplitude of oscillations tends towards zero and the oscillations and driving force are in anti-phase. This is the general description for a resonant process involving a driven harmonic oscillator, and will come up again in the discussion of plasmonic resonances.

So far we have only described the position of the electron with time, to obtain the dielectric function we must convert this to a resulting permittivity. To do this we use the definition of the permittivity and polarisation

$$\mathbf{D} = \epsilon_r \epsilon_0 \mathbf{E}, \tag{4.8}$$

$$\mathbf{D} = \epsilon_0 \mathbf{E} + \mathbf{P}, \tag{4.9}$$

$$\mathbf{P} = Nq\mathbf{x}. \tag{4.10}$$

Where N is the density of oscillators per unit volume. Using these relationships leads directly to the Lorentz equation for permittivity

$$\epsilon_r = 1 + \frac{\omega_p^2}{(\omega_0^2 - \omega^2) - i\gamma\omega}, \tag{4.11}$$

$$\omega_p^2 = \frac{Nq^2}{\epsilon_0 m}. \tag{4.12}$$

ω_p is the so called plasma frequency, the physical meaning of the plasma frequency will be discussed in the following section. Figure 4.2 shows the frequency response of the Lorentz dielectric function. The three regions discussed have been highlighted, the pink region shows the low frequency in-phase response. This region has little loss ($\epsilon^{''}$) and far away from the resonance frequency the real part of the permittivity is close to constant. This means that later we can use constant values of permittivity with zero absorption as a model for dielectric materials far below their resonant frequencies. The green region shows the resonance position where there is a shift from normal dispersion ($\epsilon^{'}$ increases with frequency) to anomalous dispersion where $\epsilon^{'}$ decreases with frequency. This region also has significant absorption which can be seen from the high value of $\epsilon^{''}$. To understand why there is a strong absorption at this frequency, the general idea of a resonant process must be understood. In a driven harmonic oscillator, at the resonant frequency, the driving force gives energy to the resonator during every cycle. At the resonant frequency this energy builds up during each cycle of the harmonic driving force, if there were no loss in the system ($\gamma = 0$) then the energy would keep building up infinitely. However since we do have some losses, the energy in the resonator builds up until the energy added by the driving force is exactly equaled by the dissipation from the losses. This is why absorption is significant at the resonant frequency, since only at this frequency does energy build up in the resonator. At frequencies above the resonant frequency the dielectric function tends towards the dielectric function for vacuum ($\epsilon^{'} = 1, \epsilon^{''} = 0$) which means there is no response to the driving force.

4.2.3 Drude Model

We now move to the standard model for the permittivity of metals, the Drude model. This model shares a lot of mathematical similarities with the Lorentz model, but the physical picture is quite different. The Drude model assumes that there is no restorative force from the ions, i.e. the electrons are really free electrons. If we return to the equation of motion used in the Lorentz model and remove the restoring force, we are left with

$$m\frac{d^2x}{d^2t} = qE_x - m\gamma\frac{dx}{dt}. \tag{4.13}$$

By following the same steps as for the Lorentz oscillator, we will again arrive at the permittivity given by

$$\epsilon_r = 1 - \frac{\omega_p^2}{\omega^2 + i\gamma\omega}, \tag{4.14}$$

$$\omega_p^2 = \frac{Nq^2}{\epsilon_0 m}. \tag{4.15}$$

This can be achieved by allowing $\omega_0 \rightarrow 0$ in the Lorentz oscillator model, which will also become apparent when plotting the Drude dielectric function. In fig 4.3 the Drude model permittivity is sketched. This time there is no below resonance region, since the resonant region is shifted to zero frequency. This means that for free electrons, the maximum energy is transferred from the driving field to the electrons when the driving field is static. This makes intuitive sense, since there is no restorative force, simply accelerating the electrons in one direction will give them more energy than oscillating back and forth. The loss in this case comes from scattering processes and limits how much energy the electrons can be given (how much they can be accelerated). The reason this deserves a classification separate from the Lorentz model (other than historical reasons) is that the repercussions of a zero resonance frequency drastically change the optical properties. For the example given in fig. 4.3 the absorption ($\epsilon^{''}$) only starts to significantly increase below $0.5\omega_p$. If we assume that ω_p lies in the optical region then the Drude model predicts low absorption for metals, which is true, the main cause for absorption in metals in the optical regime comes from sources not taken into account in the Drude model. The most impactful of these sources is the inter-band transition, in which an electron from a lower energy band than the conduction band is optically promoted to the conduction band. This will then decay non-radiatively causing a net absorption in the metal.

The real part of the permittivity is below zero for frequencies below ω_p and between zero and one for frequencies above ω_p. This gives a stark change in the optical behaviour of the metal, for $\omega < \omega_p$ the metal will be highly reflective. This is because any incident electromagnetic wave will cause the free electrons to oscillate in such a way that they produce a secondary wave that destructively interferes with the incident wave. The result is no transmitted wave and only a reflected wave. For $\omega > \omega_p$ the oscillations become faster than the electrons can respond, this is because ω_p is the natural frequency of motion of the free electrons. For these frequencies, we move to the bulk plasmon description.

4.3 Bulk and Surface Plasmon

Having discussed the Drude model, we have already covered the concept of the bulk plasmon since it is an integral part of the model. Figure 4.4 shows the dispersion relation for three kinds of plasmon: the bulk plasmon, the surface plasmon polariton and the localised surface plasmon resonance. Also shown is the light line (dashed line) which is crucial to understanding the relationship between a bulk and surface plasmon. The bulk plasmon frequency is shown as a horizontal line labeled ω_{BP}, this line represents the longitudinal oscillations of charge density which are usually referred to as a bulk plasmon. Likewise the surface plasmon frequency is also shown as a horizontal line. This corresponds to longitudinal charge density oscillations that occur at a metal surface propagating parallel to the surface. They are lower in energy than the bulk plasmons since the region above the surface which does not contain plasma does not contribute to the restoring force present in the Drude model. The weaker restoring force for electrons oscillating parallel to the surface means that less energy is required to excite the oscillations.

The figure also shows the dispersion of two modes in solid black lines. These modes are the bulk plasmon polariton (upper) and surface plasmon polariton (lower), the word polariton means that the longitudinal mode has been coupled to the light. The dispersion of the bulk plasmon and surface plasmon polariton are both formed due to the no crossing principle. Light is a transverse wave while charge oscillations are a longitudinal wave. However since charged particles may also be affected by electromagnetic fields, the two types of oscillation may be coupled together. Generally in physics where there exists a system of two weakly coupled modes (e.g. two masses on springs which are

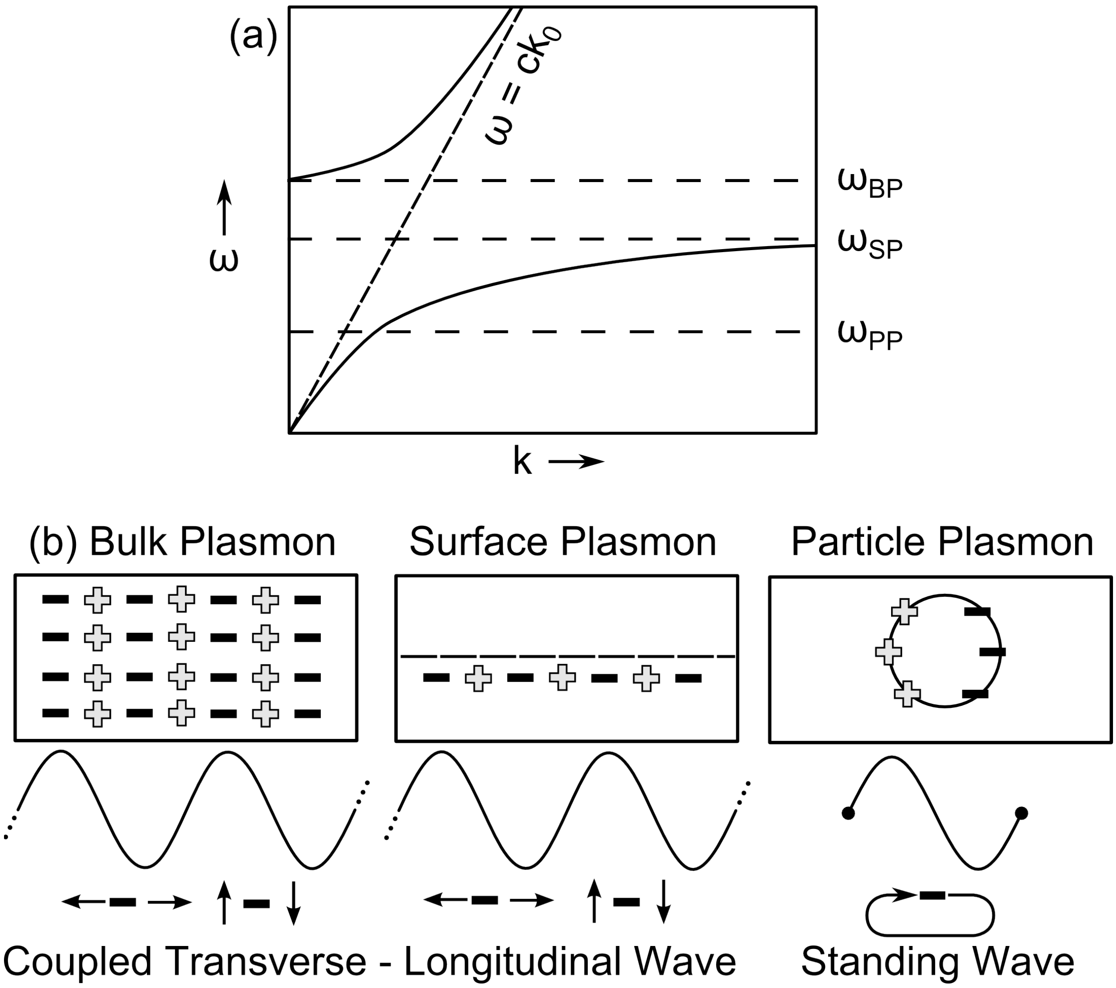

FIGURE 4.4: (a) The dispersion of the bulk plasmon and surface plasmon polariton are shown in solid black lines, the lightline is shown as a diagonal dashed line. The three horizontal lines refer to the frequencies of the three kinds of plasma resonance, the bulk plasmon (ω_{BP}), the surface plasmon polariton (ω_{SP}) and the localised surface plasmon resonance also known as the particle plasmon (ω_{PP}). (b) the physical charge distribution for each plasmon type, the bulk and surface plasmon are coupled transverse and longitudinal travelling waves, the particle plasmon is a standing wave.

connected by a third spring) the dispersion of the two modes will seemingly repel each other leading to an avoided crossing with a gap forming between the modes. In this case, the light mode and the electron density mode avoid crossing each other, leading to a higher energy mode called the bulk plasmon since it propagates inside the metal, and the surface plasmon polariton since it propagates at the surface between the metal and the surrounding medium. The slight difference being that the limiting longitudinal frequency for the surface plasmon polariton is reduced to ω_{SP} compared to ω_{BP} for the bulk plasmon. For both types of wave, when the dispersion moves closer to one of the two horizontal lines, the oscillations become more longitudinal in nature. Conversely when the dispersion curves move closer to the light line, the transverse components of the E field will dominate over the longitudinal ones. Since bulk plasmons involve propagation purely inside the metal, they are of little use to absorption enhancement in solar cells, therefore we move onto the surface plasmon polariton which is more suitable for this application.

Consider a planar interface between a metal and dielectric in the x-y plane at $z = 0$. We wish to find a solution to Maxwell's equations for a wave travelling along the surface that is also bound to the surface. That means that it decays exponentially when moving away from the surface. The symmetry that is exploited in order to obtain an analytical solution is in the x-y plane. The dielectric and metal are homogeneous in the upper and lower half space, respectively, meaning the only discontinuity in permittivity is at $z = 0$. By using the continuity of the transverse E field components and the normal D field component it is possible to show that a mode can exist if there is a sign change in the real part of the permittivity between the two materials. From the analysis of the Drude and Lorentz models, we can directly observe that for large frequency regions, a metal will have a negative real part to the permittivity, while a dielectric will have a positive part so long as it is below the Lorentz resonant frequency. If that is the case then the dispersion for the in plane component of the k vector for the wave (i.e. the propagation constant) will be given by [45]

$$k = \frac{\omega}{c}\left(\frac{\epsilon_1\epsilon_2}{\epsilon_1 + \epsilon_2}\right). \tag{4.16}$$

Where ω is the frequency of the wave, c is the speed of light in free space and ϵ_1 and ϵ_2 are the permittivities of the metal and dielectric, respectively. The physical interpretation of this bound mode is a coupling between the longitudinal charge density oscillations and the transverse electromagnetic wave. This dispersion is plotted in fig. 4.4, the dispersion line changes from being very close to the light line for low frequency, until it is asymptotically horizontal as we increase towards the surface plasmon frequency. How close the dispersion is to either one of these limits determines the relative strength of the components; the transverse ones dominate near the light line, while the longitudinal ones dominate close to ω_{SP}. In fact ω_{SP} can be calculated by rearranging 4.16 and letting the wave vector $k \to \infty$. Assuming a lossless Drude model for the dispersion of the metal and vacuum for the surrounding medium we obtain

$$\omega_{sp} = \frac{\omega_p}{\sqrt{2}}. \tag{4.17}$$

The reason that such modes are not excited when shining light onto a metallic surface is that the momentum of a SPP mode is higher than that of a photon in the dielectric medium where the SPP mode should form. This can be understood by looking at the dispersion curve of a photon and SPP mode. Figure 4.4(a) shows the dispersion of a photon (solid black line) and a SPP mode (dot dashed black line) as well as the SPP resonance frequency (ω_{sp}). The SPP mode lies to the right of the light line for all frequency values, this means that it has a higher wavevector and therefore momentum.

One solution to exciting this kind of plasmonic mode is to use evanescent coupling, similar to the concept of quantum tunneling for electrons. In a simple prism, for certain incident angles, light will be totally internally reflected. At the total internal reflection interface an evanescent wave will occur, meaning that the totally internally reflected wave decays exponentially outside the prism. If a metallic surface is brought close (typically less than 100 nm) to the prism, then the evanescent wave can excite a SPP mode propagating at the air/metal interface. This is because the prism has a higher permittivity than the air, meaning that light inside the prism has a higher k vector and therefore more momentum. If the k vector parallel to the interface matches k_{spp} given by equation 4.16 calculated using the metal and air permittivity, then a SPP mode will be excited. This can be imaged by measuring the reflection from the prism, which will drop when coupling to the SPP occurs. This setup for measuring a SPP mode is called the Otto configuration.

Other methods exist for coupling to a SPP mode that are more practical for photovoltaic applications. A grating structure formed in the metal can provide the extra momentum to incident light in order to couple to SPP modes. The diffraction orders tend to be narrowband and angle dependent, therefore could provide difficulties in covering the whole spectrum and for devices without tracking. Devices that are more tolerant to a range of incident angles can be formed using localised surface plasmon resonances.

4.4 Localised Surface Plasmon Resonance

The third and final type of plasmon is the localised surface plasmon resonance (LSPR), also called particle plasmon. This kind of plasmon is excited in nanoparticles and for the case of a spherical nanoparticle, Mie theory can be used to compute the solution which was shown in chapter 3. Note that for the LSPR we do not obtain the dispersion for a type of travelling wave as in the case of bulk and surface plasmon. This is because a nanoparticle has a finite extent in all three directions. Therefore the coupled charge density oscillations cannot travel anywhere and they form a kind of standing wave at the particle boundary. Since the resonance frequency is independent of the incident wavelength, there is no dispersion curve for the LSPR, as long as the light line passes through the frequency of the LSPR, it will be able to excite an LSPR.

This has the implication that there is no momentum matching condition necessary to excite a LSPR, as long as the frequency of light matches the LSPR frequency (ω_{PP} in fig. 4.4) the resonance will be excited. To understand why momentum does not need to be conserved in more detail we rely on Noether's theorem. The theorem states that *every differentiable symmetry of the action of a physical system has a corresponding conservation law*, which means that symmetries in physical systems lead to conservation laws. In the case of SPP modes, we assumed that the interface is infinitely extended in the $x - y$ plane, meaning that any translation in the $x - y$ plane would leave us with exactly the same system. That is why the k_x and k_y wave vector components are conserved in exciting a SPP mode (Note k_z is not conserved because there is no continuous symmetry in the z direction). Likewise for the particle, the system is not symmetric with respect to translations in any direction due to the particle's finite extent, thus meaning that there is no momentum conservation requirement.

Typically when measuring the optical behaviour of nanoparticles, the extinction cross section is used as the figure of merit. The extinction is the total of both scattering and absorption. To measure extinction means to pass light through a solution containing nanoparticles and measure the intensity of the directly transmitted beam, meaning that light scattered into different angles is not measured, the reduction in light intensity in the transmitted beam is equal to the extinction. The measured extinction should be equal to the distance the light has to travel through the sample, multiplied by the concentration of particles in the sample and by the extinction cross section C_{ext}. This is valid for low concentrations where the effect of multiple particle interactions may be neglected.

The frequency at which the resonance occurs can be obtained by looking at the extinction cross section. Although an expression for the exact extinction cross section was introduced in chapter 3, we refer here to a simplification in order to make the origin of the LSPR resonance frequency clearer. The extinction cross section for a spherical particle in the dipole approximation is given by

$$C_{ext} = 9\frac{\omega}{c}\epsilon_m^{3/2}V\frac{\epsilon^{''}}{(\epsilon^{'} + 2\epsilon_m)^2 + (\epsilon^{''})^2}. \tag{4.18}$$

Where V is the particle volume, $\epsilon^{'}$ and $\epsilon^{''}$ are the real and imaginary parts of the metal nanoparticle dielectric function and ϵ_m is the dielectric function of the surrounding medium. This quantity will be maximised if the denominator of the fraction tends towards zero, in which case we say a resonance has occurred. If we assume a lossless

Drude model ($\epsilon'' = 0$) with vacuum surrounding the particle, then the frequency at which the resonance will occur is

$$\omega_{pp} = \frac{\omega_p}{\sqrt{3}}, \tag{4.19}$$

which is lower than the surface plasmon frequency ($\omega_{SP} = \frac{\omega_p}{\sqrt{3}}$) for the same choice of materials.

4.5 Near Field and Far Field

For sources of radiation it is convenient to make a mental separation between the near and far field. The far field refers to field components which have a non-negligible amplitude at a distance far from the source, i.e. using conventional detectors this is the field which will be measured. The condition for a non-negligible amplitude is that the electric field should not decay more rapidly than $1/r$, where r is the distance from the source. With this dependence, the intensity (which is measured by detectors) decays with $1/r^2$. A thin shell surrounding the particle will have a surface area of $4\pi r^2$, which means that the intensity integrated over the shell area will be constant given a $1/r^2$ dependence. Thus the total intensity of light does not decrease when moving away from the source, it simply spreads out over a larger surface area. As long as we take into account the angular fraction of light hitting the detector, the measurement will be independent of the distance from the source.

The near field refers to field components which decay quicker than $1/r$. In the vicinity of the source, these field components will dominate in magnitude compared to the far field components. In contrast to the far field, the measured intensity will strongly depend on the distance from the source since the angular integrated intensity decreases with distance from the source. The question of how to measure the intensity of the near field is difficult, since anything which will interact with the near field will change the surrounding of the source, thereby changing the near field produced. Therefore the goal is to measure the near field intensity while having the smallest impact possible on the source. This can be achieved by placing a secondary source (e.g. a fluorescent molecule) close to the source. The secondary source intensity is dependent on the excitation intensity which comes from the near field. This idea is exploited for the detection of extremely low concentrations of molecules in the method of surface enhanced Raman spectroscopy (SERS). In this case, since a Raman process is a two photon process, the signal is proportional to the square of the exciting field. The result is that the high near fields are further magnified, allowing signal boosts in the range of thousands to millions. Another option is that of a shielded tip of a waveguide near the particle. The evanescent fields of the particle can couple into the waveguide through the tip, whereas radiative waves are prevented from coupling due to the below wavelength tip diameter. This is the principle behind scanning near field microscopy (SNOM). Until now we have described a SNOM device in collection mode, however it is also possible to run a SNOM in illumination mode. By sending light into the waveguide, the tip itself will become a source for near fields. These fields can then excite the nanoparticle causing it to emit far field radiation which is then detected. For either mode, the tip is raster scanned near the particle to gain a complete image of the near field strength.

The actual value for the near field found via measurements will vary strongly upon the position with respect to the particle. In general we desire a single figure of merit that describes the near field surrounding the nanoparticle. For sensing applications the highest field enhancement in the near field might be used, even though this is dependent on position near the particle. For photovoltaic applications, we are more interested in the average field enhancement surrounding the particle since the absorption in a material is based on the volume integral of the electric field in that material. The average field strength in a thin shell surrounding the particle could be used, however the results will depend strongly on the shell thickness. Therefore to keep the figure of merit equal for different particles, we evaluate the field strength only at the particle surface. That means integrating the field over the surface of the particle. This is the definition of the near field cross section which will be used during the present work. This might correspond to the measured value if it could be integrated over a very thin shell around the particle, however the measurement device is unlikely to be able to measure the field strength directly at the particle surface. Therefore the near field cross section is a purely theoretical concept used to quickly evaluate the near field strength around a nanoparticle.

4.6 Plasmonic Materials

Using the theoretical description of the optical properties of isolated spherical particles from chapter 3, we move on to looking at the realistic choices available for optically active plasmonic materials. The principle restriction is simply to have a high density of free charge carriers, leading to a localised surface plasmon resonance in the optical regime. This describes most metallic materials therefore we impose further criteria in order to find the most useful materials. The criteria are (listed in order of importance from most to least):

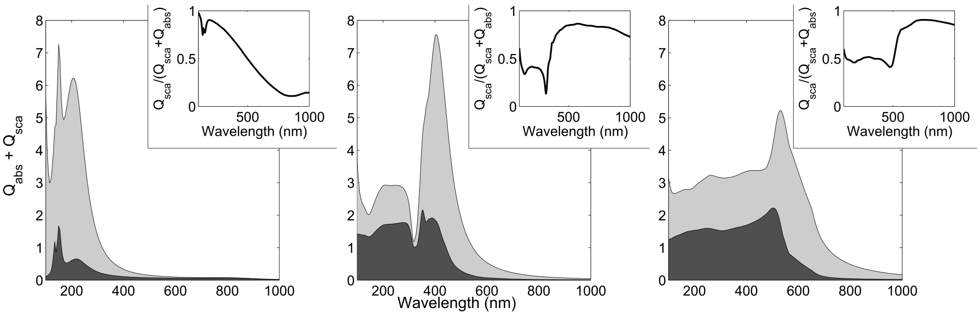

Figure 4.5: The normalised extinction cross section Q_{ext} decomposed into absorption Q_{abs} (dark grey) and scattering Q_{sca} (light grey) as a function of wavelength, for three different materials. The materials and radii are Al r = 30 nm (left), Ag r = 50 nm (middle) and Au r = 80 nm (right). The particles are in vacuum. The inset in each case shows the scattering efficiency over the same wavelength range.

- Low losses due to inter-band transitions in the optical region.
- Good chemical stability.
- Abundant/low cost.

Depending on the application these criteria may be more or less important. For example sensing applications may not require low cost materials if it means outperforming other sensing techniques. However for the application to solar energy, all three of these criteria are critical. Unfortunately no one material can fulfill all these criteria. The most important criterion for optical applications is the first one since if there are high inter-band transition losses, they will heavily damp the plasmonic resonance, meaning that the desired plasmonic effect cannot be reached. This rules out most transition metals since the filling of the d shell leads to a large amount of inter-band transitions [46]. The alkali metals avoid this problem but fall at the next hurdle, they are extremely reactive with both air and water, meaning that integration in realistic devices would be extremely challenging . The final column of transition metals contains the noble metals Al, Cu, Ag and Au. These four materials avoid inter-band transitions in at least part of the optical spectrum. They are relatively stable (Au being superbly stable, while Al, Ag and Cu are prone to forming self limiting oxide layers). Of these four materials, Ag and Au have the most desirable optical properties (low losses) which is the reason why most plasmonic research has been conducted on particles made from one of these two materials [47–49]. However they are both rare elements and carry with them a high cost. Cu and Al which may not perform as well are significantly less expensive which may end up being crucial for realistic device applications. Al has a high plasma frequency meaning that it might be useful for different applications compared to Ag and Au. Cu however has a similar plasma frequency to Au, but with higher losses it can be generally considered a cheaper but worse version of Au.

Figure 4.5 shows the normalised extinction cross section for the materials Al, Ag and Au, decomposed into the scattering (light grey) and absorption (dark grey). The insets show the scattering efficiency for each material, that is the ratio of scattering to extinction. For the application to photovoltaics, we desire for the scattering efficiency to be as high as possible. For the case of Al the resonance lies primarily in the UV region, this is due to the high density of free charge carriers in Al. Although redshifting of the resonance is possible, which will be discussed in detail later, it should be noted that a plasmonic resonance in Al will always be at a higher frequency compared to Ag and Au. The inset shows the scattering efficiency, which while high at the surface plasmon resonance wavelength at around 200 nm, drops in the optical region and near infrared due to an inter-band transition centered around 800 nm. Ag shows a plasmonic resonance at around 400 nm wavelength, with both a high scattering efficiency and a high total value for the extinction. This means that Ag has the strongest interaction with light at optical frequencies and explains why this material is heavily studied in the literature. Below 350 nm inter-band transitions drop the scattering efficiency from over 90% to less than 50% meaning that Ag is not a good material for applications in the UV region. The behaviour for Au looks comparable to Ag, with a plasmonic resonance around 550 nm and inter-band transitions beginning at wavelengths below this. Therefore for applications that require the complete optical region, Au might be unsuitable due to optical losses at wavelengths below 500 nm. For applications in the red/ near infrared, Au can be a very good material providing lower losses than Ag due to a higher conductivity.

4.7 Nanoparticle Radius

As previously alluded to, the wavelength of the plasmonic resonance can be shifted. One of the possibilities for doing this lies in the particle size. Figure 4.6 shows the normalised scattering cross section for an Ag nanoparticle in air as a function of both wavelength and particle radius. Starting with the smallest particle radii the spectral behaviour is relatively simple, there is a single resonance peak at around 350-400 nm. Since the particle is small compared with the wavelength, the dipole approximation is valid and we obtain a dipole response. As the radius increases and becomes comparable with the wavelength, the Mie theory size parameter will also increase. For a larger size parameter, the Mie coefficients for higher order multipoles will become significant. This is visible as an extra peak emerging in the scattering cross section, firstly at a radius of around 100 nm (the quadrupole mode) and another at around 150 nm (the octupolar mode). These modes appear due to the boundary conditions which determine the Mie coefficients being dependent on the size parameter of the nanoparticle. We can also observed that each individual resonance is redshifted due to the increasing particle radius. This is a

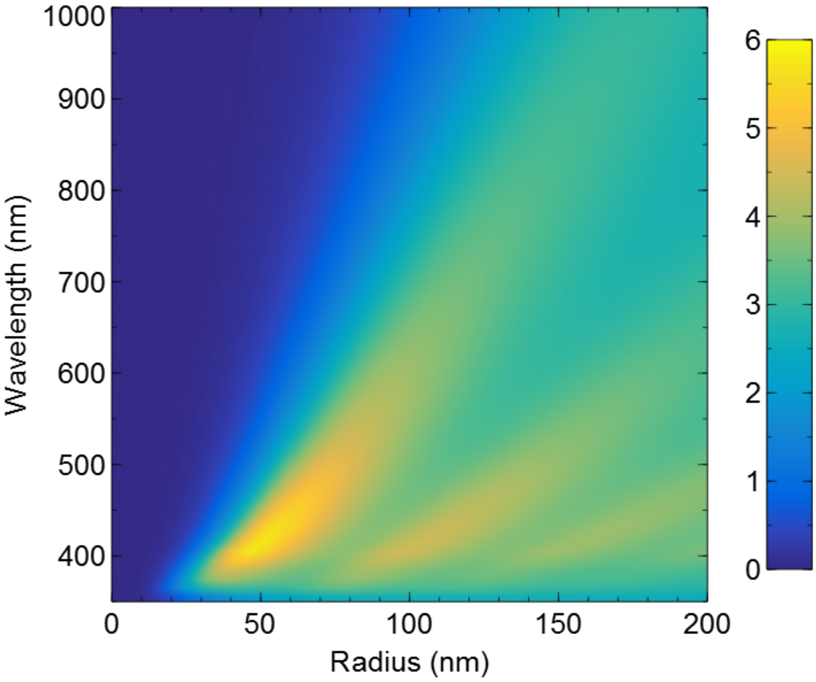

FIGURE 4.6: The normalised scattering cross section (Q_{sca}) for a spherical Ag particle in vacuum as a function of both the particle radius and wavelength.

retardation effect and is a consequence of the particle having a finite size, this will be discussed in more detail in the following chapter on numerical methods where the optical shifting is decomposed into particle size increases in different directions with respect to the light incidence and polarisation vectors. For now it is enough to know that particle resonances can be redshifted by increasing their size and that this kind of shifting tends to broaden the resonance and decrease the peak intensity.

4.8 Surrounding Material

Another option for shifting the plasmonic resonance is by changing the surrounding medium. All the results shown until now were for a surrounding medium of air which is unlikely to be encountered in reality. Figure 4.7 shows a plot similar to 4.6, with the radius dependence being replaced by a dependence on the surrounding medium refractive index. In this case the behaviour is simpler, the resonance position is linearly redshifted with an increase in the surrounding medium refractive index. The resonance also increases in strength as it is redshifted, this is opposite to the behaviour seen with the radius dependence where redshifting leads to a decrease in the resonance intensity. This underlies the different physical description for the source of the redshifting. For the case of the surrounding material refractive index, the reason can be understood by returning to the simplest model of dielectric media. In this model we assume that each

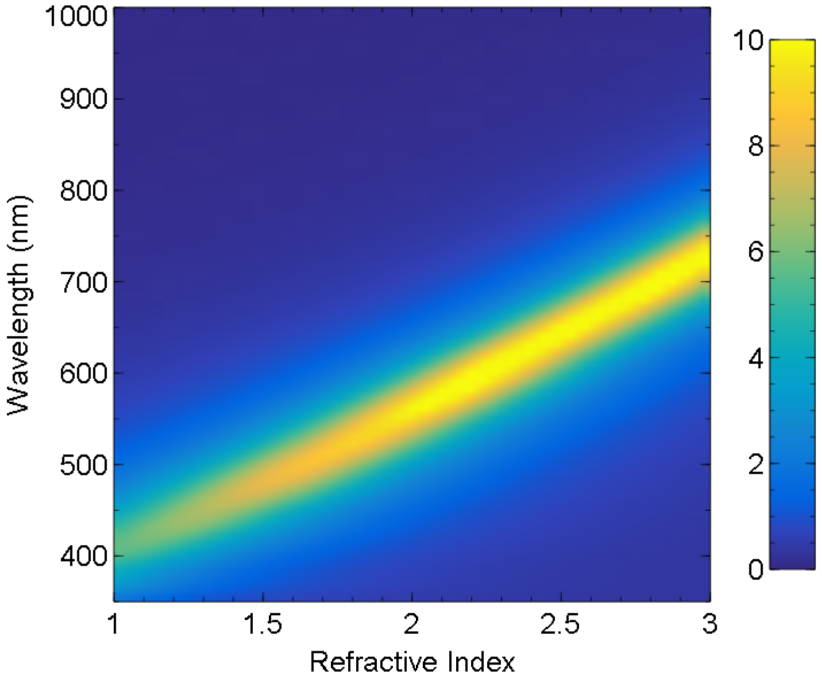

FIGURE 4.7: The normalised scattering cross section (Q_{sca}) for a spherical radius 50 nm Ag particle as a function of both the surrounding medium refractive index and wavelength.

atom in the dielectric medium is represented by a single dipole. When the plasmonic resonance occurs, there will be associated surface charges at the sphere/outer medium interface. These surface charges are able to polarise the surrounding medium. That means where there is positive surface charge, the negative ends of the dipoles are attracted to the particle and the positive ends are repelled, and vice versa for negative surface charge. The net effect of the polarisation charge and the surface charge is that they will partially cancel out, and the more polarisation charge there is, the more they are able to cancel each other out. More polarisation charge means that the dielectric material has a higher number of dipoles per unit volume which is equated to a higher refractive index. Therefore we can say that a higher refractive index causes the surface charge to be more compensated for during a plasmonic oscilation. Now we return to the dynamics of the plasmonic oscillation, the restoring force for the LSPR is the surface charge build up on the other side of the particle. If that surface charge is reduced, then the restoring force will be weakened. In any system of simple harmonic motion, a weaker restoring force leads to lower frequency and higher amplitude oscillations, which fits in this case since we observed a redshifting and increase in Q_{sca}.

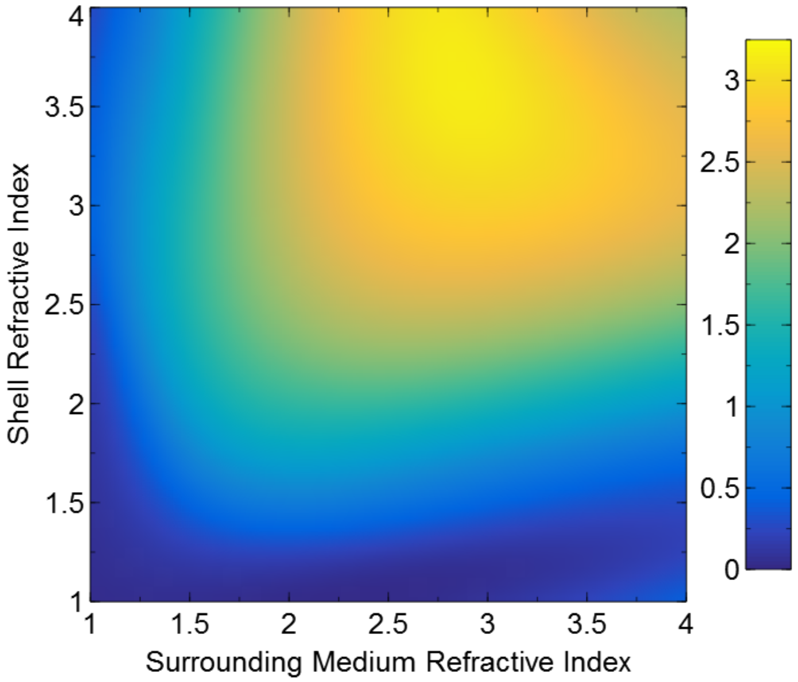

FIGURE 4.8: The spectrally integrated normalised scattering cross section (Q_{sca}) for a radius 35 nm spherical Ag core 10 nm thickness shell in vacuum as a function of the refractive index of both the shell and surrounding medium. The spectrum was integrated over the wavelength range 500 nm to 1100 nm, and normalised to the same range.

4.9 Core Shell Particle

As discussed in chapter 3, it may be necessary to use plasmonic core - dielectric shell particles for successful integration of plasmonic particles into devices. The shell also provides further design parameters which we can use to optimise the system. We first investigate a core-shell particle consisting of a radius 35 nm Ag core surrounded by a radius 45 nm shell giving a total shell thickness of 10 nm. The geometry has been previously shown in fig. 3.1. The shell refractive index and the outer medium refractive index will be varied from one to four in order to investigate the effect on the plasmonic resonance of different combinations. Since plasmonic effects are resonant, they will always work in a limited spectral region. Depending on the application this can be a limitation or a benefit. For the application proposed here, that of solar energy we require a broadband resonance covering a large spectral region. For ultra-thin chalcopyrite photovoltaics, the region lies between 500 nm and 1100 nm wavelength. Thus we have chosen this spectral region to evaluate our results.

Figure 4.8 shows the spectrally integrated normalised scattering cross section (Qsca) for both shell and surrounding medium refractive index varying from one to four. This gives the average value of Qsca within the spectral region and is calculated via

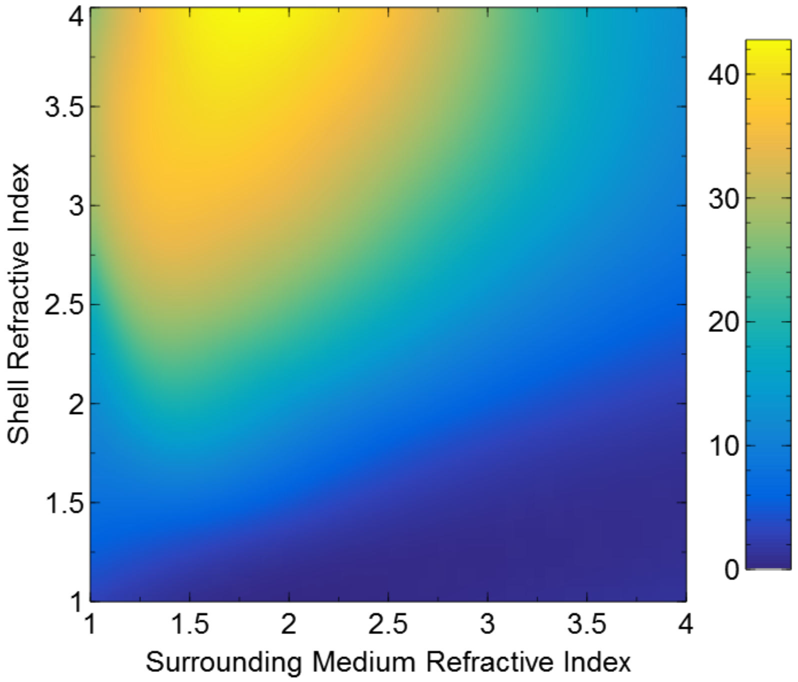

FIGURE 4.9: The spectrally integrated normalised near field cross section (Q_{nf}) for a radius 35 nm spherical Ag core 10 nm thickness shell in vacuum as a function of the refractive index of both the shell and surrounding medium. The spectrum was integrated over the wavelength range 500 nm to 1100 nm, and normalised to the same range.

$$< Q_{sca} >= \frac{\int_{\lambda_{min}}^{\lambda_{max}} Q_{sca}(\lambda) d\lambda}{\int_{\lambda_{min}}^{\lambda_{max}} d\lambda}. \tag{4.20}$$

Similarly fig. 4.9 shows the spectrally integrated normalised values of Qnf for varying shell and surrounding medium refractive index. The near field cross section is evaluated at the outermost particle boundary, in this case the outer shell boundary. Since the range of refractive indices simulated are identical, it means that the upper left half corresponds to cases where the shell material refractive index is higher than the surrounding medium refractive index. The opposite will be true for the lower right half of the image. The general trend is that we see a larger integrated value in both Qnf and Qsca if the shell has a higher refractive index than the surrounding material.

In order to investigate the cause of this effect in more detail, we present also the near fields for two core-shell particles which exemplify the trend. Figure 4.10 shows the electric field strength around an Ag/dielectric core/shell particle in a dielectric medium. In part (a) the medium has a higher refractive index compared to the surrounding (3 compared to 1) with the result being that the resonance is largely extracted outside of the shell. This will lead to a higher near field cross section but also a higher scattering

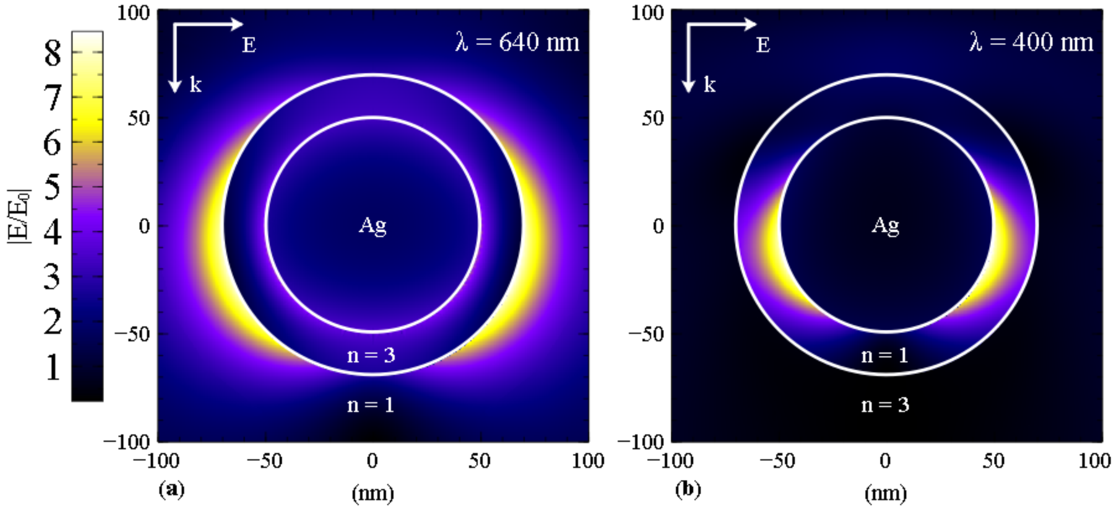

FIGURE 4.10: The total electric field strength in the plane of polarisation for an Ag/dielectric core/shell particle in a dielectric medium. In part (a) the shell has a refractive index of 3 and the medium a refractive index of 1. In Part (b) these values are reversed with the shell being 1 and the medium being 3.

as the near field corresponds to the dipole source which extends into the far field. In Part (b) the roles are reversed, the shell has a refractive index of 1 while the medium has a refractive index of 3. In this case the plasmonic resonance is strongly confined inside the shell, thus lowering both the near field and far field scattering cross sections.

To understand where this comes from, consider the electrostatic case shown in fig. 4.11. First we consider the electric field applied to pure dielectric particles in a dielectric background. In part (a) the particle has a high refractive index with a low surrounding medium refractive index, while in part (d) the two refractive indices are reversed. In part (a) the surface charge produced will act against the applied field, thereby lowering the total field inside the particle. Likewise the opposite is true in part (d), where the lower refractive index will enhance the field inside the particle due to surface charges aligned with the applied field. We now move to part (b) and (e), surface charge on the metallic particle always acts to screen the electric field inside the particle. Finally we come to the core shell particles shown in (c) and (f). Clearly in the case of (a) and (b), the surface charges are aligned with each other therefore the fields act in the same direction inside the particle, meaning that the net effect of the plasmonic core will be amplified by the dielectric shell. However for (d) and (e) the surface charges have opposite polarity therefore the fields are antiparallel and will act against each other, meaning that the net effect of the core shell particle will be to lessen the effect of the plasmonic core. Since these surface charges are the source of the dipole radiation outside the particle, the scattering will also be enhanced or lowered by the presence of the dielectric shell.

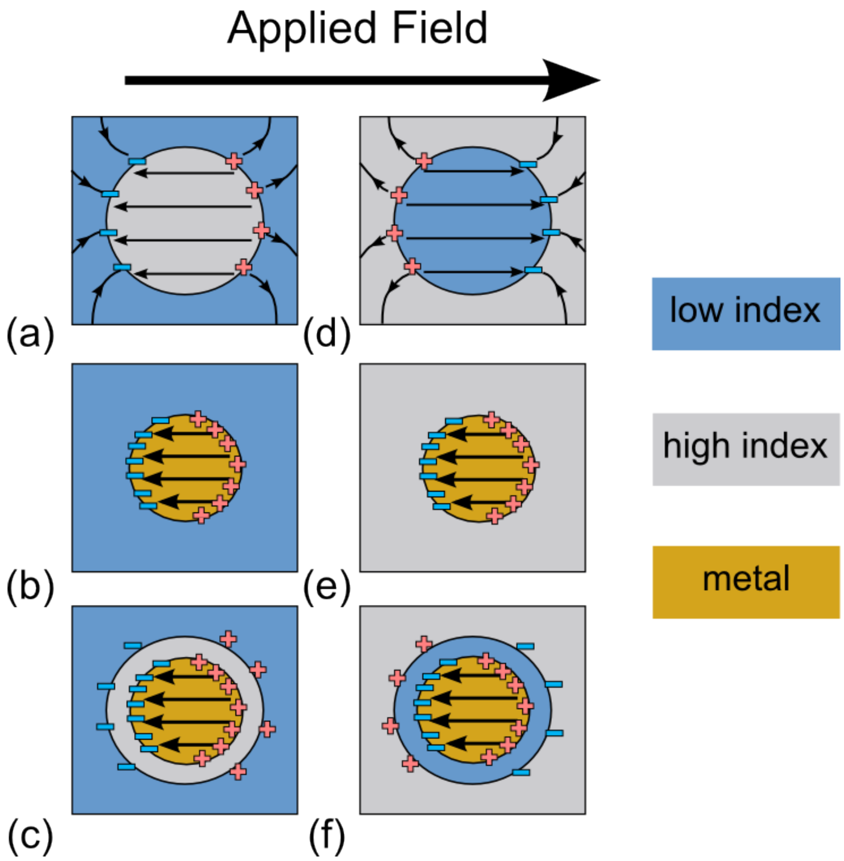

FIGURE 4.11: The response to an applied electric field for different core shell particles in the electrostatic regime. Parts (a-c) show a low index background with a high index shell, while parts (d-f) show a high index shell with a low index background. Parts (a) and (d) show the response of dielectric particles without a metallic core. Parts (b) and (e) show the result of the metallic core without the dielectric shell. Parts (c) and (f) show the net combination of parts (a-b) and (d-e) respectively.

Extending this outside of the electrostatic regime, the effect of an applied oscillating field on solid dielectric particles will be to create oscillating dipoles which are either in phase with the applied field (for a particle with a higher n than the surrounding) or it will be in antiphase with the applied field (for a particle with a lower n than the surrounding). The dipole radiation from the shell then interacts with dipole radiation from the plasmonic core providing either constructive or destructive interference. Higher order modes of both the shell and the core will also follow the same trend.

The normalised near field cross section has its highest integrated value for a very large value of $m_2 = n_{shell}/n_{surrounding}$, peaking at $m_2 = 2.2$. The maximum value for the Qsca comes at a smaller value of $m_2 = 1.28$, however this could be due to the scattering resonance being more strongly redshifted by a higher local refractive index, meaning that for high values of m_2, the plasmonic resonance is shifted out of the spectral region of interest therefore no longer contributing to the integrated value. This could

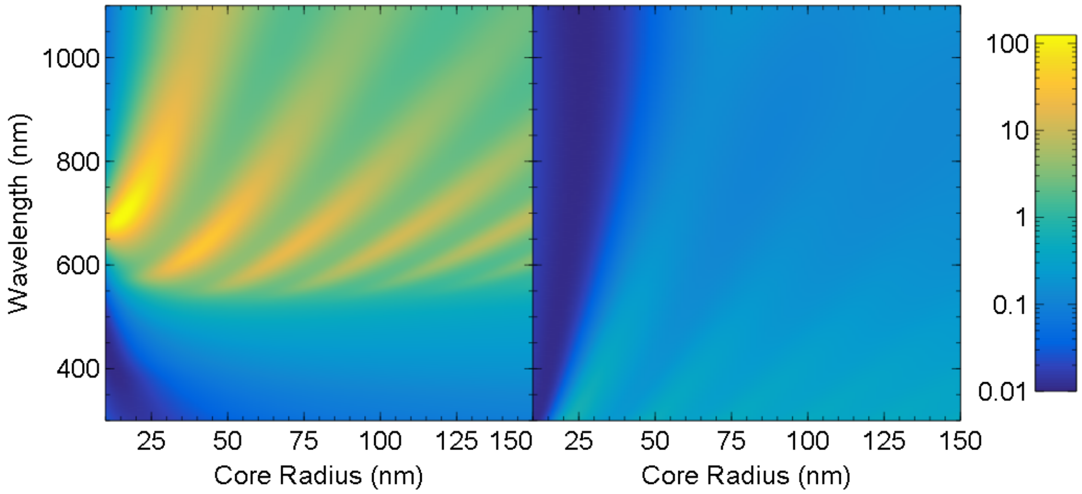

FIGURE 4.12: The normalised near field cross section (Q_{nf}) for a spherical Ag core 10 nm thickness shell in vacuum as a function of the core radius and wavelength for two different shell materials. The two different materials are AlSb (left) and SiO_2 (right). The colour scale is logarithmic.

be counteracted by using either a smaller particle, or a material with a higher plasma frequency.

Given this insight into the general properties of core shell particles, we turn to look at more concrete examples. The idea of using an isolating dielectric shell for metallic particles has been proposed in the literature typically with SiO_2 [50] or TiO_2 [51, 52], however more exotic materials have been used depending on the application [53–55]. However, it seems that until now little thought has been given to the optical properties of the isolating layer. We have shown that the optical performance of plasmonic nanoparticles is significantly enhanced when surrounded by a shell with a higher refractive index than the surrounding material. For the case of organic photovoltaics and dye sensetised solar cells, where the use of plasmonic particles has shown to be promising, this is fairly easy to achieve. That is due to organic materials typically having a low refractive index compared to inorganics. If we instead consider nanoparticles in direct contact with chalcopyrite material, the choice of shell material becomes more limited. This is because CIGSe has a refractive index ranging from 2.8 to above 3 in the visible region. Typical isolating shell materials like SiO_2 or TiO_2 will have a significantly lower refractive index than the surrounding CIGSe, limiting the scattering and near field cross sections. Casting the net for available shell materials a little wider, we turn to the material AlSb, which is a semiconductor with a band gap in the blue optical region and a high refactive index throughout the optical region.

This is demonstrated in fig. 4.12 where the near field cross section is shown as a function of core radius and wavelength for both an AlSb and an SiO_2 shell. A 10 nm shell thickness is used for all core radii, in order to properly isolate the metallic core. The outer medium

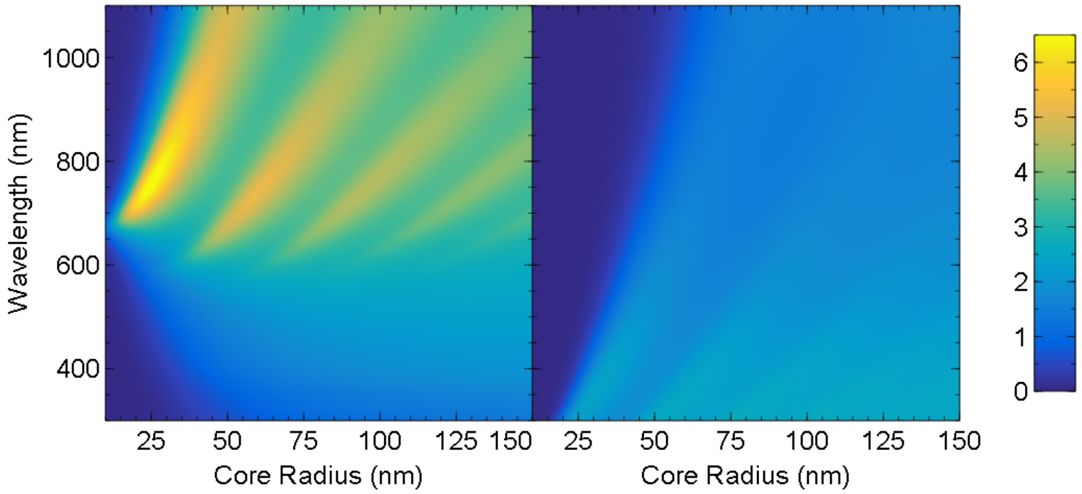

FIGURE 4.13: The normalised scattering cross section (Q_{sca}) for a spherical Ag core 10 nm thickness shell in vacuum as a function of the core radius and wavelength for two different shell materials. The two different materials are AlSb (left) and SiO_2 (right).

is assumed to be CIGSe without absorption, this is an approximation necessary since the outer medium for a Mie theory calculation must be non-absorbing, however in the weakly absorbing regime it is a good approximation. The colour scale showing the value of Q_{nf} is logarithmic, meaning that the values of Q_{nf} achievable using the AlSb shell are orders of magnitude higher than those reachable using a SiO_2 shell. Since we are varying the radius of the plasmonic core, we see the typical resonances due to different orders of multipole arising due to the increased particle size. The dipole mode shows the strongest resonance, however it may be more beneficial to use a slightly larger particle to exploit multiple resonances for a broadband effect. Similarly in fig. 4.13 the same comparison is made between the two different shells but for Q_{sca} instead of Q_{nf}. In this case the scale is linear since the difference between the Q_{sca} for AlSb and SiO_2 is smaller. Within the spectral region of interest, the AlSb shell still shows a value of Q_{sca} that is one to six times larger than for the SiO_2 shell. It is clear that whatever the optimal value for the core radius, the values of Q_{nf} and Q_{sca} will be much larger using an AlSb isolating shell.

The previous analysis can equally be performed with other material systems. The fast Mie theory implementation developed as part of the current work allows for the kinds of multidimensional data sets presented in this chapter to be evaluated in a few seconds on a standard desktop computer. We believe that organic and inorganic optoelectronic systems involving the use of plasmonic core/isolating shell particles can greatly benefit from this kind of optical optimisation. For a quantitative prediction of the actual absorption enhancement obtained using these nanoparticles requires a simulation of the entire integrated device. Therefore we move on to the second chapter where we discuss a numerical approach to solving plasmonics problems that no longer contain symmetry.

Chapter 5

Finite Element Method

The key tool to solving the equations describing plasmonics in the first chapter was exploiting the symmetry of the problem. Real devices may not have such symmetries and therefore a more robust method of solving Maxwell's equations needs to be developed. Thus we turn away from analytical solutions to the world of numerics. We first discuss some of the most prominent numerical methods for nanooptical applications, then focus on our method of choice, the finite element method. The following chapter is devoted to examples of this method including novel techniques used to speed up simulations.

5.1 Finite Element Method

The most visible part of finite elements is the discretisation of the computational domain into elements, be they triangular, rectangular or any manner of shape. However this does not emphasise the mathmetical underpinning of the method. In fact we can imagine the computational domain being discretised with a single element. Therefore even though the breakdown into individual elements is one of the strongest advantages of the finite element method, we will leave it until the end of the section. We firstly try to understand the mathematics behind the method.

The first step is to understand the difference between the operational form and variational form of a problem. The operational form is the standard form for a differential equation, e.g. we want to find the function $u(x)$ that follows the following differential equation

$$-\frac{d}{dx}\left(p(x)\frac{d}{dx}\right)u(x)+q(x)u(x)=f, \tag{5.1}$$

$$\left[-\frac{d}{dx}\left(p(x)\frac{d}{dx}\right)+q(x)\right]u(x)=f, \tag{5.2}$$

$$Lu(x)=f. \tag{5.3}$$

Where all of the differential parts and other functions (here $p(x)$ and $q(x)$ are arbitrary functions) are contained in the *operator* L. This is a convenient way to write all of the difficult parts of the equation. To describe the variational form we first need to remind ourselves of the definition of the inner product

$$\langle \phi,\psi\rangle = \int \phi\psi^* d\Omega. \tag{5.4}$$

This is the functional equivalent of the scalar product for vectors. With that definition in mind, we define the following functional

$$I(v) = < Lv, v > -2 < f, v > . \tag{5.5}$$

The special feature of this functional is the following: $I(v)$ is minimised for $v = u$ only if the first derivative vanishes there. The condition for the derivative to vanish is the original equation $Lu = f$. Thus the problem of minimising I and inverting L are equivalent. To see this, let us assume that L, v and f are real numbers

$$I(v) =Lv^2 - 2fv, \tag{5.6}$$

$$\frac{dI}{dv}|_{v=u} =2(Lu-f)=0, \tag{5.7}$$

$$\rightarrow Lu =f. \tag{5.8}$$

Notice that this is only true if L is a positive number, otherwise the minimum is at $v = -\infty$. If we return to the world of functions and operators, this is equivalent to ensuring that the operator L is positive definite. Now assume that the functional I has a minimum at $v = u$, if we add any vector to u then we must arrive at a value of I larger than $I(u)$ since it is the minimum value. For any constant number ϵ and any vector v, the following must be true

$$
\begin{aligned}
I(u) \leq I(u+\epsilon v) = &< L(u+\epsilon v),(u+\epsilon v) > -2 < f,(u+\epsilon v) >, && (5.9)\\
&= < Lu, u > + < L\epsilon v, \epsilon v > \\
&+ < Lu, \epsilon v > + < L\epsilon v, u > \\
&-2 < f, u > -2 < f, \epsilon v) >, && (5.10)\\
&= I(u) + 2\epsilon[< Lu, v > - < f, v >] + \epsilon^2 < Lv, v > . && (5.11)
\end{aligned}
$$

Since ϵ can be positive or negative, and the rhs must be larger than the lhs, it must be true that the coefficient of ϵ vanishes which establishes

$$< Lu, v > - < f, v >= 0. \tag{5.12}$$

This is the standard motivation for the finite element method. In this case the example partial differential equation (5.1) was equivalent to the Helmholtz equation from physics, however we wish to solve Maxwell's equations. For the case of Maxwell's equations L is not a positive definite or even self adjoint matrix. However it has been shown that equation 5.12 can still be solved [56], allowing us to obtain solutions to Maxwell's equations.

Equation 5.12 looks fairly innocuous, but it changed things significantly. The problem is now stated in the so called weak formulation. It is called weak since we no longer require $Lu = f$, instead requiring $< Lu, v >=< f, v >$ for all v. To understand this difference we reference an example from physics, the so call Dirac delta function. This function can be used to discribe the charge distribution of a single point source. It has the following properties

$$
\begin{aligned}
\delta(x) =&\infty, && x = 0, && (5.13)\\
\delta(x) =&0, && x \neq 0, && (5.14)\\
\int_{-\infty}^{\infty} \delta(x)dx =&1. && && (5.15)
\end{aligned}
$$

We might ask, how can this function be used in physics, since it gives the value of the charge distribution as being infinite at the origin, something that is clearly unphysical. However this function is only ever evaluated with respect to an integral over a region of space, giving a defined value. In this same sense, the solutions obtained from the weak formulation only make sense in the integral form, meaning that there are fewer restrictions on the types of functions used. This step is not necessary to solving the problem in principle, in practice it is essential since it allows us to consider trial functions with less strict boundary conditions. This is crucial to obtaining a tractable and efficient solution.

Until now we have described the variational principle which is used in the finite element method. Remember that we introduced a trial function made up from basis functions. If we choose functions which are defined over the whole computational domain, it may be quite difficult to obtain a basis which comes close to approximating the real solution. Therefore the finite element approach is to subdivide the computational domain into elements. Each element defines a geometrical region and a particular local function which can be expected to approximate the full solution within the geometrical region. Typically polynomial functions are used for their simplicity.

The great advantage of finite elements over other methods is that the elements do not have to be layed out on a structured grid. That means that irregular and curved surfaces can be very accurately reproduced without stair-casing errors. Additionally, the resolution of the elements can be increased in regions of high field gradients, meaning that computational effort is used efficiently by having a fine approximation where it is needed, and a rougher approximation where it is sufficient.

As we have seen, Maxwell's equations need to be expressed as a functional to minimise, in order to use the finite element method. By applying the time harmonic ansatz we may reduce Maxwell's equation to one differential equation [57]

$$\frac{1}{\epsilon_0 \epsilon_r} \nabla \times \frac{1}{\mu_0} \nabla \times \mathbf{E} - \omega^2 \mathbf{E} = 0. \tag{5.16}$$

We then multiply this with the test function $\bar{\Phi}$ and integrate over the computational domain to obtain a functional

$$\int \bar{\Phi} \cdot \left[\frac{1}{\epsilon_0 \epsilon_r} \nabla \times \frac{1}{\mu_0} \nabla \times \mathbf{E} \right] - \omega^2 \bar{\Phi} \cdot \mathbf{E} d^3 r = 0. \tag{5.17}$$

We then minimise the integral with respect to variations in the test function $\bar{\Phi}$.

The first approach to increasing the accuracy of a finite element computation is to use smaller elements. If any curved surfaces are involved in the geometry, this will help to better resolve those surfaces. More importantly the polynomial basis functions are able to better describe the full solution over a smaller region. The second approach to increasing the accuracy is to use a higher order of polynomial basis function. If there is some variation in the full solution over the region of a particular element, then it can be expected that a higher order element is able to better resolve this variation.

The particular finite element solver used during this work is JCMsuite [57]. Which is an adaptive finite element solver especially suited to problems in nano-optics. In particular, it provides features such as the ability to evaluate scattered fields in the far field and to couple FE simulations to scattering matrix simulations in order to extend the size of domain capable of being simulated by the FEM. This will be covered in more detail in chapter 11

5.2 Boundary Conditions

The choice of boundary conditions when performing FEM simulations is crucial. For the scattering problem, three principle boundary conditions are useful. These are periodic Floquet type, perfect electric /magnetic conductor type and perfectly matched layer (PML) type. Periodic boundary conditions are used to turn a finite simulation into an infinitely extended one, by periodically repeating the simulated unit cell. For nanostructured solar cells, the dimensions of the device in the x-y plane are so much larger compared to the nanoscale, it is a good approximation to assume that the device extends infinitely in these directions. For the case of a structure that contains a geometric periodicity, these kinds of boundary conditions perfectly describe the system. For systems with a geometry that is continuously varying in the x-y plane, often in a random fashion, periodic boundary conditions must be used carefully. Generally periodic boundary conditions may still be imposed, with the caveat that the domain be large enough in the x-y plane such that artifacts of the periodicity are sufficiently small. If the period of repetition is sufficiently large then any diffraction effects will be minimal.

The second kind of boundary condition is the perfect electric or magnetic conductor. When placed in a plane perpendicular to the electric or magnetic polarisation, respectively, these act as perfect mirrors. These boundary conditions can be useful in order to reduce the computational effort required on a simulation by exploiting the symmetry present in the system. This is achieved by placing the perfect conductor conditions at mirror planes in the system and simulating only the reduced geometry. A similar boundary condition that exploits symmetry is the cylindrical boundary condition. This assumes that the geometry has rotational symmetry around a central axis. In this case the geometrical distribution in the r z plane defined by a particular θ can be converted to a 2D problem in the x-y plane. The θ dependence is expanded into a set of basis functions valid for cylindrical symmetry and the 2D problem is solved repeatedly in order to obtain the expansion coefficients. Due to the reduced complexity of 2D problems in comparison to 3D ones, this method is much less computationally expensive, despite the need for multiple 2D simulations compared to a single 3D one.

The final boundary condition that needs to be considered is a specific form of the transparent boundary condition called the perfectly matched layer. The transparent boundary condition seeks to allow outgoing fields to leave the computational domain without any artificial reflections at the computational domain boundary. The perfectly matched layer achieves this aim by an analytic continuation of the real valued position into the complex domain [58]. To demonstrate in a simplified way how this works in one dimension, consider the electric field of a wave propagating in the x direction with polarisation in the y direction that we wish to be attenuated

$$E(x) = \hat{\mathbf{e}}_{\mathbf{y}} \exp\left[\frac{ix(n+ik)2\pi}{\lambda}\right], \tag{5.18}$$

$$E(x) = \hat{\mathbf{e}}_{\mathbf{y}} \exp\left[\frac{ixn2\pi}{\lambda}\right] \exp\left[\frac{-xk2\pi}{\lambda}\right], \tag{5.19}$$

where n and k are the real and imaginary parts of the refractive index of the material and λ is the wavelength. A material which has $k > 0$ will be attenuated due to absorption, as can be seen in the second term in the second equation. In contrast, a material with $k = 0$ will not be attenuated at all. Gain materials with $k < 0$ are not considered. Typically the attenuation offered by the k value is not enough to prevent unwanted boundary reflections and we would like a framework in which materials with $k \geq 0$ can be attenuated. This can not be accomplished by increasing the value of k since this would cause a boundary between a material where the k value was lower and a material where the k value was higher, such a material interface would again lead to unwanted reflections.

The argument of the exponential in equation 5.18 is mainly determined by the product of the imaginary unit, the position and the (complex) refractive index. The product of the imaginary part of the refractive index with the imaginary unit produces the real exponential decay which causes attenuation of the wave. If we now consider that not only the refractive index but also the position could be a complex quantity, we can redefine the position as $\tilde{x} = x + i\chi$. Given this definition, the expression for the electric field becomes

$$E(x) = \hat{\mathbf{e}}_{\mathbf{y}} \exp\left[\frac{i(x+i\chi)(n+ik)2\pi}{\lambda}\right], \tag{5.20}$$

$$E(x) = \hat{\mathbf{e}}_{\mathbf{y}} \exp\left[\frac{i(xn+\chi k)2\pi}{\lambda}\right] \exp\left[\frac{-(xk+\chi n)2\pi}{\lambda}\right], \tag{5.21}$$

meaning that an extra source of attenuation is introduced due to the χn term. Using this method the computational domain is slightly enlarged due to the need to also simulate the fields inside the PML. PML boundary conditions allow us to simulate isolated systems, this means that the response of single nanoparticles can be investigated. An additional advantage is that the Fourier transform of the outgoing wave has a continuous range of k values meaning that the angular scattered field distribution can be obtain for all angles. This allows the far field scattered distribution to be obtained from isolated systems.

5.3 Random Particle Arrays

As stated earlier, one method to deal with random particle arrays is to simulate a large number of particles and apply periodic boundary conditions in the x-y plane. This has the problem that artificial periodic effects may nevertheless occur, and that the size in the x-y plane is limited due to computational constraints. This means that only a small number of particles may be simulated which will give a very poor approximation to the actual statistical distribution of particles present.

In contrast a method which seeks to fully utilise the complete statistical distribution of particles is that of averaging single particles. This method involves performing a statistical analysis of an image of particles. In this instance, only the size and shape of the particle is important. After the statistical distribution describing the size and shape has been obtained, a simulation of a single particle of each size and shape is performed. Finally to obtain the average response of the array we calculate the expectation value taking into account the statistical distribution. As an example, if the reflection for each wavelength (λ) and particle size (x) is known, and the particle size is normally distributed with a known mean (μ) and variance (σ^2) then the expected reflection will be

$$< R(\lambda) >= \frac{1}{\sigma\sqrt{2\pi}} \int_{-\infty}^{\infty} R(x, \lambda) e^{\frac{(x-\mu)^2}{2\sigma^2}} dx. \tag{5.22}$$

Since $R(x, \lambda)$ is an unknown function which can only be evaluated pointwise, this integral must be evaluated numerically. The advantages of this approach are as follows

- For axisymmetric particles, the simulation geometry can be significantly simplified using cylindrical boundary conditions, allowing for faster calculations
- The statistical distribution for the particle size and shapes may be arbitrarily well approximated
- Other statistical distributions can be trivially calculated providing R(x,λ) is known.

Let us now examine these points in more detail. If the effects of interparticle interactions are negligible, perfectly matched layer boundary conditions are appropriate for simulating the single particle response. If the particle has a further symmetry around the axis of rotation, a cylindrical coordinate system may be imposed. This means that although many different particle sizes must be simulated, the combined time to simulate the different sizes may be less than the time to simulate a single array of particles. The isolated method allows the statistical distribution to be arbitrarily well approximated. Returning to our previous example, if $R(x, \lambda)$ is evaluated for more values of (x) then the numerical integral will converge towards the analytical integral shown in equation 5.22.

Once the various optical responses as a function of particle size $R(x, \lambda)$, $T(x, \lambda)$ and $A(x, \lambda)$ are known, the probability density function describing the probabilities to find a particle for each size x can be easily changed by choosing a new analytical form for the probability density function. The effort required involves only reevaluating the integral. When simulating a 3D array of particles, as soon as the statistical distribution of the particles changes the entire area of particles must be simulated again using the new statistics. This means it is very time consuming to compare different statistical distributions when simulating the whole array.

The main disadvantage of the averaging method is that the inter-particle interactions are neglected. These kind of interactions may be categorised in three main ways, near field coupling, far field interference and quenching of optical cross sections. Near field coupling is expected to occur when a significant fraction of particles have an inter-particle distance (edge to edge) small compared to the wavelength. Inter-particle coupling has been shown to strongly affect the optical response of metallic nanoparticles, therefore systems where this kind of coupling is significant will not be well approximated by the averaging method. Far field interference means in this case that the radiation emitted by each particle interacts with other particles. This will usually not have a fixed phase relationship leading to a measurable interference pattern, due to the random nature of the particle distributions. However as we shall see, the presence of internal reflection in layers above or below the particles can enhance this kind of coupling.

The final kind of interaction is optical cross section quenching. The scattering and absorption cross section of metallic nanoparticles may be many times larger than their geometrical cross section at resonance. The physical interpretation of this is that the particle bends the propagation of light in its vicinity causing the particle to interact with an area of light larger than the particle. However if two particles are arranged with overlapping optical cross sections, both particles attempt to bend the light towards themselves. This reduces the amount of light which both particles can interact with meaning a lower optical cross section. This effect will be reduced for sparse arrays of particles, and also for arrays with a wide distribution of sizes (since each size will have a different resonance frequency, and quenching is only significant when the particles have a similar resonant frequency.

Taking these effects into account, we can conclude that for sparse random arrays of nanoparticles, the isolated method should be able to give a good approximation to the experimental optical response.

5.4 Obtaining the Statistical Distribution

To obtain the statistical distribution some experimental data needs to be obtained. Typically a top down SEM image of the nanoparticles will provide information about the particle sizes in the x-y plane and also the distance between particles. The size, orientation and position of each particle can be extracted via standard image processing software, e.g. ImageJ [59]. Once the particle sizes are known, a frequency histogram of those sizes can be generated. A probability density function has the defining feature that the integral of the function over the real domain should be normalised to unity [60]

$$1 = \int_{-\infty}^{\infty} PDF(x)dx. \tag{5.23}$$

Therefore in order to fit the probability density function to the histogram, we first numerically integrate the frequency histogram, then divide all values by the integrated value

$$N = \int_{-\infty}^{\infty} h(x)dx, \tag{5.24}$$

$$\tilde{h}(x) = \frac{h(x)}{N}. \tag{5.25}$$

where $h(x)$ is the original frequency distribution and $\tilde{h}(x)$ is the normalised frequency distribution. This ensures that integrating the frequency histogram gives the value of one. After this a standard least squares fitting technique can be used to find the parameters of the analytical probability density function best fit to the normalised frequency histogram.

5.5 Substrate Far Field Coupling

In the following chapter we will simulate particles that are on a glass substrate. In this case light which is scattered by the particles into the glass substrate can be totally internally reflected inside the substrate. This causes it to interact with the particle array for a second time where it can either be scattered out of the substrate, absorbed by the particle or remain trapped in the substrate. In the isolated single particle simulations used for the averaging method here, it is not possible to include these secondary interactions with the nanoparticle array. A simple way to take this effect into account is to take a portion of the transmitted light and convert this to reflection and absorption. In order to determine how much should be converted we can estimate the amount of trapped light by looking at the angular distribution inside the glass substrate. By integrating the angular distribution for angles higher than the angle of total internal reflection, this will give a lower bound on the amount of trapped light. It is only a lower bound because a fraction of the light will also be internally reflected for lower angles.

Chapter 6

Symmetry Breaking Plasmonics

6.1 Nanoparticle Shape Effects

Now that we have discussed the numerical methods themselves, we can begin to apply them to simulate things beyond the scope of analytical simulations. First we return to looking at a nanoparticle as a function of its size. In 4.6 we showed the scattering cross section dependence on the particle size. However with respect to the principle axes of the incident light, i.e. the direction of propagation and the directions of electric and magnetic polarisation, we have made a change in the particle in all three directions simultaneously. To better understand the effects of particle dimensions with respect to these axes we can instead elongate the particle along each axis separately. Figure 6.1 shows the extinction cross section for four different cases. Firstly a spherical Ag particle with radius 50 nm is taken as a reference. This particle is then elongated while keeping the surface curvature constant, that is, we end up with a cylindrical object with hemispherical faces which have the same radius of curvature as the sphere. This is done to isolate purely the effect of elongation. This elongated particle is then orientated along three different axes, parallel to k, parallel to E and parallel to H. Figure 6.2 shows the same scenarios, but instead of cross section, the electric field strength surrounding the particle in the k-E plane is shown. The wavelength used in each case is the wavelength of peak Q_{sca} intensity from fig. 6.1.

We first consider the elongation in the direction parallel to the incident light (parallel to k). The total intensity of the resonance is greatly increased, this should be expected since our normalisation is to the particle area cross section as seen by the incident light. In this case, the incident light only sees one of the hemispherical faces of the cylinder, meaning that we normalised to an area which is the same size as the sphere, but in

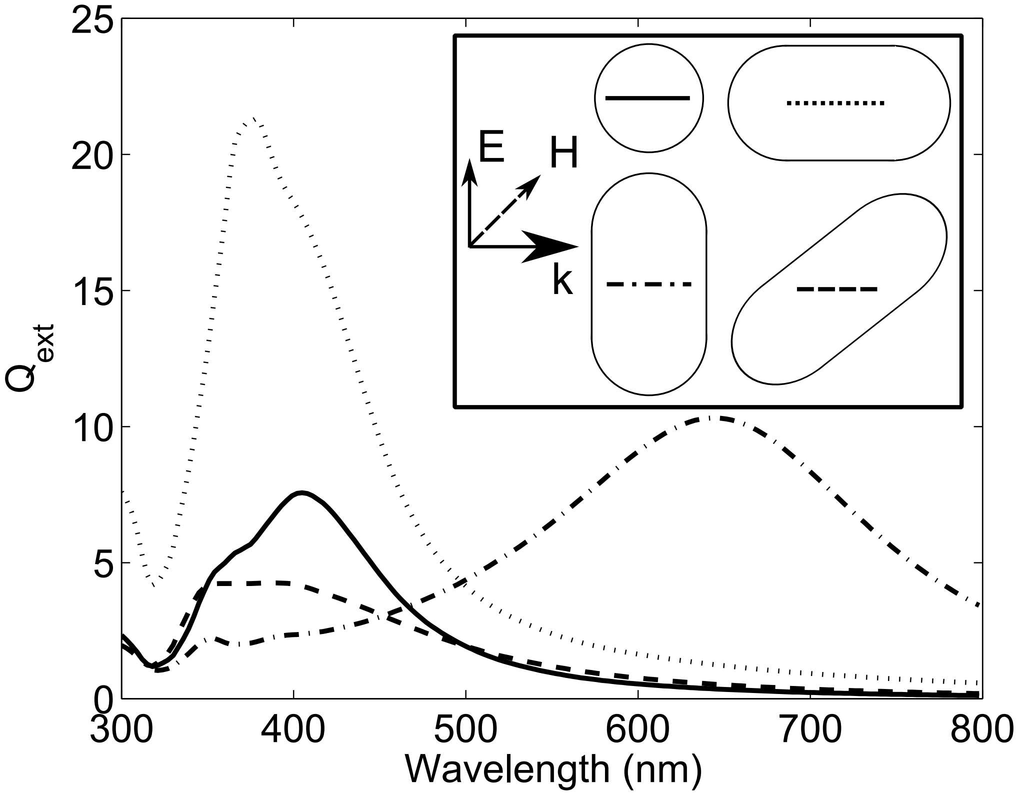

FIGURE 6.1: The normalised scattering cross section (Q_{sca}) for four different scenarios. A spherical Ag particle of radius 50 nm (solid line) is compared to an elongated Ag particle with length 200 nm orientated along three different axes. As shown in the insert the axes are: parallel to k (dotted line), parallel to E (dash dotted line) and parallel to H (dashed line).

this case we have a much larger volume of particle, which should have a strong light-matter interaction leading to more scattering. The shape of the resonance changes as well as the total intensity. For the sphere we see a peak in Q_{ext} at around 410 nm due to the dipole resonance with a shoulder to the resonance at around 380 nm caused by a second resonance there (the quadrupole resonance). For the case of the elongated particle, the peak and shoulder have been reversed, the higher intensity comes at the lower wavelength and can be associated with the quadrupole mode, while the shoulder at the higher wavelength comes from the dipole mode. If we move to the near field picture, the same effect is observed. Figure 6.2(a) shows a typical dipole field pattern which has been distorted slightly to the forwards direction due to the presence of the electric quadrupole mode. Part (b) instead shows the elongation along the k direction, the field pattern looks noticeably different with four prominent high field intensity lobes suggesting a mainly quadrupolar type resonance.

We move on to consider the elongation in the direction of the electric polarisation (parallel to E). In fig. 6.1 we observe that the resonance is strongly redshifted, increased in

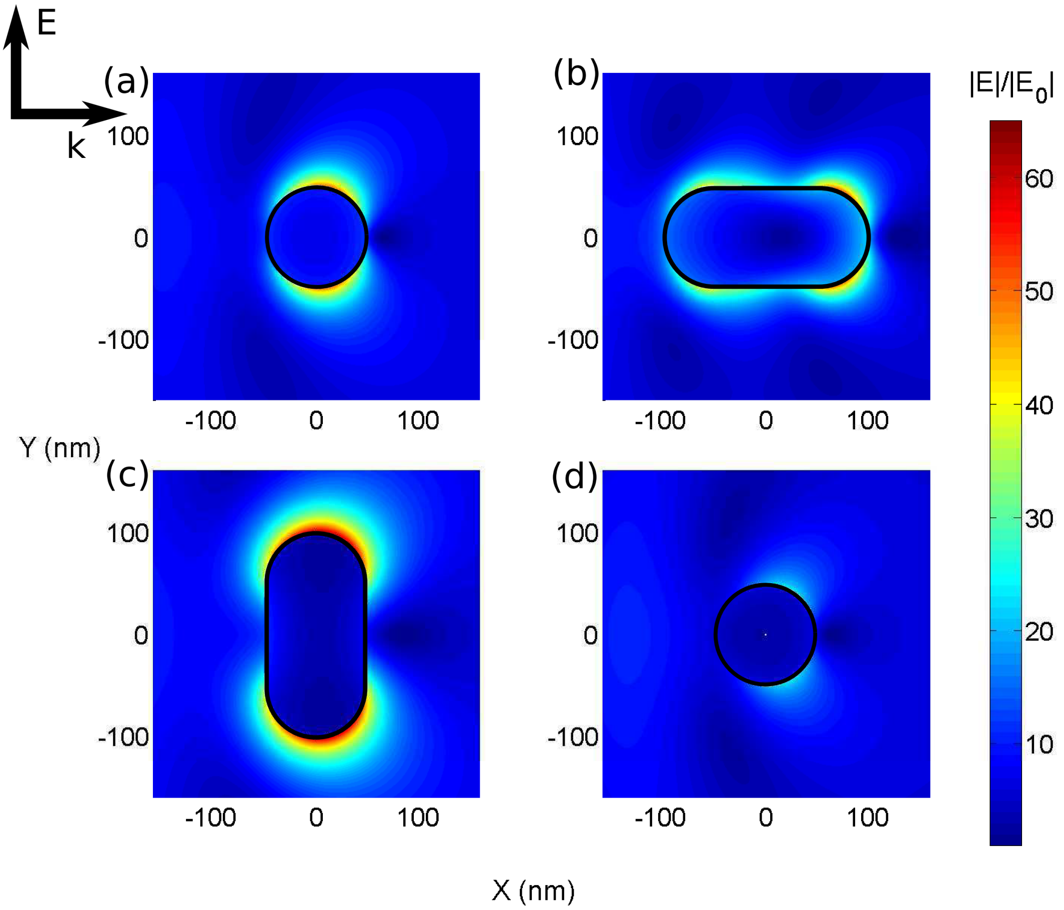

Figure 6.2: The near fields for the particles shown in figure 6.1, in each case the wavelength used is the peak resonance wavelength taken from the extinction cross section.

intensity and the shape changes. These are all due to a retardation effect. Figure 6.3 shows schematically the position of an electron in an incident field in the non-retarded and retarded regime. If there is no retardation, the driving and restoring forces are in phase. The sinusoidal electric field (the driving force) pushes the electron away from the center line, in the case of a nanoparticle, this leads to positive charge build up on the opposite surface which generates a restoring force. This force is maximised when the driving force is also maximised. If the length of the particle is increased in the direction of polarisation, i.e. the direction of the driving force, then the time taken for the restoring force to reach the electron will also be increased. If this time becomes significant, the electrons will feel a restoring force which is much weaker than in the non-retarded case. This leads to a redshift and increase in intensity of the resonance.

Finally, elongation in the direction parallel to the magnetic polarisation (parallel to H) causes the resonance to be reduced in intensity. This is due to dephasing of the resonance, as the particle elongates, the electric field acting on the particle no longer has

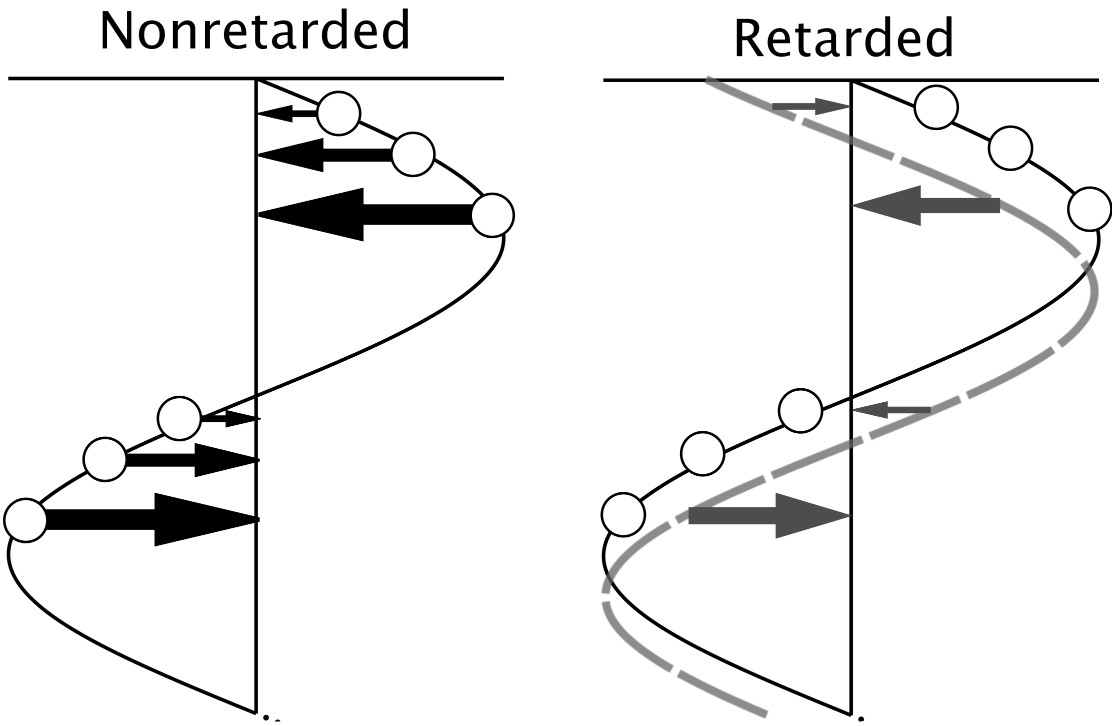

Figure 6.3: Schematic view of the retardation effect which causes the resonance of large particles to redshift.

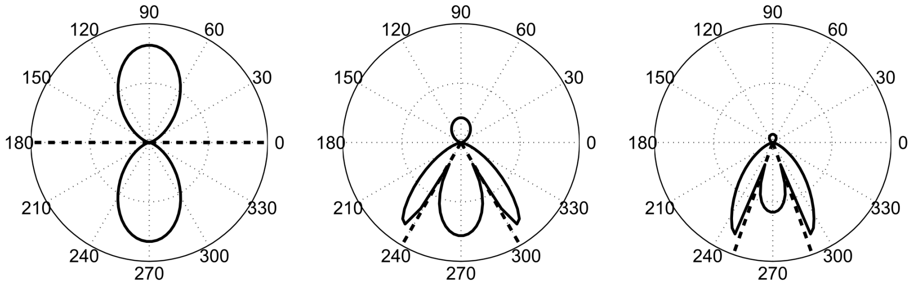

Figure 6.4: The angular scattering distribution for a radius 50 nm Ag hemisphere at an air/substrate interface. The substrate has in each case a different refractive index, (a) n = 1, (b) n = 2 and (c) n = 3. The substrate is the lower half of the image while the air is the upper half, light is incident from the air side. Dashed lines show the angle for total internal reflection inside the substrate.

a homogeneous phase across the whole particle. This will lead to the driven oscillations to become out of phase with each other, resulting in the reduced resonance intensity.

6.2 Interface Properties

In chapter 3, the resonance of a plasmonic particle was decomposed into different multipoles using Mie theory. In particular, for small metallic particles the electric dipole response tends to dominate. Schmid et al. used the solution for the emission of an electric dipole source near to a planar interface between two materials with different permittivities to predict the enhancement seen by placing small plasmonic nanoparticles in a solar cell device [61]. The solution predicts that more light tends to be directed into the material with a higher permittivity. The physical significance of this is that the emission rate of a dipole source is strongly affected by the density of states in the surrounding medium, therefore a material with a higher permittivity which has an associated higher density of states will receive more emission from the dipole.

Figure 6.4 demonstrates this principle by showing the angular scattering distribution for a hemispherical Ag plasmonic particle at a planar interface between two dielectrics. In all cases the upper dielectric is air, while the lower dielectric will be varied in refractive index from 1 (air) to 3 in order to show the effect of increasing optical density of states in the substrate. In each case the angle of total internal reflection inside the substrate is shown in a dashed line. This line represents the highest angle at which light can propagate inside the substrate if it is incident from the upper half space without the presence of nanoparticles. That means that emission into angles higher than this due to the nanoparticle represents coupling of light into modes trapped within the substrate due to total internal reflection if the interface on the other side of the substrate is also air. If we consider that for a high absorption there will be some kind of reflector on the rear side (typically a metal layer) of the device, it means that light will be trapped within the device, since it cannot escape when returning to the air/dielectric interface after being reflected from the back reflector. For the highest absorption enhancement, we desire for the light to be trapped solely within the absorbing layer rather than inside the multilayer stack. To do this using the concept of plasmonic particles at an interface requires that the nanoparticles be placed at an interface including the absorber layer. However this may come with significant electrical drawbacks, therefore a tradeoff must be found.

The question remains how this generalises to magnetic dipole moments and to higher order electric and magnetic multipole orders. For the case of plasmonic particles magnetic resonances are not excited very efficiently meaning that we can neglect the effect of an interface on those orders. The higher order electric resonances (e.g. quadrupole) can be efficiently excited in larger particles and in a homogeneous medium they typically show forwards scattering behaviour, therefore higher order modes may not be useful for particles that should mainly scatter the light backwards into trapped modes.

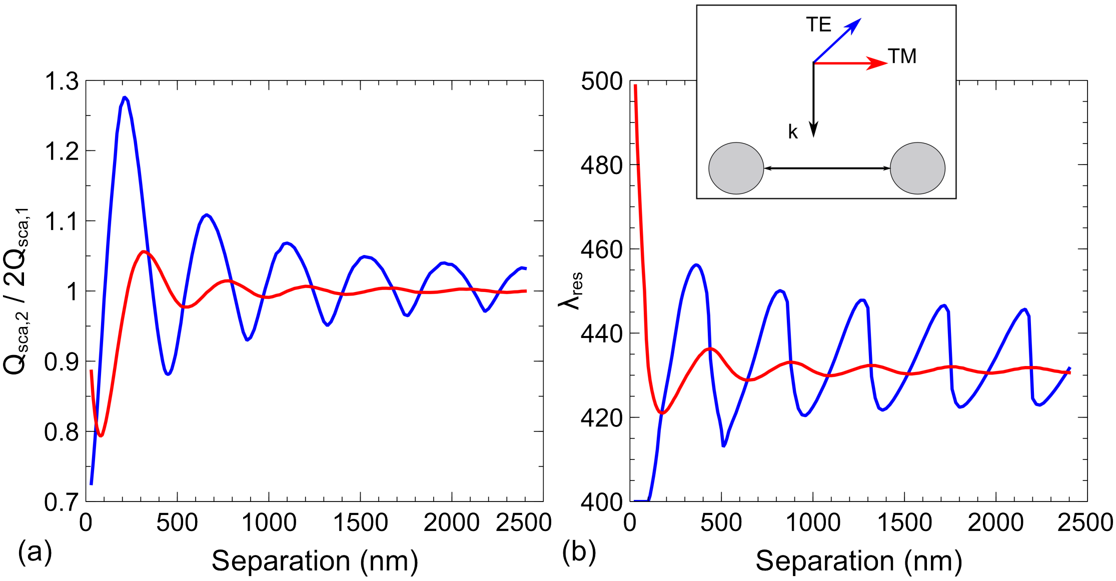

FIGURE 6.5: The peak scattering (a) and peak wavelength (b) for two radius 60 nm Ag spheres in air as a function of the edge to edge separation between the particles. The inset shows the orientations of the TM and TE polarisations as well as the separation between particles.

6.3 Two Particle Interactions

So far we have considered only a single particle, for integration of particles into a device multiple particles will need to be considered. In order to understand what kind of interactions may occur, we first consider the interaction between two spherical particles. Figure 6.5 shows the peak scattering and peak wavelength from two spherical Ag particles as a function of the edge to edge distance between the two particles. The scattering is normalised to twice the scattering from a single particle, therefore in the limit of no interaction this should give a value of unity. Here we will only consider light incident perpendicular to the axis formed by the two particles, since we are interested in how particles interact on a surface when light is incident perpendicular to the surface. In the case of perpendicular incidence, two different polarisations must be considered, light can be polarised with the magnetic field normal to the particle axis which we refer to as transverse magnetic (TM) or it can be polarised with the electric field normal to the particle axis, which we refer to as transverse electric (TE). The two polarisations are depicted in the inset of fig. 6.5.

Both polarisations follow a general trend in that the total scattering and the peak wavelength oscillate with the separation distance due to far field coupling. For short distances ($<$ 200 nm) the oscillations give way to more extreme behaviour, this is due to the near field coupling present when particles are close together. The total scattering is reduced when near field coupling is present. That is because the envelope of light which the particle interacts with, which is larger than the geometrical cross section of the particle, overlaps between particles which are close together. These overlapping envelopes compete for the incident light, meaning that both particles interact with less light than if they were isolated. When the particles are far enough away from each other, the envelopes do not overlap meaning there is no reduction in the amount of light interacted with. The resonance position is also strongly shifted in the near field region. This can be understood by viewing the two particle system as a single composite particle in the near field coupling region. This coupled particle will be elongated along the axis between the two particles. Previously in this chapter, the effects of elongation on particle resonances have been discussed. The elongation present for light incident with a TM polarisation causes a redshift to the resonance, while light incident in the TE polarisation will be blueshifted.

The far field coupling causes separation dependent oscillations on the order of the incident wavelength. This is because the total light incident to each particle includes the incident plane wave plus the scattered field from the other particle. The scattered field changes with phase on the order of a wavelength and interacts coherently with the incident plane wave. This causes either constructive or destructive interference meaning that the total scattering will be greater or lesser than twice the scattering of an isolated particle. This will change the wavelength of the peak scattering, if we imagine that the interference between two particles is maximally constructive for a certain wavelength and separation, then if the separation is increased slightly, a slightly increased wavelength will bring the interference back into maximum coherency. The far field interference is more pronounced for the TE polarisation because the far field radiation from an electric dipole is very low parallel to the dipole axis (actually equal to zero for the limit of being exactly on axis). Therefore when the polarisation is TM the electric dipoles are collinear to each other and interact only weakly, but when the polarisation is TE the dipoles are parallel but not collinear meaning that they interact with each other relatively strongly. For both cases this interaction reduces with further separation since the field produced by the particles becomes weaker with increasing separation (only the value of the field integrated over all angles remains constant).

Based on the coupling of two single particles, we can extract some implications for the case of particle arrays. We will consider ordered and unordered particle arrays. Ordered particle arrays will have a well defined inter-particle edge to edge spacing and polarisation. This means that a specific point on the curves shown in fig. 6.5 will be met, causing red/blueshifting and increase/decrease in scattering strength depending on the exact separation. The scattering will also be highly polarisation dependent as can be seen in the difference between the TE and TM modes shown in the figure. On the other hand, an unordered or random array will have a variable particle separation. If

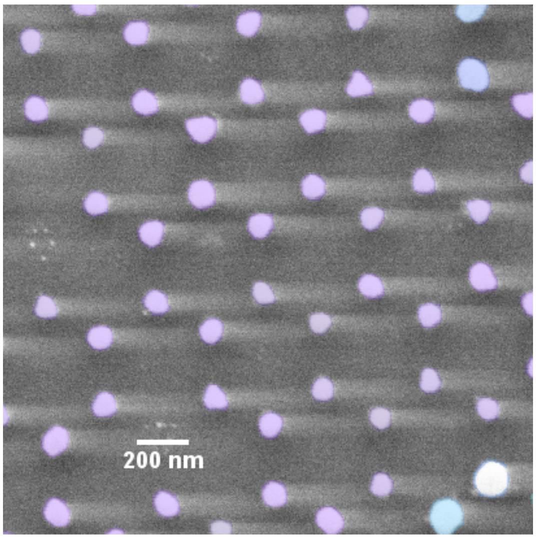

Figure 6.6: SEM image of a periodic nanoparticle array. The particles are coloured after their plasmonic resonance wavelength for the particular particle size in air.

that variation in edge to edge separation is very narrow, we will see a similar result as that for the periodic array. However if the variation in separations is quite large, then many different points along the curves in fig. 6.5 will be sampled. Since the curves are oscillating if at least one whole period of oscillation (with respect to separation) is uniformly sampled, the net effect will be to obtain the average scattering, which is always twice the isolated particle scattering for the given two particle system. This means that a random array with a large variation in inter-particle separations will behave similarly to isolated particles, since the constructive/destructive interference from other particles tends to cancel out. This will be discussed further in the following sections.

6.4 Periodic Arrays of Nanoparticles

There are many methods capable of producing periodic arrays of nanoparticles. For example, e-beam lithography, nanosphere lithography and nanoimprint lithography to name but a few. Periodic arrays are characterised by having uniformly shaped and sized particles with a fixed interparticle spacing. This means that for light incident with a coherence length longer than the interparticle spacing, the particles will react coherently to the light. This may or may not be beneficial to device design.

We choose to study particles fabricated using nanosphere lithography due to the relative ease and low cost in fabrication compared to other techniques. This comes at the cost of not having full control over the size and density of nanoparticles. Figure 6.6 shows a SEM image of the nanoparticles prepared using nanosphere lithography. In order to show

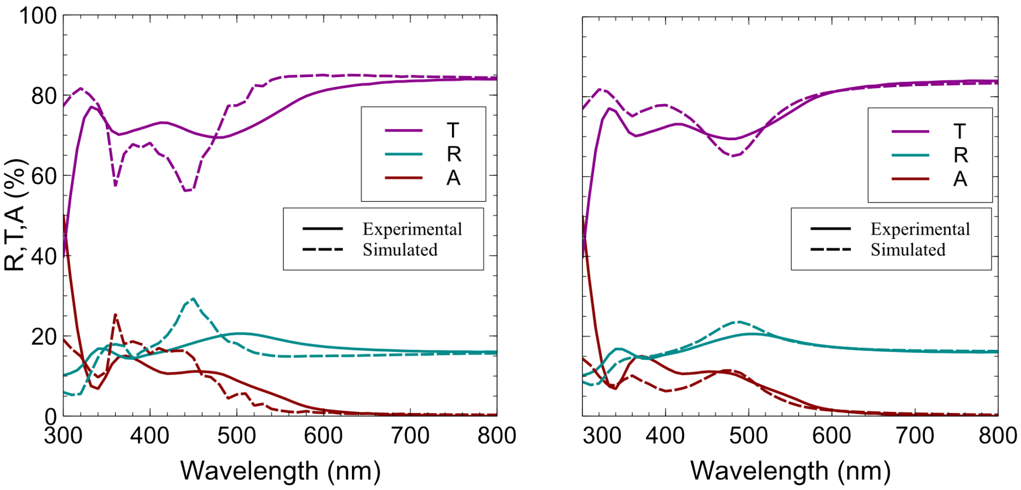

Figure 6.7: The reflection, transmission and absorption for the particle array shown in fig. 6.6. Part (a) compares full 3D simulations with periodic boundary conditions to the experimental values. Part (b) instead compares the method of averaging single particle responses to the experimental data.

the relationship between particle size and spectral resonance position, the particles are coloured by their resonant frequency, calculated via Mie theory for a spherical particle of the same radius shown in the SEM image but in air. The fact that they are all the same colour (apart from some defects) hints at the relatively narrowband response produced by such an array. This is further enhanced by the fact that the particles are small, as we have seen, the dipole resonance broadens significantly when increasing particle size, therefore smaller particles have a narrowband response.

Figure 6.7 shows the reflection, transmission and absorption from the nanoparticle array shown in fig. 6.6. Part (a) compares the experimental data to simulated data using fully 3D periodic boundary FEM simulations. Similarly part (b) compares the experimental data to simulated data using an average of isolated cylindrical boundary condition problems as outlined in chapter 5. The fully 3D periodic boundary conditions should in principle give a very good agreement to the experimental data due to the periodic nature of the array. However, as is visible in fig. 6.6 the sample contains considerable imperfections, such as larger particles and missing particles. We can also infer the presence of sections of solid Ag film on the sample due to the long wavelength reflection being higher than that of glass. No plasmonic activity is expected in this spectral region and the reflection is almost constant with wavelength which can only be described by a solid film. Therefore a 10% Ag film has been included into the simulated data based on empirical matching of the long wavelength spectra. Due to the sample imperfections the resonance is significantly broadened and redshifted in the experimental case compared to the simulations. This is to be expected due to two contributing factors, that is

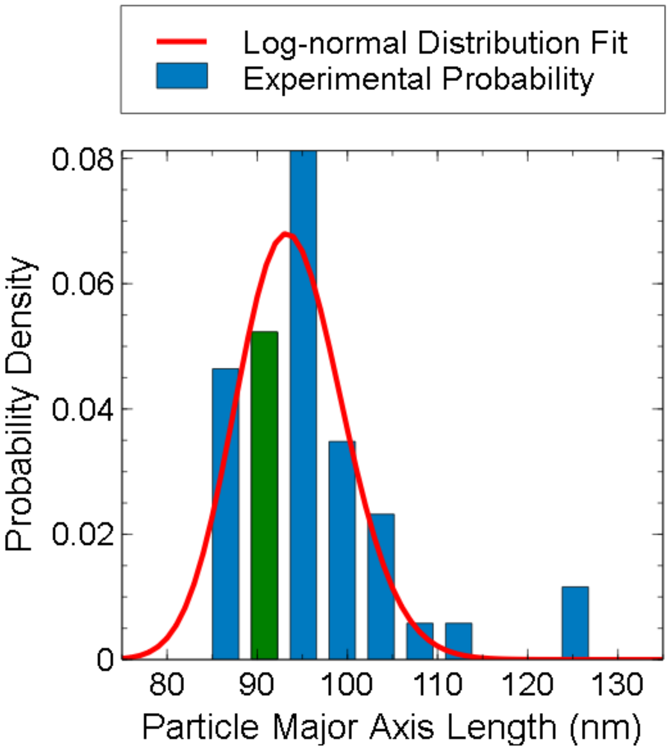

Figure 6.8: The particle size distribution extracted from fig. 6.6 used in the simulations in fig. 6.7(b). The bars represent the measured statistical distribution while the red line is a fit to the data. The green bar represents the size used in the full 3D simulations in 6.7(a).

that larger particles tend to have broader resonances, and the presence of different sizes (and associated resonance wavelengths) will broaden the overall response even if each individual resonance would be narrow.

Since the presence of imperfections is unavoidable, we may instead try to simulate the range of nanoparticle sizes present. Figure 6.8 shows the distribution of particle sizes present taken from the SEM image in fig. 6.6. The bars represent the probability histogram of sizes taken from the image, while the curve shows the fitted log-normal probability density function. The green bar shows the single particle diameter used in the 3D FEM simulation. This distribution takes into account the range of sizes present in the sample but does not include extreme outliers in size. In fig. 6.7 part (b) we see that the resulting transmission, reflection and absorption curves are much broader than the simulation in part (a). The results from the averaging of isolated simulations is in good agreement with the experimental results which supports the validity of this approach.

In chapter 5 we introduced corrections to the averaging isolated simulations due to reflections from the rear side of the substrate. In this case such corrections did not give better agreement with the results. This could be due to bare areas of the sample not

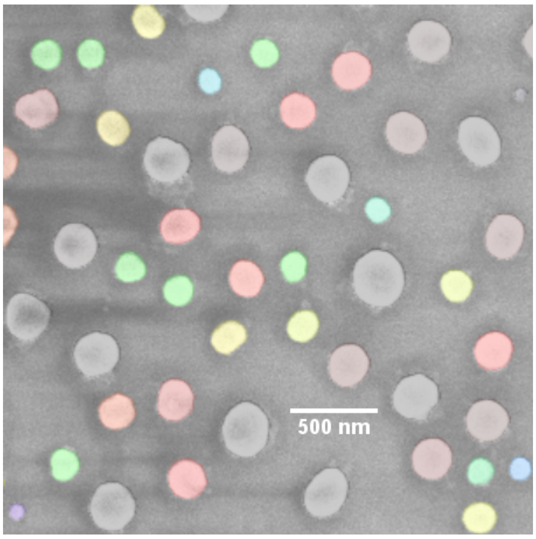

Figure 6.9: SEM image of a random nanoparticle array. The particles are coloured after their plasmonic resonance wavelength for the particular particle size in air.

contributing to the particle scattering, meaning that the overall scattering is reduced. In this case introducing the internal reflection corrections would cause the predicted scattering to be greater than the scattering seen experimentally. This is supported by the fact that the resonance intensity in fig. 6.7 is very weak compared to the one shown in fig. 6.11 (a-c) even though the particle sizes in each case are similar.

6.5 Random Arrays of Nanoparticles

Similarly to periodic arrays, there are also multiple ways to create a disorderd or random array of nanoparticles. Chemical methods which fabricate nanoparticles in solution before finally depositing them onto a substrate typically end with random positioning of the particles. An even simpler method is that of thermal growth used to prepare the particles presented here. In this method a very thin solid film of metal is first evaporated, followed by thermal annealing which melts the film and causes the formation of nanodroplet-like nanoparticles. An example of the kind of particles that can be produced using this method is shown in fig. 6.9. The particles are randomised in their shape, size, orientation and inter-particle spacing. The particles have been coloured by their resonance frequency, calculated via Mie theory for a spherical particle of the same radius shown in the SEM image but in air, particles that are left grey represent resonance frequencies outside of the visible spectrum (IR for large particles). The variety of different colours suggests the broadband response of the array. The resonance will be further broadened due to the fact that the resonance of each individual particle will be broad due to the large size of the particles.

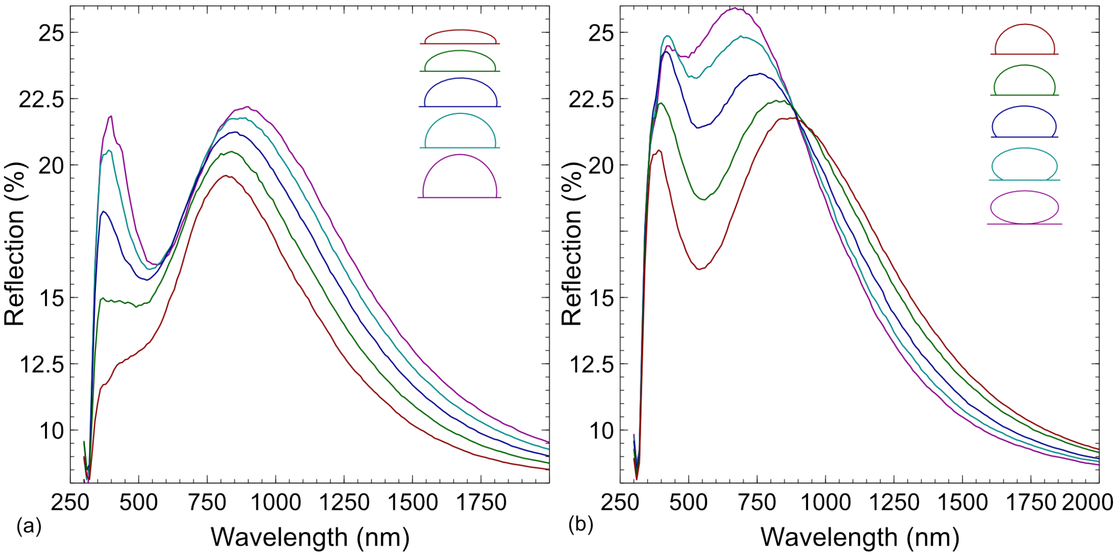

FIGURE 6.10: The effect on the reflection of an isolated Ag particle of two shape parameters. Part (a) shows the variation in particle height with constant contact angle, while part (b) shows a constant height and varying contact angle. The various combinations of height and contact angle are shown as the particle schematics in the graphic.

The particles are more irregularly shaped than for the case of the periodic particles. Although in general the particles seem circular from above, meaning equal a and b axis lengths, the c axis length is relatively unknown. To completely describe the particles on the substrate requires two parameters additional to the a and b axis lengths. In this case we chose the ratio of the height compared to the diameter in the x-y plane, and the contact angle to the substrate. These parameters were chosen since they are the most realistically obtainable from the point of view of characterising the particles experimentally.

Figure 6.10 shows the reflection curves for different particle shapes for the particle size distribution given by the array in fig. 6.9. In part (a) the height ratio (the ratio between the particle's total height and the diameter in the x-y plane) is varied between 0.2 and 0.6 while the contact angle is kept constant at 100°, the legend shows cross sectional images of the particles in the x-z plane. As the particle height increases the reflection curves increase in intensity and redshift, with the quadrupole resonance becoming more prominent. The first two properties can be inferred directly from fig. 6.1, the intensity of the resonance increases since there is more volume of material for scattering but the same area is used when taking into account the coverage. Therefore the volume increases while the coverage remains the same. Secondly due to the elongated shape, the quadrupolar mode is able to be excited. The dipolar mode will be more heavily confined to the interface for the larger particles and will thus be redshifted due to a stronger interaction with the higher index substrate.

Initially it could be assumed that since increasing the contact angle causes the particle to have a higher radius of curvature in the x direction that this would cause the resonance to redshift. However this effect is dominated by the fact that increasing the contact angle decreases the effect of the substrate on the particle. In the limit as the contact angle tends to 180° i.e. a point contact, the particle will behave similarly to being in air. Therefore increasing the contact angle causes the resonance to blue shift. The intensity of the resonance will also increase since the dipolar mode will move away from the interface with increasing contact angle, due to destructive interference of the incident and reflection beams from the glass, it is usually beneficial to have the dipole be further away from the surface [62].

With these basic results in mind we move to comparing the simulations obtained from averaging isolated simulations to experimental results. We present the results for two different samples with different nanoparticle size distributions in fig. 6.11. Parts (a) and (d) show the size distribution (bars) of the samples with their corresponding fitted probability density functions (red line). In both cases a log-normal distribution is in good agreement with the experimental distribution. These distributions were then used to calculate the reflection, transmission and absorption curves shown in (b-c) and (e-f) using the method detailed in chapter 5. The figures in (b) and (e) use the method of averaging isolated simulations without taking into account light trapping in the substrate. These each assume a different shape for the particles, with the shape (i.e. height/diameter ratio and contact angle) were chosen by fitting the resonance to the experimental data.

The results in fig. 6.10 showed that the resonance could be redshifted or blueshifted depending on the particular shape chosen. However resonance position is still predominantly determined by the size distribution chosen, rather than the particular shape at a given size distribution. Due to this, although the shape has been chosen to give the best possible fit to the experimental data, the approach of using the statistical size distribution is still somewhat verified since a different size distribution would not be able to fit the data for any given particle shape.

Despite the fact that the broadness and peak position of the resonance fit for the particle shape chosen, the total intensity of the curves is not in good agreement with the experimental data. Generally the simulated resonances are not as intense as the experimentally measured ones. This can be explained by the fact that the isolated simulations assume a semi-infinite glass substrate, meaning that all light which is transmitted to the substrate enters the results as 'transmitted'. For light which is transmitted at an angle close to normal incidence this is a good approximation since there will be little reflection at the glass rear side. However for higher angles the internal reflection will increase. Previously in this chapter we showed that a high proportion of the light which

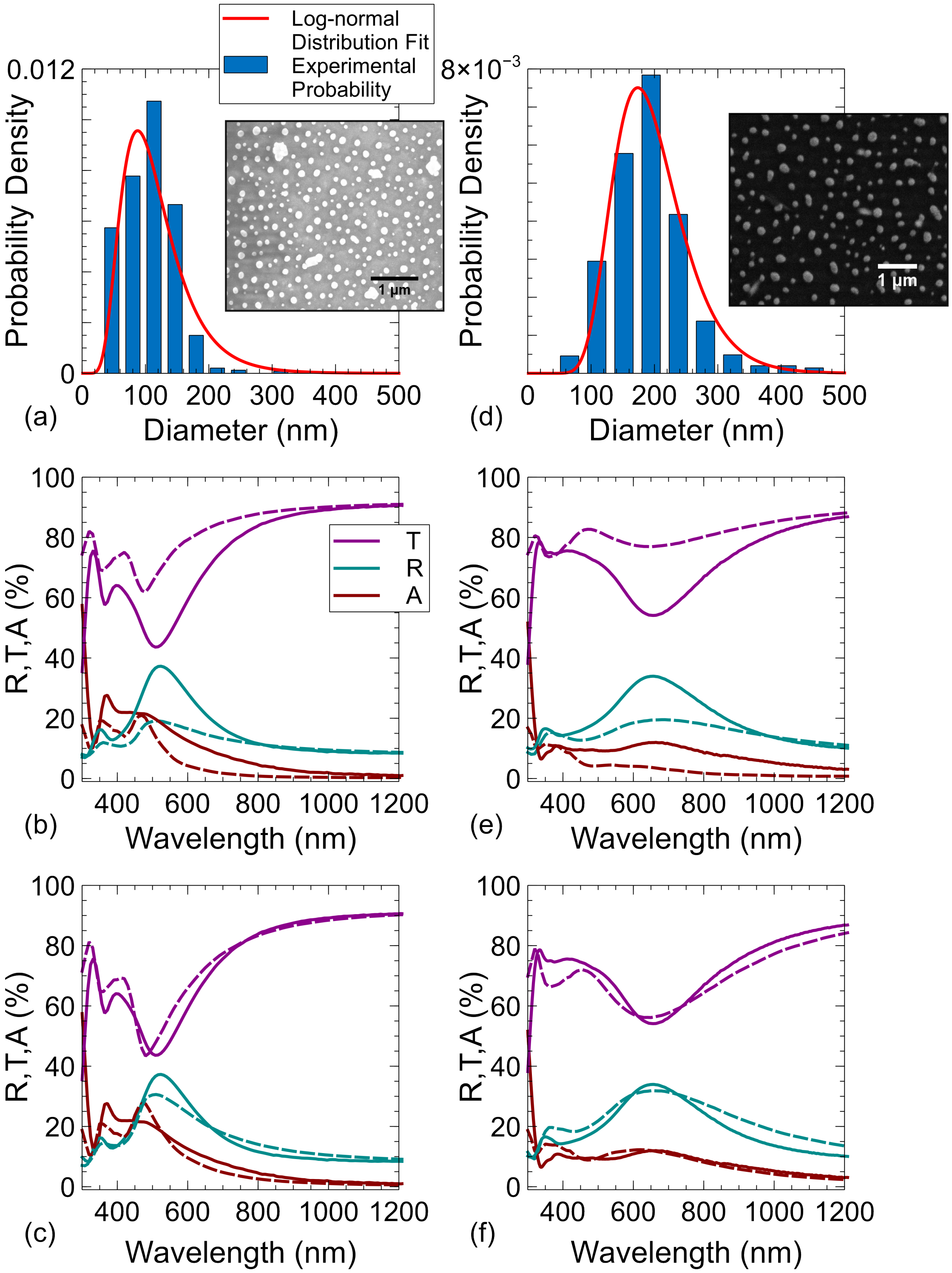

FIGURE 6.11: statistical distribution and reflection, transmission and absorption for two different random nanoparticle arrays. The first array covers (a-c) while the second array covers (d-f). The first row shows the measured size distribution and fitted statistical distribution as well as a SEM image of the array as an inset. The second row compares a simulation using averaging of isolated simulations to the experimental data. The bottom row additionally takes into account total internal reflection inside the glass substrate.

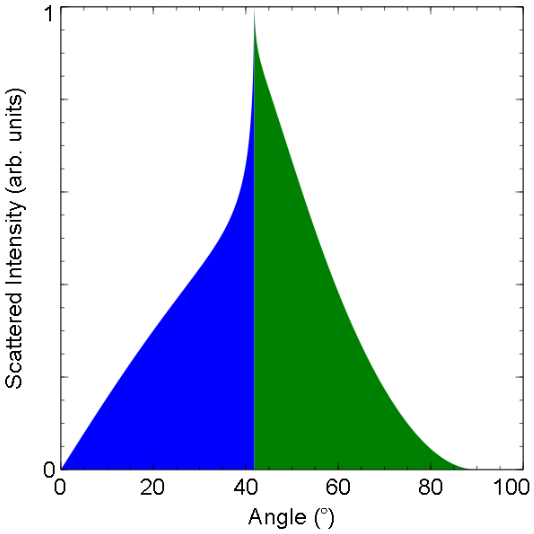

Figure 6.12: The angular distribution of the light transmitted from a spherical particle with radius 100 nm at an air/glass interface at a wavelength of 600 nm. The blue area represented light that will be transmitted out of the substrate, while the green area represents light trapped in the substrate.

is transmitted into a substrate will be at high angles, even at angles higher than the angle of total internal reflection. Correcting for the total internal reflection as outlined in chapter 5 gives the simulated curves in parts (c) and (f) which show good agreement with the experimental data. In calculating these curves we assume that 50% of the transmitted light is trapped within the substrate and that 60% of this light is converted to reflection and 40% is converted to absorption in the particle. The 50% trapping assumption can be inferred from fig. 6.12, in which we plot the angular distribution of the transmitted light for a radius 100 nm Ag particle at an air/glass interface. In this case 0° corresponds to directly transmitted light, while 90 ° would be light scattered perpendicular to the incident beam. The values contain a $\sin\theta$ factor to account for the fact that the values are azimuthally integrated. The two areas are roughly equivalent with slightly more light being trapped than transmitted. This leads to the assumption that 50% of the incident light is trapped within the substrate. The amount of trapped light that is converted to reflection and transmission is not so easy to predict. However since the scattering cross section is larger than the absorption cross section for such particles, it is reasonable to assume that more light is scattered than absorbed.

Generally the amount of trapped light and the fraction of trapped light that goes to reflection and absorption will be a function of the wavelength. However even assuming that these are constant with wavelength as we have done here leads to results which match the experimental data well. The problem is that this precludes having accurate simulations of the particles based purely on the SEM image data, since the amount of light trapped inside the substrate is difficult to simulate using isolated simulations.

This chapter has shown that simulating arrays of particles can be very complicated, especially for the case of random particles. Although the method of averaging managed to predict the correct resonance wavelength, it was not shown to be quantitatively predictive due to significant internal reflection inside the substrate. This, however, is itself promising from the point of view of light trapping applications in solar cells. The method of statistical averaging can therefore be used to rapidly optimise the optical resonance position based on the nanoparticle distribution, which can then be used as a starting point for rigorous simulations including all particle interactions.

Chapter 7

Scattering Matrix Method

Light propagation through a layered stack such as the one presented in fig. 7.1 can be solved analytically. This is because we can orientate our axis to simplify the system, if we assume that the layer boundaries all lie in the x-y plane with the material transitions occurring in the z direction To do this we assume that the layers are infinitely extended in the x-y plane due to the fact a solar cell will have dimensions orders of magnitude larger than the wavelength in the x and y directions. This means that components of light propagating in the x or y directions do so in a homogeneous medium with associated plane wave solutions. Therefore we only need to calculate how the components propagating in the z direction are affected by the layered stack. The boundary conditions for electric and magnetic fields at an interface can be used to determine the amplitudes of

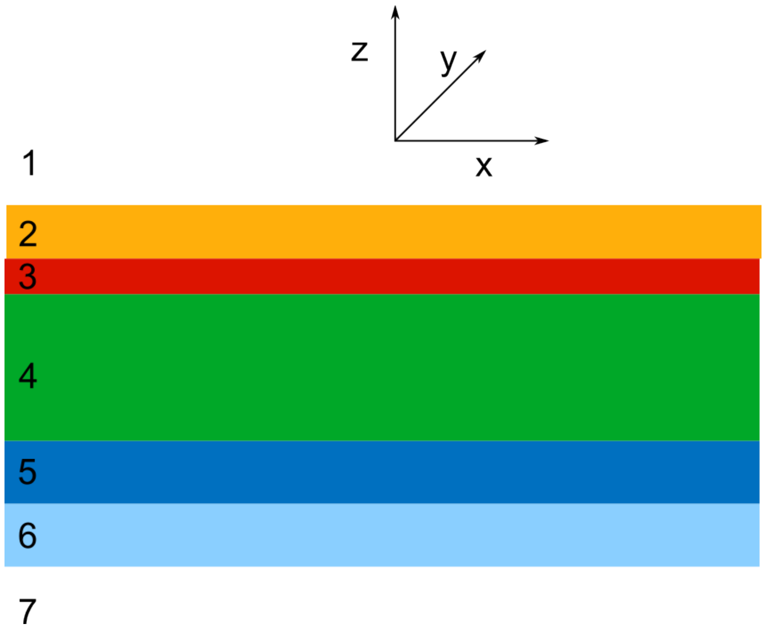

Figure 7.1: A schematic example of a layered stack system. The layers are infinitely extended in the x-y plane.

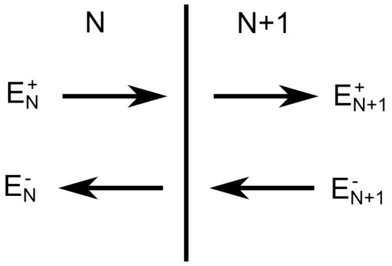

FIGURE 7.2: The incoming and outgoing fields at the interface between the N^{th} material and the $N+1^{th}$ material.

fields on either side of an interface. If the amplitudes of fields incident from above, below or both are known, the fields interior to the layered stack can be calculated by repeated application of the boundary conditions and propagation in a homogeneous medium.

7.1 Comparison to Transfer Matrix

The formalism used to calculate field amplitudes interior and exterior to the layered stack is called the transfer matrix or scattering matrix depending on how field amplitudes on either side of an interface are related. The transfer matrix (T matrix) takes field values of forward and backwards traveling waves on one side of an interface and gives the field values on the other side of the interface. The scattering matrix (S matrix) formalism takes the incoming waves on both sides of the interface and gives the outgoing waves on each side of the interface. Figure 7.2 shows the field values on either side of an interface inside of a layered stack. The T matrix links the field values as following

$$\begin{bmatrix} E_N^+ \\ E_N^- \end{bmatrix} = \begin{bmatrix} T_{11} & T_{12} \\ T_{21} & T_{22} \end{bmatrix} \begin{bmatrix} E_{N+1}^+ \\ E_{N+1}^- \end{bmatrix}. \tag{7.1}$$

Whereas the S matrix links the values as following

$$\begin{bmatrix} E_N^- \\ E_{N+1}^+ \end{bmatrix} = \begin{bmatrix} S_{11} & S_{12} \\ S_{21} & S_{22} \end{bmatrix} \begin{bmatrix} E_N^+ \\ E_{N+1}^- \end{bmatrix}. \tag{7.2}$$

The T matrix formulation can be unstable for absorbing media. Although the interface condition shown here remains perfectly fine, the problem arises when calculating the propagation through an absorbing layer. Consider propagation through the N^{th} layer which will be absorbing. We begin with field values of the forwards and backwards propagating waves inside of layer N at the interface to the $N-1$ layer, we then wish to apply a propagation matrix to obtain the field values inside the N^{th} layer at the interface to the $N+1$ layer. This propagation matrix will multiply the forwards traveling wave by a factor $exp(i(n+ik)2\pi t/\lambda) = exp(-k2\pi t/\lambda)exp(in2\pi t/\lambda)$, where $n+ik$ is the complex refractive index of layer N, t is the thickness of layer N and λ is the vacuum wavelength. As the value of the absorption in layer N given by the k value increases, this propagation term will tend towards zero due to presence of the negative exponential term. We now consider the propagation of the backwards traveling wave. This will be multiplied by a factor $exp(-i(n+ik)2\pi t/\lambda) = exp(k2\pi t/\lambda)exp(-in2\pi t/\lambda)$. For increasing k value this will increase exponentially which causes a major instability in the algorithm. The S matrix formalism avoids this error since incoming waves are always directly related to outgoing waves, this ensures that we always use the propagation factor $exp(i(n+ik)2\pi t/\lambda)$ thereby avoiding exponentially increasing numbers. For this reason we employ the S matrix formalism in this work.

7.2 Scattering Matrix Formalism

We present here a short overview of the S matrix formalism as it is presented in [63]. We begin by considering Maxwell's equations for the E and H fields in linear homogeneous isotropic media

$$\nabla \times \mathbf{E} = k_0 \mu_r \tilde{\mathbf{H}}, \tag{7.3}$$

$$\nabla \times \tilde{\mathbf{H}} = k_0 \epsilon_r \mathbf{E}, \tag{7.4}$$

where k_0 is the magnitude of the wave-vector in free space and μ_r and ϵ_r are the relative permeability and permittivity of the medium, respectively. We have replaced the magnetic field $\mathbf{H}$ by the normalised magnetic field $\tilde{\mathbf{H}} = i\mathbf{H}/(\epsilon_0 c)$ where i is the imaginary unit, ϵ_0 is the permittivity of free space and c is the speed of light in vacuo. This keeps the values of $\tilde{\mathbf{H}}$ and $\mathbf{E}$ at the same order of magnitude increasing numerical stability.

As previously mentioned, the x and y components are assume to have a plane wave form due to homogeneity in these directions. That means that partial differentials in these dimensions can be replaced

$$\frac{\partial}{\partial x} = ik_x, \tag{7.5}$$

$$\frac{\partial}{\partial y} = ik_y. \tag{7.6}$$

Inserting these into 7.3 and 7.4 gives six coupled equations

$$ik_yE_z - \frac{dE_y}{dz} = k_0\mu_r\tilde{H}_x, \tag{7.7}$$

$$\frac{dE_x}{dz} - ik_xE_z = k_0\mu_r\tilde{H}_y, \tag{7.8}$$

$$ik_xE_y - ik_yE_x = k_0\mu_r\tilde{H}_z, \tag{7.9}$$

$$ik_y\tilde{H}_z - \frac{d\tilde{H}_y}{dz} = k_0\epsilon_rE_x, \tag{7.10}$$

$$\frac{d\tilde{H}_x}{dz} - ik_x\tilde{H}_z = k_0\epsilon_rE_y, \tag{7.11}$$

$$ik_x\tilde{H}_y - ik_y\tilde{H}_x = k_0\epsilon_rE_z. \tag{7.12}$$

We can eliminate the z components of the fields via substitution

$$\frac{dE_x}{dz} = \frac{k_xk_y}{\epsilon_r}\tilde{H}_x + \left(\mu_r - \frac{k_x^2}{\epsilon_r}\right)\tilde{H}_y, \tag{7.13}$$

$$\frac{dE_y}{dz} = \left(\frac{k_y^2}{\epsilon_r} - \mu_r\right)\tilde{H}_x - \frac{k_xk_y}{\epsilon_r}\tilde{H}_y, \tag{7.14}$$

$$\frac{d\tilde{H}_x}{dz} = \frac{k_xk_y}{\mu_r}E_x + \left(\epsilon_r - \frac{k_x^2}{\mu_r}\right)E_y, \tag{7.15}$$

$$\frac{d\tilde{H}_y}{dz} = \left(\frac{k_y^2}{\mu_r} - \epsilon_r\right)E_x - \frac{k_xk_y}{\mu_r}E_y. \tag{7.16}$$

Note that we have normalised the lengths scales such that $k_i/k_0 \to k_i, i = x, y, z$ and $k_0z \to z$. These four equations can be written more compactly as two matrix equations

$$\frac{d}{dz}\begin{bmatrix} E_x \\ E_y \end{bmatrix} = \frac{1}{\epsilon_r}\begin{bmatrix} k_xk_y & \mu_r\epsilon_r - k_x^2 \\ k_y^2 - \mu_r\epsilon_r & -k_xk_y \end{bmatrix}\begin{bmatrix} \tilde{H}_x \\ \tilde{H}_y \end{bmatrix}, \tag{7.17}$$

$$\frac{d}{dz}\begin{bmatrix} \tilde{H}_x \\ \tilde{H}_y \end{bmatrix} = \frac{1}{\mu_r}\begin{bmatrix} k_xk_y & \mu_r\epsilon_r - k_x^2 \\ k_y^2 - \mu_r\epsilon_r & -k_xk_y \end{bmatrix}\begin{bmatrix} E_x \\ E_y \end{bmatrix}. \tag{7.18}$$

Since these 2x2 matrices will be used often, we given them the labels $\hat{P}$ and $\hat{Q}$

$$\frac{d}{dz}\begin{bmatrix} E_x \\ E_y \end{bmatrix} = \hat{P}\begin{bmatrix} \tilde{H}_x \\ \tilde{H}_y \end{bmatrix}, \tag{7.19}$$

$$\frac{d}{dz}\begin{bmatrix} \tilde{H}_x \\ \tilde{H}_y \end{bmatrix} = \hat{Q}\begin{bmatrix} E_x \\ E_y \end{bmatrix}. \tag{7.20}$$

Finally we differentiate equation 7.17 and substitute 7.18 into it to obtain a single second order differential matrix equation

$$\frac{d^2}{dz^2}\begin{bmatrix} E_x \\ E_y \end{bmatrix} = \hat{P}\hat{Q}\begin{bmatrix} E_x \\ E_y \end{bmatrix}, \tag{7.21}$$

$$\frac{d^2}{dz^2}\begin{bmatrix} E_x \\ E_y \end{bmatrix} - \hat{\Omega}^2\begin{bmatrix} E_x \\ E_y \end{bmatrix} = \begin{bmatrix} 0 \\ 0 \end{bmatrix}, \tag{7.22}$$

$$\hat{\Omega}^2 = \hat{P}\hat{Q}. \tag{7.23}$$

This is the system of equations that needs to be solved. We require the eigenvector matrix $\hat{W}$ and the eigenvalue matrix $\hat{\lambda}^2$ of the matrix $\hat{\Omega}^2$. For the case of a simple layered stack these are analytically available. For more complex geometries where layers are not homogeneous in the x-y plane, these eigenvectors and eigenvalues must be computed numerically leading to the method known as rigorous coupled wave analysis (RCWA).

Since $\hat{W}$ and λ^2 are known, we may immediately write the solution for both the E and $\tilde{H}$ fields

$$\begin{bmatrix} E_x \\ E_y \\ \tilde{H}_x \\ \tilde{H}_y \end{bmatrix} = \begin{bmatrix} \hat{W} & \hat{W} \\ \hat{V} & \hat{V} \end{bmatrix}, \begin{bmatrix} e^{-\hat{\lambda}z} & \hat{0} \\ \hat{0} & e^{\hat{\lambda}z} \end{bmatrix}\begin{bmatrix} \mathbf{c}^+ \\ \mathbf{c}^- \end{bmatrix}, \tag{7.24}$$

$$\hat{V} = \hat{Q}\hat{W}\hat{\lambda}^{-1}. \tag{7.25}$$

We have already stated that $\hat{W}$ is the eigenvector matrix for the electric field, we have now introduced $\hat{V}$ as the eigenvector matrix for the magnetic field. The matrix exponentials describe the propagation of a forwards and backwards propagating wave. The column vectors $\mathbf{c}^+$ and $\mathbf{c}^-$ are the amplitudes of forwards and backwards propagating eigenvectors, that is they must be multiplied by the eigenvector matrices to obtain the physical fields.

Given that the eigenvectors and eigenvalues can easily be calculated for each layer, the remaining problem is to determine the amplitude coefficients ($\mathbf{c}^+$ and $\mathbf{c}^-$) within the individual layers of the stack. In order to do this we employ scattering matrices. Previously we characterised scattering matrices as a way to formalise the boundary conditions for fields at a single interface between two materials. However scattering matrices can also be formulated to describe not interfaces (inherently a property of two materials) but individual layers (a property of a single material). The advantage being that if certain materials are used multiple times in the layer stack, the same scattering matrix may be used each time, independently of the surrounding materials. A further advantage is that each individual 4x4 scattering matrix will be symmetric, meaning that only eight from sixteen components need to be calculated. Typically a scattering matrix for a single layer will involve the surrounding layers, meaning it is a property of three different materials. This can be circumvented by the use of infinitesimal layers (thickness = 0) of some other medium that we place in between all physical layers. As long as this material has zero thickness and has a refractive index $n \neq 0$, this will have no physical effect on the computation.

In order to convince the reader of the validity of this approach, we will shortly digress to prove this using the Fresnel coefficients. We will consider the reflection Fresnel coefficient at normal incidence, however the following analysis is equally valid for the transmission coefficient or for angular incidence. We consider the reflection from a two layer system in which the layers are labeled 1 and 3. We will then compare this to a three layer system with labels 1, 2 and 3, where layer 2 will have zero thickness. The layers 1, 2 and 3 are all considered to have different material refractive indices n_1, n_2 and n_3.

The reflection Fresnel coefficient for a two layer system is

$$r_{13} = \frac{n_1 - n_3}{n_1 + n_3}, \tag{7.26}$$

while the reflection coefficient for a three layer system is given by

$$r_{123} = \frac{r_{12} + r_{23} e^{-2i\delta}}{1 + r_{12} r_{23} e^{-2i\delta}}, \tag{7.27}$$

where δ is the phase shift given by a single pass through layer 2. In the case that $t_2 = 0$, this implies $\delta = 0$. In that case the reflection coefficient simplifies to

$$\begin{align} r_{123} &= \frac{r_{12} + r_{23}}{1 + r_{12} r_{23}}, \tag{7.28} \\ &= \frac{\frac{(n_1-n_2)(n_2+n_3)}{(n_1+n_2)(n_2+n_3)} + \frac{(n_2-n_3)(n_1+n_2)}{(n_1+n_2)(n_2+n_3)}}{\frac{(n_1+n_2)(n_2+n_3)}{(n_1+n_2)(n_2+n_3)} + \frac{(n_1-n_2)(n_2-n_3)}{(n_1+n_2)(n_2+n_3)}}, \tag{7.29} \\ &= \frac{(n_1 - n_2)(n_2 + n_3) + (n_2 - n_3)(n_1 + n_2)}{(n_1 + n_2)(n_2 + n_3) + (n_1 - n_2)(n_2 - n_3)}, \tag{7.30} \\ &= \frac{n_1 n_2 + n_1 n_3 - n_2^2 - n_2 n_3 + n_2 n_1 + n_2^2 - n_3 n_2 - n_3 n_1}{n_1 n_2 + n_1 n_3 n_2^2 + n_2 n_3 + n_1 n_2 - n_1 n_3 - n_2^2 + n_2 n_3}, \tag{7.31} \\ &= \frac{2n_1 n_2 - 2n_2 n_3}{2n_1 n_2 + 2n_2 n_3}, \tag{7.32} \\ &= \frac{n_1 - n_3}{n_1 + n_3}, \tag{7.33} \\ &= r_{13}. \tag{7.34} \end{align}$$

Having justified the validity of the approach we will describe how to generate the scattering matrices for single layers.

The scattering matrix will always describe one finite layer surrounded by two infinite layers. In the following the infinite layer will be labeled with 1 and 3 while the finite layer is labeled with 2. Therefore the 4x4 scattering matrix for layer 2 will have the following general form

$$\begin{bmatrix} \mathbf{c}_1^+ \\ \mathbf{c}_1^- \end{bmatrix} = \begin{bmatrix} \hat{S}_{11}^2 & \hat{S}_{12}^2 \\ \hat{S}_{21}^2 & \hat{S}_{22}^2 \end{bmatrix} \begin{bmatrix} \mathbf{c}_3^+ \\ \mathbf{c}_3^- \end{bmatrix}. \tag{7.35}$$

Therefore we need to determine the values of $\hat{S}_{11}^2$,$\hat{S}_{12}^2$,$\hat{S}_{21}^2$ and $\hat{S}_{22}^2$ We begin with the case where the infinite layers do not have the same refractive index and then simplify to the case of symmetric refractive indices used for the S matrix of a single layer.

The boundary conditions for the eigenvector coefficients at the first and second interface of layer 2 are

$$\begin{bmatrix} \hat{W}_1 & \hat{W}_1 \\ \hat{V}_1 & -\hat{V}_1 \end{bmatrix} \begin{bmatrix} \mathbf{c}_1^+ \\ \mathbf{c}_1^- \end{bmatrix} = \begin{bmatrix} \hat{W}_2 & \hat{W}_2 \\ \hat{V}_2 & -\hat{V}_2 \end{bmatrix} \begin{bmatrix} \mathbf{c}_2^+ \\ \mathbf{c}_2^- \end{bmatrix}, \tag{7.36}$$

$$\begin{bmatrix} \hat{W}_2 & \hat{W}_2 \\ \hat{V}_2 & -\hat{V}_2 \end{bmatrix} \begin{bmatrix} e^{-\hat{\lambda}_2 t_2} & \hat{0} \\ \hat{0} & e^{\hat{\lambda}_2 t_2} \end{bmatrix} \begin{bmatrix} \mathbf{c}_2^+ \\ \mathbf{c}_2^- \end{bmatrix} = \begin{bmatrix} \hat{W}_3 & \hat{W}_3 \\ \hat{V}_3 & -\hat{V}_3 \end{bmatrix} \begin{bmatrix} \mathbf{c}_3^+ \\ \mathbf{c}_3^- \end{bmatrix}. \tag{7.37}$$

Where t_i is the normalised thickness of layer i. We then use 7.36 and 7.37 to eliminate the coefficients $\mathbf{c}_2^+$ and $\mathbf{c}_2^-$, and rearrange to give the same form as 7.35. Resulting in the following forms for the scattering coefficients

$$\hat{S}_{11}^2 = (\hat{A}_{21} - \hat{X}_2 \hat{B}_{23} \hat{A}_{23}^{-1} \hat{X}_2 \hat{B}_{21})^{-1} (\hat{X}_2 \hat{B}_{23} \hat{A}_{23}^{-1} \hat{X}_2 \hat{A}_{21} - \hat{B}_{21}), \tag{7.38}$$

$$\hat{S}_{12}^2 = (\hat{A}_{21} - \hat{X}_2 \hat{B}_{23} \hat{A}_{23}^{-1} \hat{X}_2 \hat{B}_{21})^{-1} \hat{X}_2 (\hat{A}_{23} - \hat{B}_{23} A_{23}^{-1} B_{23}), \tag{7.39}$$

$$\hat{S}_{21}^2 = (\hat{A}_{23} - \hat{X}_2 \hat{B}_{21} \hat{A}_{21}^{-1} \hat{X}_2 \hat{B}_{23})^{-1} \hat{X}_2 (\hat{A}_{23} - \hat{B}_{23} A_{23}^{-1} B_{23}), \tag{7.40}$$

$$\hat{S}_{21}^2 = (\hat{A}_{23} - \hat{X}_2 \hat{B}_{21} \hat{A}_{21}^{-1} \hat{X}_2 \hat{B}_{23})^{-1} (\hat{X}_2 \hat{B}_{21} \hat{A}_{21}^{-1} \hat{X}_2 \hat{A}_{23} - \hat{B}_{23}), \tag{7.41}$$

$$\hat{A}_{ij} = \hat{W}_i^{-1} \hat{W}_j + \hat{V}_i^{-1} \hat{V}_j, \tag{7.42}$$

$$\hat{B}_{ij} = \hat{W}_i^{-1} \hat{W}_j - \hat{V}_i^{-1} \hat{V}_j, \tag{7.43}$$

$$\hat{X}_i = e^{-\hat{\lambda}_i t_i}. \tag{7.44}$$

For the case where refractive index of layer 1 and layer 3 are equal, the scattering parameters for layer 2 simplify to

$$\hat{S}^2_{11} = \hat{S}^2_{22} = (\hat{A}_{21} - \hat{X}_2\hat{B}_{21}\hat{A}^{-1}_{21}\hat{X}_2\hat{B}_{21})^{-1}(\hat{X}_2\hat{B}_{21}\hat{A}^{-1}_{21}\hat{X}_2\hat{A}_{21} - \hat{B}_{21}), \tag{7.45}$$

$$\hat{S}^2_{12} = \hat{S}^2_{21} = (\hat{A}_{21} - \hat{X}_2\hat{B}_{21}\hat{A}^{-1}_{21}\hat{X}_2\hat{B}_{21})^{-1}\hat{X}_2(\hat{A}_{21} - \hat{B}_{21}A^{-1}_{21}B_{21}). \tag{7.46}$$

To compute the propagation through the entire layer stack requires the combination of the single layer matrices. To combine scattering matrices together we use the Redheffer star product

$$\begin{bmatrix} \hat{S}^{ij}_{11} & \hat{S}^{ij}_{12} \\ \hat{S}^{ij}_{21} & \hat{S}^{ij}_{22} \end{bmatrix} = \begin{bmatrix} \hat{S}^{i}_{11} & \hat{S}^{i}_{12} \\ \hat{S}^{i}_{21} & \hat{S}^{i}_{22} \end{bmatrix} \otimes \begin{bmatrix} \hat{S}^{j}_{11} & \hat{S}^{j}_{12} \\ \hat{S}^{j}_{21} & \hat{S}^{j}_{22} \end{bmatrix}. \tag{7.47}$$

The individual 2x2 matrices are given by

$$\hat{S}^{ij}_{11} = \hat{S}^{i}_{11} + \hat{S}^{i}_{12}\left[\hat{I} - \hat{S}^{j}_{11}\hat{S}^{i}_{22}\right]^{-1}\hat{S}^{j}_{11}\hat{S}^{i}_{21}, \tag{7.48}$$

$$\hat{S}^{ij}_{12} = \hat{S}^{i}_{12}\left[\hat{I} - \hat{S}^{j}_{11}\hat{S}^{i}_{22}\right]^{-1}\hat{S}^{j}_{12}, \tag{7.49}$$

$$\hat{S}^{ij}_{21} = \hat{S}^{j}_{21}\left[\hat{I} - \hat{S}^{i}_{22}\hat{S}^{j}_{11}\right]^{-1}\hat{S}^{i}_{21}, \tag{7.50}$$

$$\hat{S}^{ij}_{22} = \hat{S}^{j}_{22} + \hat{S}^{j}_{21}\left[\hat{I} - \hat{S}^{i}_{22}\hat{S}^{j}_{11}\right]^{-1}\hat{S}^{i}_{22}\hat{S}^{j}_{12}. \tag{7.51}$$

Now we have a way to combine scattering matrices, and we can calculate the scattering matrix for the case of equal and unequal surrounding media, we can combine the scattering matrices to get the scattering matrix for a complete stack. Figure 7.3 shows schematically how the scattering matrices are combined into the full stack matrix.

This allows the scattering matrix for the entire system to be calculated. The system scattering matrix allows the reflection and transmission of the entire stack to be determined. Since the application to solar cells also required the absorption in each layer to be calculated separately, we introduce our own formalism not covered by [63] in order to determine the absorption in each layer.

The absorption inside of a layer can be calculated by comparing the Poynting vector of both outgoing waves to that of the incoming waves

$$A_i = \left[|\mathbf{S}^{+}_{i+1}| + |\mathbf{S}^{-}_{i-1}| - |\mathbf{S}^{+}_{i-1}| - |\mathbf{S}^{-}_{i+1}|\right]/S_{inc}, \tag{7.52}$$

$$S_i = \sqrt{\frac{\epsilon^i_r k^i_z}{|\mathbf{k^i}|}}|E_i|^2. \tag{7.53}$$

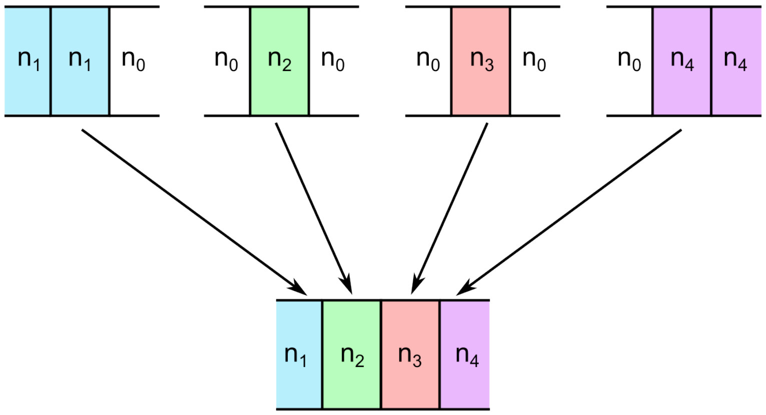

FIGURE 7.3: The combination of scattering matrices of individual layers, and two extra scattering matrices for the reflection and transmission region combine to make the full stack matrix.

Where S_i is the Poynting vector of the i^{th} layer, S_{inc} is the Poynting vector of the incident field, ϵ_r^i is the relative permittivity of the i^{th} layer, k_z^i and $|\mathbf{k^i}|$ are the z component and norm of the k vector in the i^{th} layer, respectively. Therefore only the field values in the zero thickness medium surrounding each material need to be known in order to calculate the absorption. We can calculate these using the field values at either side of the layer stack and one of the following sets of recurrence relations

$$E_j^- = \left[S_{12}^{ij}\right]^{-1}\left[E_i^- - S_{11}^{ij}E_i^+\right], \tag{7.54}$$

$$E_j^+ = S_{21}^{ij}E_i^+ + S_{22}^{ij}E_j^-, \tag{7.55}$$

$$E_j^+ = S_{21}^{ij}\left[S_{21}^{ij}\right]^{-1}\left[E_i^- - S_{12}^{ij}E_i^+\right], \tag{7.56}$$

$$E_j^+ = S_{21}^{ij}E_i^+ + S_{22}^{ij}E_j^-. \tag{7.57}$$

7.3 Incoherent Layer with S Matrix

Two different methods can be used to obtain incoherency in an S matrix or general transfer matrix simulation. The two methods are intensity coupling and phase averaging, we will now discuss them both in turn.

7.3.1 Intensity Coupling

The intensity of light is the square conjugate of the complex electric field

$$I = \mathbf{E}^{\dagger}\mathbf{E}. \tag{7.58}$$

This means that the intensity is a scalar quantity compared to vector electric field. More importantly for the current discussion the intensity is a real number compared to the complex value of the electric field. This means that no phase information is contained in the intensity. Without phase information there cannot be any interference between two overlapping intensity distributions compared to two overlapping field distributions. The implementation of the S matrix algorithm presented here was for the propagation of fields through a layered stack. This could be changed to the propagation of intensities by modifying the boundary conditions and propagation inside of a layer. However we typically wish to include both coherent and incoherent layers inside of a simulation. To achieve this we split the layered stack to be simulated into two different simulations. The simulations contain either all layers above the incoherent layer or all the layers below the incoherent layer. If both simulations take the incoherent layer to be one of the exterior layers of the simulation, and the intensities are calculated in the incoherent layer, then the two can be coupled together incoherently. The topic of coupling two different simulations together will be discussed in more detail in chapter 11. This method is limited in convergence by the tolerance of the iterative coupling.

7.3.2 Phase Averaging

The second method by which an incoherent layer can be simulated is via phase averaging. In this method the simulation is repeated N times, each time using a different phase in the incoherent layer. The final result is then obtained by taking the average of the individual simulations. For example, the reflection would be obtained via

$$< R >= \frac{1}{N}\sum_{n=1}^{N} R_n. \tag{7.59}$$

Where R_n is the reflection calculated for the n^{th} phase. In order to modify the phase in the incoherent layer, the phase can either be directly modified in the S matrix algorithm by adding an extra phase term to the propagation of light through the incoherent layer, or by varying the thickness of the incoherent layer or the incident wavelength of light in a small region which will also change the phase slightly. However those two methods can also have physical consequences if e.g. the incoherent layer is absorbing or the material properties of any of the layers vary with the wavelength. Therefore directly adding a phase factor is preferred where possible. It has been shown that evenly spaced phase factors covering the range from 0 to 2π give the fastest convergence towards an incoherent result [64–66], compared to randomised phase factors. This method is limited in convergence by the total number of phase factors used, this means that for a well converged result a large number of simulations N may be required, which can significantly increase the computational effort required.

Chapter 8

Ultra-Thin Photovoltaics

Until now the results presented have focused on modelling nanoparticles, whether single or multiple, in free space or at an interface. The thesis being presented here is that these particles can beneficially affect ultra-thin film solar cells. In order to evaluate the veracity of this thesis, we now turn to simulations of particles integrated into solar cell devices. In order to better understand how the integration can work, we begin by briefly presenting the basics of solar cells.

8.1 Solar Cell Basics

All solar cells are devices which convert the energy from sunlight into a useable form of energy. Until now the most successful solar cells have been made from inorganic materials and have been based off of the photovoltaic principle. Therefore we will focus exclusively on these types of solar cells, even though technologies like dye sensitised and organic solar cells, and solar fuel cells could potentially also benefit from the work presented in this thesis.

8.1.1 Photovoltaic Effect

The photovoltaic effect is the conversion of photons to voltage. In order to achieve this, a semiconductor is first required that is capable of absorbing optical photons [67]. These photons create electron hole pairs which can be extracted at conducting contacts. In order for this process to create a voltage we need to ensure that the electrons accumulate at one contact while the holes accumulate at a different contact. To do this we add directionality to the device by introducing a pn-junction.

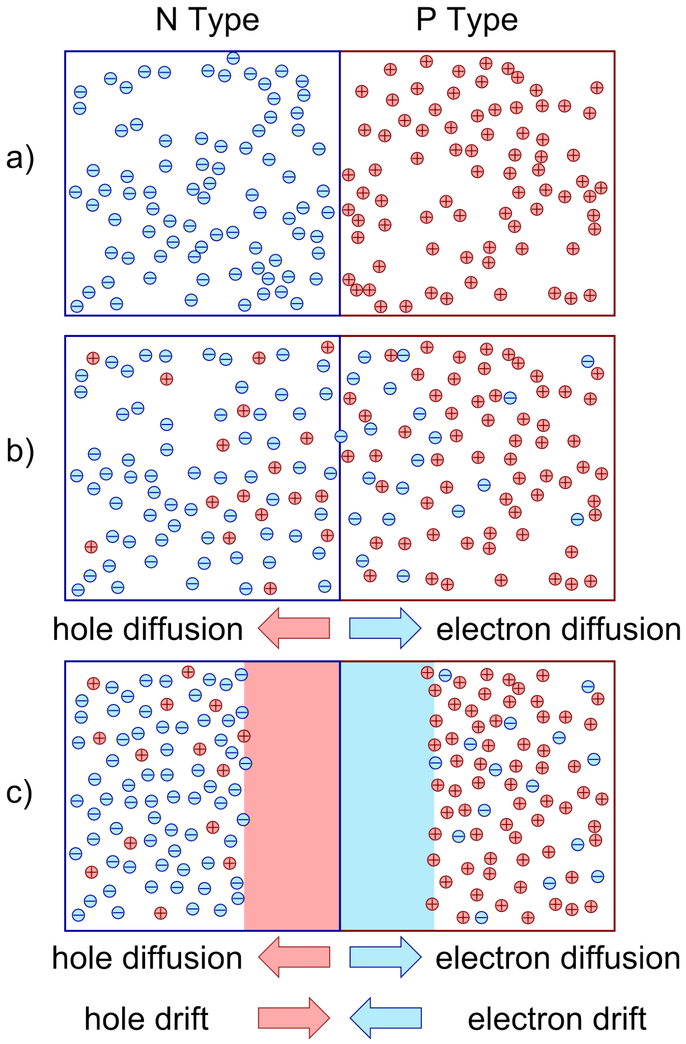

FIGURE 8.1: The formation of a pn-junction. Part a) shows separated p and n type materials. Part b) shows the initial diffusion of majority carriers from both sides to the opposite side. Part c) shows the subsequent formation of a space charge region due to the ionic cores left behind after diffusion, this sets up a drift current which balances out the diffusion current in equilibrium.

A pn-junction is formed from two adjoining semiconductors, one with p type doping (i.e. an excess of holes) the other with n type doping (i.e. an excess of electrons). In this case the excess electrons and holes will naturally diffuse into the semiconductor of the opposite type. When some of the excess charge carriers have diffused out of their respective host semiconductor, they leave behind a region of localised charge with the opposite polarity. For example an n type semiconductor contains dopant atoms with one more electron in their outer shell than the surrounding atoms. The dopant is however, initially still electrically neutral. The extra electron is able to be separated from the dopant atom purely due to thermal effects, allowing the electron to diffuse across the pn-junction to the p type material. This leaves behind the ionised dopant core which will be positively charged. Thus the n type material starts to build up positive charge at the interface while the p type region builds up a region of negative charge at the interface. This charge distribution has an associated electric field causing electrons or holes in the vicinity to drift in opposite directions. The drift effect will counteract the diffusion of excess carriers across the pn-junction. This eventually reaches an equilibrium where the forces of drift and diffusion are equal and opposite. The region of charge build up at the pn-junction is referred to as the space charge region.

Now we add in the generation of electron hole pairs inside of the space charge region due to incident photons, the charge carriers will drift in opposite directions due to the electric field. This ensures that we have directionality in the device meaning that different charge carriers are collected at different contacts. By applying an external load, the current flowing from one contact to the other can be utilised. This is the photovoltaic effect.

8.1.2 Quantum Efficiency

When reducing the thickness of the absorbing layer of a solar cell, the main problem which arises is the incomplete absorption of light. This is particularly a problem for indirect band gap semiconductors like Si, which have a very low absorption coefficient near the band edge, typically necessitating light trapping even for very thick devices. However even for direct band gap materials which will have a comparatively higher absorption coefficient close to the band gap, the absorption may be incomplete for ultra-thin layers, which again necessitates a light trapping concept.

The incomplete absorption is spectrally dependent, however in general long wavelengths will suffer more from incomplete absorption due to the combined effect of longer wavelengths having a shorter path length per unit wavelength in the material, and also due to the fact that for most absorber materials, the absorption coefficient reduces close to their band gap. In order to optimise for the absorption of light in the solar cell, the main goal of our simulations will be to calculate the spectrally resolved absorption in the absorbing layer of the solar cell. This information is not available experimentally, however a close analogue of the absorption can be measured which is the external quantum efficiency. The external quantum efficiency measures how many electron hole pairs were extracted at the contacts for each incident photon. Thus it includes not only the absorption of light leading to electron hole pairs, but also the probability that these electron hole pairs may be separated and collected at the contacts without recombining. In order to compare experimental values of quantum efficiency to our absorption results requires either a coupled optical/electrical simulation which is beyond the scope of the current work, or an assumption of the collection probability of charge carriers. In this work we assume 100% collection of generated charge carriers, simply because any other assumption is very dependent on the individual electrical properties of the cell and would be highly subjective. Since we are presently interested in optimising the optical aspects of the solar cell this will not present any particular problem. However it should be kept in mind that the absorption spectra shown in this work relate to the best possible EQE, and that realistic EQE values would be lower than those predicted by simulation. Although we do not specifically optimise the electrical properties, we also seek to rule out cases that will obviously negatively effect electrical performance. This is discussed in more detail in sec. 10.1 where the concepts for nanoparticle integration are considered.

With regards to photogenerated carriers, a solar cell is typically characterised by the total current produced from the carriers when illuminated by the solar spectrum, as opposed to the individual response at each wavelength. As the total current will also be a function of the area of the solar cell, typically the current density with no external load, called the short circuit current density J_{sc} is used to compare the absorption ability of solar cells. To obtain the value of J_{sc} from the EQE curve, which we assume is equivalent to the absorption curve that we simulate, means multiplying the absorption by the solar spectrum, normalising the energy and integrating over the spectral range

$$J_{sc} = \int_{-\infty}^{\infty} \Phi(\lambda) EQE(\lambda) \frac{q\lambda}{ch} d\lambda. \tag{8.1}$$

Where $\Phi(\lambda)$ is the solar spectrum, q is the fundamental unit of charge, λ is the wavelength, c is the speed of light in vacuo and h is Plank's constant.

8.1.3 Chalcopyrite Solar Cells

Now that the operating principle of photovoltaic solar cells has been described, we will move on to describing in detail the features of a chalcopyrite solar cell. The typical device structure for this kind of solar cell is the following (from front to back) [68],

- Front Contact - ZnO. Typically the front contact contains two separate layers, one is aluminium doped zinc oxide (Al:ZnO) with the other being intrinsic ZnO. This is done in order to optimise both the conductivity and the transmission of light into the layers below. Since the optical properties of Al:ZnO and ZnO differ significantly, we will explicitly state the thickness of each layer contained in the front contact.

- N Doped Layer - CdS. The purpose of this layer is twofold: firstly it provides one half of the pn-junction and secondly it has a good band alignment with the

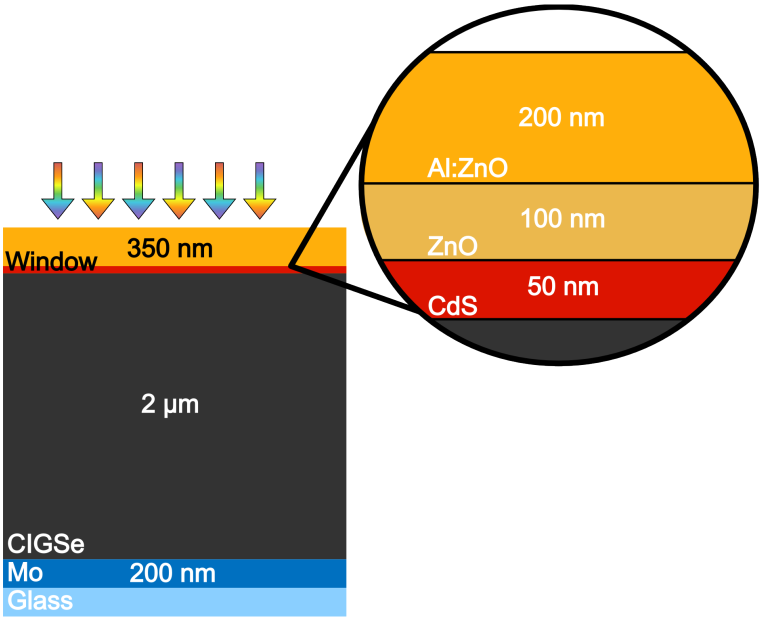

FIGURE 8.2: Schematic diagram of the layers in a standard thin film chalcopyrite solar cell. The window layer contains three individual layers. light is incident from above.

absorbing layer underneath. The band alignment is crucial to avoiding interface recombination at the physical junction between p and n type materials, due to this providing an intermediate between the absorbing layer and the front contact, this layer is often referred to as the buffer layer. In addition this layer should have a band gap higher than the operating wavelengths of the solar cell. This is because we do not want light to be absorbed in this layer. In principle since the space charge region is also present in this layer, electron hole pairs generated here could also contribute to the current. In practice this is undesirable since holes generated in this layer have a high chance to recombine at the CdS/ZnO interface before they drift to the p type layer due to the space charge region.

- P Doped Layer - $\mathrm{Cu(In}_x\mathrm{Ga}_{1-x})\mathrm{Se}_2$ (CIGSe). The eponymous material of the solar cell is the absorbing layer. The purpose of this layer is to absorb as much light as possible. Electron hole pairs generated in this layer can easily be separated by the space charge region. This is because the space charge region extends throughout most of the layer due to a lower doping in this layer compared to CdS. Additionally since the layer is relatively much thicker than the CdS layer, very few electrons will diffuse to the back contact meaning interface recombination there is low.

- Back Contact - Mo. The transition metal molybdenum is used as the back contact material since it provides a good electrical conductivity and also a good electrical contact to the CIGSe layer. This is again a matter of band alignments, Mo happens to form a very thin layer of MoSe_2 at the interface which reduces interface recombination. For the standard solar cell, the fact that Mo has a poor reflectivity is not important due to almost all of the light being absorbed in the absorbing layer. However as we move from thin film to ultra-thin film, this issue will grow in importance.

- Substrate - Glass. In the case of chalcopyrite cells, the choice of substrate can make a significant difference, even though it is not optically or electrically active. For the case of a glass substrate diffusion of Na atoms from the glass into the CIGSe layer during the high temperature CIGSe deposition can be beneficial for the CIGSe layer. However in more recent times the Na has been blocked from diffusing from the substrate and is instead added in a controlled manner after the CIGSe deposition, therefore broadening the choice of substrates.

The uppermost three layers, Al:ZnO, ZnO and CdS, limit the amount of light which is incident to the absorbing layer. This has been heavily optimised during the development of the standard chalcopyrite solar cell. If the absorbing layer is reduced in thickness then this will not impact the amount of light coupled into the absorbing layer. In the case that light is reflected back from the rear of the solar cell and is not trapped inside the absorbing layer, the window layers could play a role in determining the amount of light absorbed. This is because the layer thicknesses will effect the path length of light inside the solar cell device, thus affecting the Fabry-Perot resonance wavelengths created by multiple internal reflections. Nevertheless, these layers will not be the dominant source of losses in the long wavelength spectral region, so we do not seek to optimise the thicknesses of these layers, but it should be understood that some amount of optical optimisation could be performed on the layers, at the risk of effecting the carefully balanced electrical properties. With this in mind, in the following results, we will group together the optical losses caused by the uppermost three layers under the term window layer.

8.2 Simulation of Thin Film Chalcopyrite Solar Cells

In chapter 7 we have developed the correct framework of S matrices, we can use this to calculate the reflection, absorption and transmission of a solar cell as a function of the incident wavelength. We take the standard thin film chalcopyrite solar cell as our first example, this will provide a reference value for absorption which we would ideally like to reach or even surpass with the ultra-thin film. Figure 8.3 shows an area plot of the absorption and all losses in a CIGSe solar cell with absorber layer thickness 2 μm. The hatched area with the white background shows the absorption that happens in the absorbing layer, i.e. the useable absorption. The rest of the area is taken up by reflection

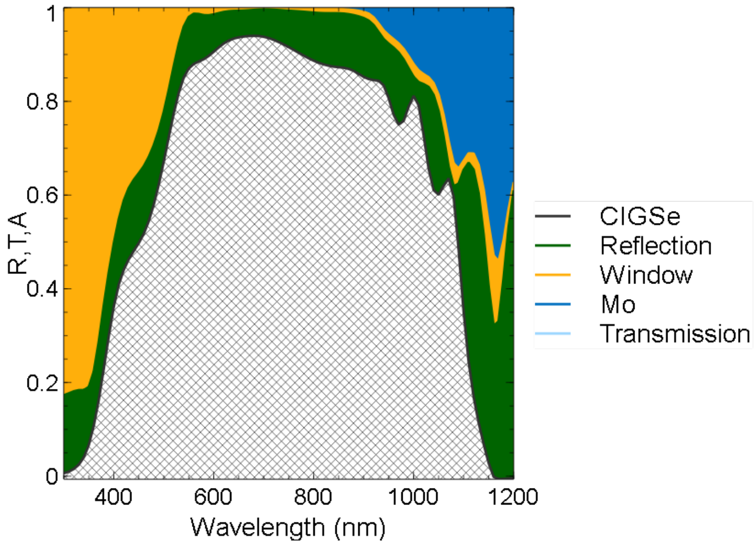

FIGURE 8.3: The reflection, transmission and absorption in a CIGSe solar cell with a 2 μm thick absorbing layer. The back contact is a 200 nm Mo layer resulting in zero transmission for this solar cell.

or absorption in other layers which are treated as loss. The absorption curve for the CIGSe layer comes close to the ideal 'top hat' function with a sharp increase in absorption between 400 and 500 nm due to the window layer band gap followed by a sharp decrease between 1100 and 1200 nm due to the CIGSe layer band gap. If the absorption curve is taken to be equivalent to an external quantum efficiency measurement, which means we assume perfect collection of photogenerated electron-hole pairs, then the expected short circuit current density can be calculated using equation 8.1. For this thin film solar cell we obtain an expected value of 31.16 mAcm^{-2}, which is comparable to the actual short circuit current density for high performance solar cells [69].

In the short wavelength regime (300 - 500 nm), the absorption in the window layer is the dominant form of loss. However since the solar spectrum does not have a very high photon flux density, the effect on cell performance is minimal. For most of the operational wavelengths (500 - 1000 nm) the solar cell is able to absorb between 85-95% of the incident light with the only losses being reflective, which could be further reduced by the inclusion of a standard anti-reflection coating. In the longest wavelength region (1000 - 1200 nm) significant optical losses due to the Mo back contact become apparent. For this thin film solar cell, these losses are not too critical since the solar flux density is also relatively low in this spectral region.

If we transition to looking at the same data but for a CIGSe solar cell with a 400 nm CIGSe layer, shown in fig. 8.4 we see a marked difference. The short wavelength response remains the same, due to the fact that all of the light will be absorbed before reaching the Mo back contact. However the back contact already shows significant losses in the

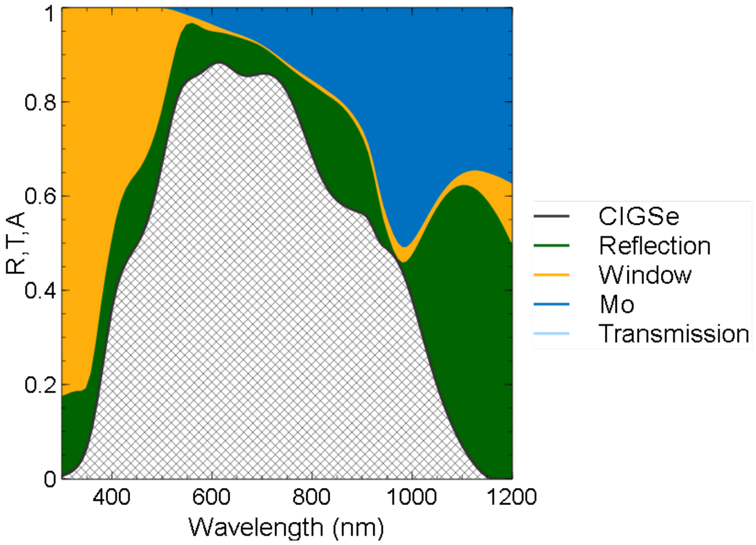

FIGURE 8.4: The reflection, transmission and absorption in a CIGSe solar cell with a 400 nm thick absorbing layer. The back contact is a 200 nm Mo layer resulting in zero transmission for this solar cell.

central spectral region which increase with increasing wavelength. Even the light that is reflected from the back contact cannot be totally absorbed by the ultra-thin absorbing layer and will leave the cell becoming a reflection loss which is significant around 900 nm. Figure 8.5 shows the absorption curve and losses for the same ultra-thin film CIGSe solar cell, but with the Mo layer replaced by an Ag layer. There are very low losses present in the back contact in this case. The absorption also shows more clearly characteristic coherency patterns, with a lower absorption at 800 nm and much higher absorption at 900 nm, this is due to destructive or constructive interference of multiple internal reflections inside the CIGSe layer. However at wavelengths higher than 900 nm the absorption still falls rapidly, this suggests that even for an ideal back reflector like Ag, a light trapping concept would still be necessary. Ag as a back contact would also be impractical due to the poor electrical contact with CIGSe and the likelihood of Ag diffusion into the CIGSe layer during deposition.

Since a back contact that has a high reflectivity and good electrical properties may be difficult to find, we will look into decoupling the two concepts. For this we require a transparent conducting back contact which will transmit the light to a highly reflective surface which does not electrically interact with the solar cell device. An example for this concept would be a transparent conducting oxide back contact, like ITO which has been shown to provide comparable electrical properties to a Mo back contact, with a Ag back reflector behind the ITO layer.

Since the Ag reflector is not required to be in contact with the ITO, we are free to add a spacer layer in between the ITO and Ag layers. As long as the spacer layer

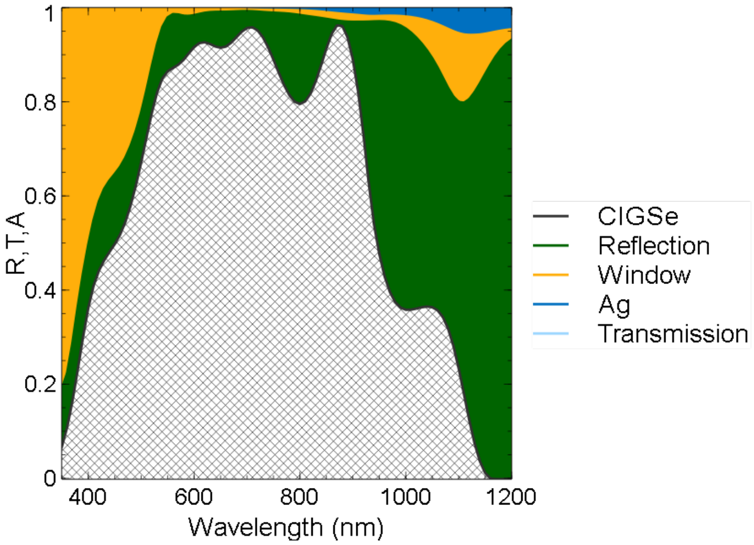

FIGURE 8.5: The reflection, transmission and absorption in a CIGSe solar cell with a 400 nm thick absorbing layer. The back contact is a 200 nm Ag layer provides a higher reflectivity than the conventional Mo back contact.

is non-absorbing in the relevant wavelength range, the only effect will be to change the coherent interference of light inside the layer stack. This can be used to optimise the absorption in the CIGSe layer given a certain thickness of ITO required for good electrical conductivity. Furthermore a spacer layer helps to block diffusion of Ag that may happen during the high temperature CIGSe deposition. The downside to adding a spacer layer is that it may harm the growth and conductivity of the ITO layer, although it may equally be beneficial compared to growing ITO on Ag, dependent on the material chosen as a spacer layer.

In order to eliminate the possibility of diffusion altogether, we can use the glass substrate as the spacer layer. This will effectively mean that the back reflector is separated from the cell device by a millimeter or more of glass. This will have a different effect than placing the back reflector within a few hundred nanometers of the absorber layer. In this case the light returning from the rear side of the substrate will be incoherent with respect to the incident light. For the thin substrate we observe peaks and troughs in the absorption profile over the spectral range of tens or hundredths of nanometers due to Fabry-Perot oscillations (i.e. multiple internal reflections). Such peaks and troughs will still be present for a thick substrate in principle, however they will occur within a few hundreds of a nanometer. Therefore when attempting to measure the absorption profile with a real light source, the spectral bandwidth of the source must be taken into account. This bandwidth will be much larger than the few hundred nanometers of the Fabry-Perot oscillations meaning that a measurement will effectively average out such oscillations. Therefore, while a perfectly monochromatic source might be able to

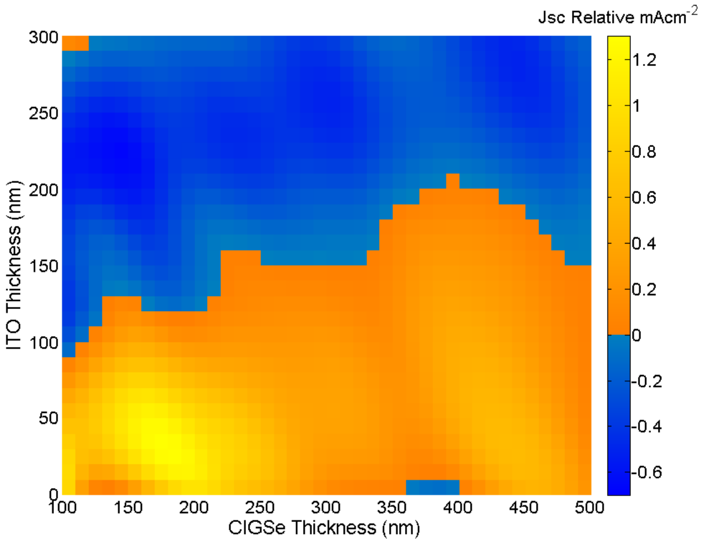

FIGURE 8.6: The short circuit current density (J_{sc}) for a coherent back reflector concept relative to an incoherent concept as a function of both the absorber layer thickness (CIGSe) and the back contact thickness (ITO).

measure the phase oscillations present in a thick substrate, for practical purposes we can consider the light there to be incoherently reflected.

This has two repercussions that need to be discussed. The first a physical one: an incoherent back reflector will not change the coherency pattern of light inside the solar cell device. That means that the absorption of light inside the CIGSe layer cannot be optimised by changing the glass substrate thickness. Furthermore, it means that any increase in absorption in the CIGSe layer will be wavelength independent and also independent on the CIGSe layer thickness. The second repercussion has to do with modelling an incoherent system. The simulation methods presented so far have assumed full coherency of the light involved. With regards to FEM simulations, an incoherent layer is not possible to simulate due to the fact that it is many hundreds or even thousands of times larger than the wavelength of light. Therefore FEM simulations need to be coupled to an S matrix simulation in order to simulate incoherency. The topic of that coupling will be discussed in chapter 11. For now we will describe only how the S matrix method can simulate incoherency since that is adequate for the current topic (incoherent back reflector).

8.3 Decoupled Back Reflector

We will first compare the coherent to incoherent back reflector in the absence of a dielectric spacer. Figure 8.6 shows the relative short circuit current density (J_{sc}) for the coherent reflector compared to the incoherent one. In both cases the wavelength range

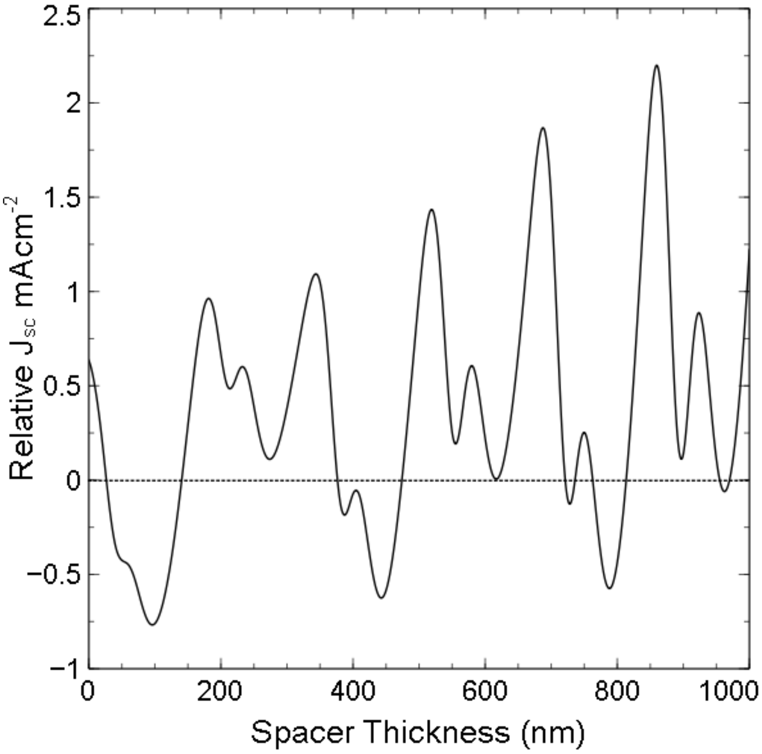

FIGURE 8.7: The short circuit current density (J_{sc}) for a coherent back reflector concept relative to an incoherent concept as a function of the dielectric spacer layer (SiO_2) thickness. The ITO thickness is 200 nm while CIGSe thickness is 400 nm.

used for integration to obtain J_{sc} was $\lambda = 300$ to 1200 nm. The incoherent results in this section were obtained via phase averaging. The relative J_{sc} is then obtained via $J_{sc}^{rel} = J_{sc}^{coh} - J_{sc}^{incoh}$, therefore it is positive when the coherent case outperforms the incoherent case and negative when it performs worse. The limit for the coherent case outperforming the incoherent one can be clearly seen in the figure, the ITO must be less then 100 nm for very thin CIGSe layers, increasing up to 200 nm for 400 nm of CIGSe before decreasing again for even thicker CIGSe layers. However the scale of the performance improvement is also important. For very thin CIGSe films and very thin ITO films the J_{sc} can be improved by over 1 mAcm^{-2} which is a significant improvement. This will be partly due to the fact that it is easier to gain a relatively large increase in performance for a cell with an initially worse absorption. While it is true that a thinner ITO will always be beneficial optically due to loss in the ITO layer, if we assume that at least 200 nm is required for good enough electric conductivity, then the incoherent case seems to be almost universally more beneficial in this case. However it is also visible from the figure that the coherent case is capable of outperforming the incoherent one quite significantly. Therefore we now employ a spacer layer in between the ITO and Ag back reflector where we hope to increase the absorption above the level of the incoherent back reflector.

Figure 8.7 shows the relative absorption increase of a coherent back reflector with a dielectric spacer layer compared to an incoherent back reflector. In both cases the CIGSe and ITO layer thicknesses were 400 nm and 200 nm, respectively. Due to the absence of a spacer layer in the incoherent case, the same reference spectrum was used for the incoherent J_{sc} in each case. The value of the relative J_{sc} at a spacer thickness of zero corresponds to the tile in fig. 8.6 for CIGSe and ITO at 400 and 200 nm, respectively.

As the spacer layer thickness increases we observe peaks and troughs in the J_{sc} relative to the incoherent back reflector. The trend indicates that increasing the spacer layer to thicknesses even beyond 1000 nm can be beneficial to the absorption in the solar cell. However this also has problems associated with it, as the spacer layer thickness increases, not only do the coherent enhancement peaks become narrower, but also in a practical sense, the possibility for fine control over the spacer layer thickness reduces with increasing spacer thickness. This is due to relative error having a larger absolute impact on thicker spacer layers. For this reason we choose to stop the optimisation at a spacer thickness of 1000 nm. Inside of the range presented, the largest increase in J_{sc} is found for a spacer layer thickness of 860 nm with a relative increase of 2.2 mAcm^{-2} compared to the incoherent case. However as discussed, a 5% error in the thickness of the spacer layer could lead to thicknesses of 817 and 903 which both provide only a 0.2 mAcm^{-2} increase. Compare this to the peak at spacer thickness of 344 nm providing an increase in 1.1 mAcm^{-2}. In this case a 5% thickness error leads to thicknesses of 327 and 361 which provide increases of 0.9 and 0.7 mAcm^{-2} respectively. Thus the peak at 860 nm spacer thickness provides a higher optimum value, but the peak at 344 nm is more robust to spacer layer thickness errors.

The reason why the coherent case can outperform the incoherent case for certain parameters has to do with the peaks and troughs in absorption present in the coherent spectrum. The incoherent spectrum essentially averages out these peaks and troughs, meaning that if an equal number of peaks and troughs are present in the coherent case, the coherent and incoherent absorption should agree. However it is possible to engineer the system such that one more peak is present than the number of troughs, meaning that the coherent case has a net increase. Additionally since the solar spectrum is not equal for different wavelengths, peaks at certain wavelengths may be more beneficial than others, further allowing for optimisation.

8.4 Conclusion

To conclude this section on ultra-thin devices before the nanoparticle integration is introduced we summarise three different absorption curves in fig. 8.8. The first curve is

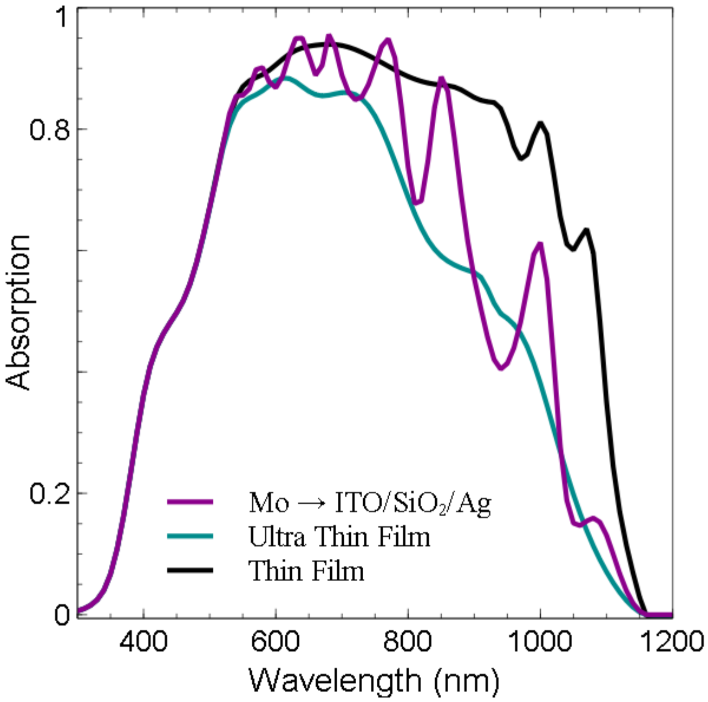

FIGURE 8.8: The absorption curves for three different devices that have been covered in this section. The standard thin film device with 2 μm of CIGSe material, the ultra-thin device with 400 nm CIGSe and finally the optimised ultra-thin film with the Mo exchanged for ITO/SiO_2/Ag with thicknesses 200/860/200.

that of the thin film solar cell with a 2 μm absorber layer thickness with an associated J_{sc} of 31.16 mAcm^{-2} this is the target to be reached or even surpassed by our ultra-thin devices. Secondly we show how the absorption drops when moving to an ultra-thin device with only 400 nm absorber layer thickness without making any other changes. Due to the low reflectivity of the Mo layer, significant losses in the Mo lead to a large reduction in absorption, providing only 24.63 mAcm^{-2} of current density. Finally we show how this can be improved without the use of nanostructuring by decoupling the back contact and back reflectors. By changing the Mo for a stack of ITO/SiO_2/Ag we can increase the absorption resulting in a J_{sc} of 26.80 mAcm^{-2}. For any nanostructuring concept to be worthy of implementation, it needs to be able to beat this result obtained without nanostructuring.

Chapter 9

3D Modelling of Photovoltaics

9.1 Modelling Layer Growth

The finite element method allows excellent control over the simulation geometry. This is not limited to including particles inside a layered stack system, but also extends to modelling the effect the particle has on the layers. All layers which are deposited on top of the particles will be deformed due to the presence of the underlying particles. To model precisely how this growth takes place is beyond the scope of this work, however we can appeal to experiment to at least give an understanding of whether the growth is typically conformal or normal [70]. Conformal growth means that the underlying structure is exactly reproduced in the overlying structure, this can be achieved by allowing the surface to grow directly upwards. Normal growth means that all surfaces grow in the direction of their local surface normal. Confusingly in the literature, conformal growth is often used to mean a mix of both proper conformal growth and normal growth. Both of these cases and any combination can be analytically described for ellipsoidal particles. Due to this analytical description the final geometry is determined by the union of an enlarged particle and the flat layer that should be grown. A schematic of the process is shown in fig. 9.1. The enlarged particle relates to the original particle upon which the layer is deposited via

$$P(a, b, c, x_0, y_0, z_0) \rightarrow P^{'}(g + a, g + b, g + c, x_0, y_0, h + z_0), \tag{9.1}$$

where a, b and c are the three radii of the ellipsoid, x_0, y_0 and z_0 are coordinates of the center point of the particle, g is the amount of growth in the normal direction and h is the amount of conformal growth.

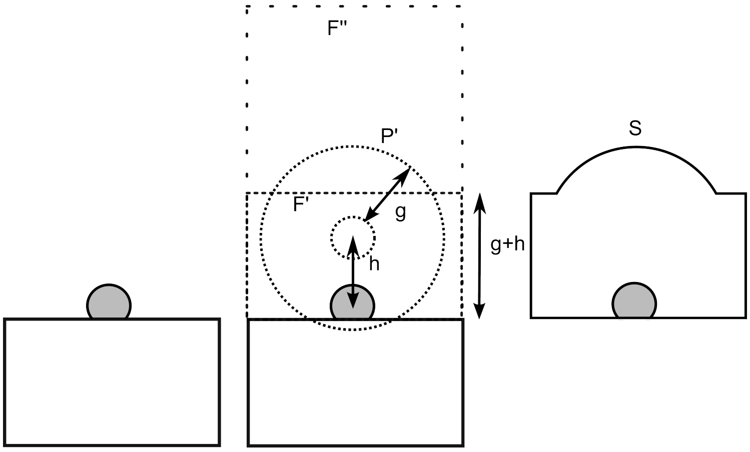

Figure 9.1: Calculating the resultant surface S determined from growth of a layer on top of a nanoparticle using the intermediary surfaces $P^{'}$, $F^{'}$ and $F^{''}$. The conformal growth h and the normal growth g are shown.

The final surface is then obtained via

$$S = \left\{ P^{'} \cup F^{'} \right\} \cap F^{''}. \tag{9.2}$$

Where $F^{'}$ is the flat layer with a lower surface at $z = z_{min}$ which is the height of the flat surface upon which the particle rests (i.e. the substrate). The upper surface of $F^{'}$ is determined by $z = z_{min} + g + h$ since all normal growth for the flat layer is also conformal growth. A final intersection must then be made between the resultant object and a further flat layer ($F^{''}$) with the same lower surface at $z = z_{min}$ and with the upper surface of the computational domain. This ensures that the layer cannot grow in a negative direction, i.e. below z_{min} without limiting the upward growth. This can easily be extended to multiple particles

$$S = \left\{ \bigcup_{i=1}^{N} P^{'} \cup F^{'} \right\} \cap F^{''}. \tag{9.3}$$

Where N is the number of particles upon which the layer is to be grown. This union between the projected ellipsoids means that when particles are relatively close together, such that their projected ellipsoids would overlap, the projected ellipsoid with the highest z value for each x and y value takes priority.

This process will be used in all the following simulations of particles integrated into the solar cell. This allows for a meaningful comparison to cases without nanoparticles, since the volume of absorbing material is kept constant in each case.

9.2 Statistical Distribution

Chapter 6 showed the immense effort required to simulate random arrays of nanoparticles. This is further complicated when trying to include these particle arrays into a layered system. The approach presented in chapter 6, that of using isolated simulations, will not be useable in this case. That is because for the isolated simulations at a single interface, it was not important whether light left the computational domain along the z boundary or the boundaries in x and y, it was either transmitted or reflected in both cases. Inclusion inside a layered system means that the distinction between light leaving the layer/computational domain along z or x and y is crucial. Light which leaves the computational domain through the x or y walls of the domain will no longer be propagated and therefore it will not be determined which fraction of this light is absorbed by the absorber layer of the solar cell device. Since the goal of the nanoparticle integration is to increase scattering into directions parallel to the x-y plane, we can assume that this will cause difficulties if proceeding with the isolated simulations.

Periodic simulations take these plane parallel propagations into account. The two principle downsides are that they model only a single particle size, although this could be overcome by simulating a range of sizes as with the isolated simulations in chapter 6. Secondly they may introduce artifacts due to the fixed phase relationship between neighboring particles, meaning that inter-particle interactions will be coherent in the periodic case whereas they would be assumed incoherent for a random array. In the cases presented here, generally the particles are placed in an absorbing medium, thereby damping any inter-particle interactions. Additionally the low coverage means that inter-particle interactions are generally negligible thereby allowing the use of periodic simulations to approximate randomised arrays.

For a periodic unit cell we choose the hexagonal close packed arrangement. This will maximise the inter-particle spacing for a specific coverage thereby reducing any artificial inter-particle interactions. It should be noted that chemically produced particles which are deposited onto a layer in the solar device may also form in the hexagonal close packed arrangement, albeit likely with a higher coverage.

9.3 Generating a Periodic Surface

Generally periodic boundary conditions are preferable for simulating particle arrays. As long as no particles are touching the computational domain boundary, the boundary will remain periodic. What is more likely is that the surface grown on top of the particles will touch the computational domain boundary. In this case steps must be taken to ensure the periodicity of this surface. To do this we copy and translate the original particle array eight times such that a single central array is surrounded by itself, essentially creating a three by three supercell. We then grow the surface on this supercell, which is not any more computationally demanding than for a single cell, since the analytical method presented here is extremely efficient. Finally the center of the surface grown on the supercell is extracted and forms the periodic surface that was initially desired.

Chapter 10

Photovoltaics with Integrated Plasmonic Nanoparticles

10.1 Possibilities for Nanoparticle Integration

We have already presented the capabilities of plasmonic nanoparticles to localise and scatter light. Now we consider the possible ways in which these capabilities can be exploited by integration in the solar cell. The first property we consider is the localisation of light. Near to the nanoparticle, light intensity is much higher than in the surrounding leading to an increased absorption in material surrounding the particle. As outlined in the previous section, only light absorbed in the CIGSe layer can contribute to the current, therefore to take advantage of this property requires that the particles be very close to or in some way touch the CIGSe layer. Three possible scenarios exist for such close integration, either the particles touch the front or rear side, or they are integrated directly inside the absorbing layer. Direct integration inside the absorbing layer presents significant difficulties, the finely tuned deposition process of the CIGSe layer would need to be stopped mid process to allow for the deposition of the nanoparticles then restarted afterward. It is to be expected that this would seriously negatively affect the material quality of the CIGSe and would potentially need a lot of effort to reoptimise the deposition process. Therefore we rule out this mode of integration for chalcopyrite cells, while noting that for organic solar cells, or solar cells with less stringent deposition procedures, direct integration may be the most beneficial method as the entire particle near field can be exploited.

Considering instead the particle integration at either the rear or front side of the CIGSe layer we can again make some assumptions as to the effectiveness of these two options. The two most popular plasmonic materials, Ag and Au both have interband transitions

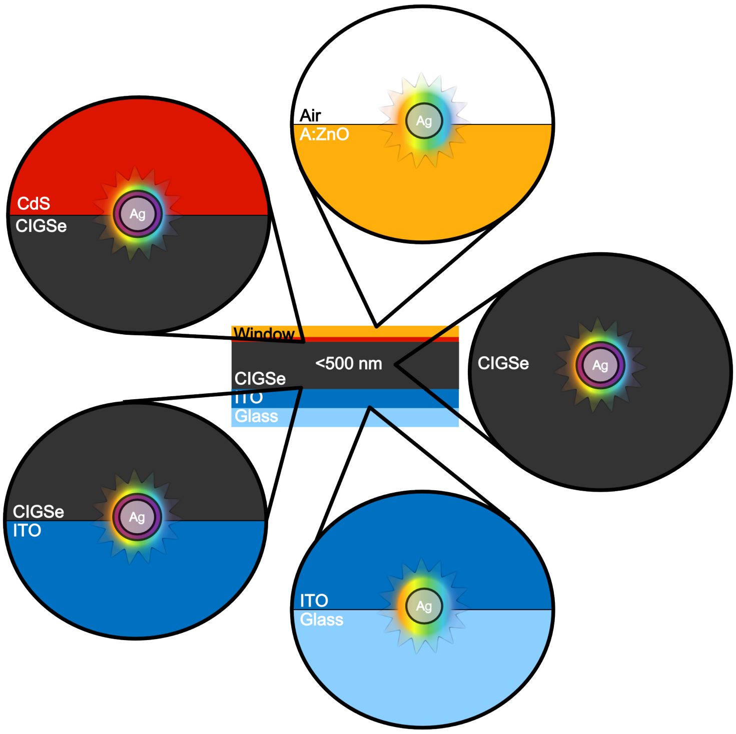

FIGURE 10.1: The five positions in the cell where nanoparticle integration could be profitable. Either at the very front or rear of the device in order to maintain electrical quality or integrated into the absorbing layer. In the absorbing layer the particles can be situated in the bulk or at the front or rear surface.

starting at wavelengths 350 nm and 500 nm, respectively. These transitions cause major absorption losses in the particles for wavelengths shorter than these. Additionally the fraction of light scattered compared to absorbed also in the plasmonic regime tends to be lower for shorter wavelengths. Taken together, this means that plasmonic particles tend to have higher absorption losses at short wavelengths in terms of the operating wavelengths of a CIGSe solar cell (300 nm to 1100 nm). If the particles are integrated on the front side of the absorbing layer, they will tend to absorb this short wavelength light before it can be absorbed by the CIGSe layer. Conversely if the particles are integrated at the rear side, the absorbing layer acts as a natural optical filter, stopping the wavelengths where the particle features high loss from reaching the particle. Therefore the integration of particles on the rear side of the CIGSe layer seem to be the most promising. The only difficulty is that light scattered by larger particles tends to be more directed in the forward direction, which in this case would be away from the absorbing layer. However due to the presence of the interface, the angular scattering spectrum of the particle will be significantly distorted anyway. In this case the rear side integration may still offer a useful absorption enhancement.

The other two places for integration worth considering are at the front or back of the entire device. The idea being that we place the particles in such a way as they have minimal impact on the electrical properties of the cell. Either they can act as an anti-reflection coating on the front side or they lie underneath the back contact, necessitating a transparent back contact. Due to the lack of close contact to the CIGSe layer, the localisation of light will not be exploited in this case, only the scattering of light and associated light path length increase will be utilised. Due to the previously mentioned problem of short wavelength absorption in plasmonic nanoparticles, front side particles do not seem particularly promising. Even if we consider a particle with low losses, the increase in path length of light due to the scattering will be present in the various parts of the window layer as well as in the absorber layer. This means that any parasitic losses in the window layer will also be increased due to the longer path length of light in the window layer. Based on this rear side integration may have more potential. The rear side integration has similar problems in that an increased path length will also increase parasitic absorption in the rear contact. However it retains the advantage that the solar cell will filter out shorter wavelengths, thereby nullifying any increase in parasitic losses at least in the short wavelength range.

Due to the previous analysis, we will focus our attention on particles integrated at the rear side of the solar cell, either directly touching the absorbing layer or integrated behind the back contact.

10.2 Integration with Mo Back Contact

In chapter 8 we have already seen that while Mo provides good electric properties for the solar cell, the optical properties are somewhat lacking. We already introduced the idea of decoupling reflector and contact via changing to ITO. However nanoparticles may also lead the way to a decoupling process. If the nanoparticles are integrated at the the CIGSe/Mo boundary, then they can act as a reflector without interfering strongly with the electrical contact. This is because the space in between the particles should provide ample contacting area for the solar cell device, and if the nanoparticles can be electrically isolated via a shell layer, then they should not deleteriously effect the electrical operation of the device. On the other hand they can bring a large benefit to the optical side of the device, if the majority of the light can be reflected by the particles without interacting with the Mo, it would greatly reduce a significant loss channel in the solar cell. In order to see if this is the case we wish to model the light scattering of a core shell particle at the interface.

As we have already seen in chapter 6, the scattering and near fields of a particle are heavily affected by the presence of an interface. In order to get a feeling for how much of an effect this can have on the overall absorption, we simulate a core shell plasmonic

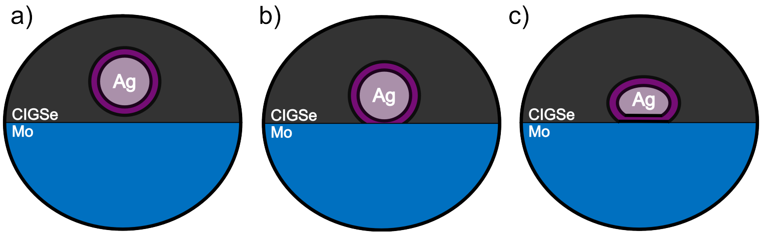

FIGURE 10.2: Three different ways to model a particle at an interface. (a) shows the particle close to but not touching the interface (b) shows the particle making contact with the interface but keeping the spherical shape, while (c) shows a particle deformed at the interface, note that the shell thickness is kept constant in this case.

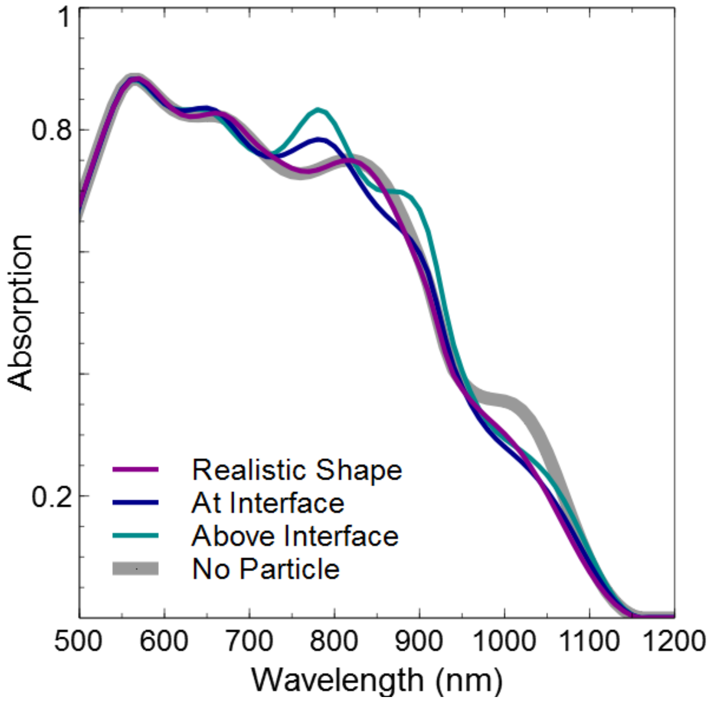

FIGURE 10.3: The absorption spectrum for the three cases shown schematically in 10.2, including a reference without particle.

nanoparticle integrated at the CIGSe/Mo interface of an ultra-thin film chalcopyrite solar cell. The core material is Ag and the shell material is AlSb, the reasons for choosing these materials were discussed in detail in chapter 4. We will simulate the absorption for three cases, firstly if the particle is artificially placed inside the CIGSe layer a few nanometers above the interface, secondly if the particle is touching the interface with a finite extent while remaining perfectly spherical and finally if the particle is touching the interface and is deformed. The exact deformation that occurs in realistic particles is difficult to determine experimentally, especially for the case of the core-shell particles were the core cannot be conveniently probed. Therefore we assume that a deformed core-shell particle will have a total geometry similar to the particles presented in chapter 6, and that the shell core is deformed in the same way, such that the shell thickness remains constant over the whole particle. Figure 10.2 shows the different setups schematically.

Figure 10.3 shows how the absorption curves change depending on the particle position/shape. The difference between the spherical particle above the interface and at the interface is particularly visible at the peak in absorption around $\lambda = 780$ nm for both cases and the second peak around $\lambda = 875$ nm which is only visible for the case of the particle above the surface. These differences can be understood by looking at the field strength averaged in the x-y plane of the FEM unit cell for different depths z inside the solar cell as shown in fig. 10.4. The dashed black lines trace the electric field strength peaks inside the absorber layer. For the first two cases, that of the particle above and at the interface, the peaks both intersect the upper boundary of the absorber layer at a wavelength of around 780 nm causing the increase shown in the absorption at that wavelength in fig. 10.3. Since the field strength profile is oscillatory due to the effect of multiple reflections inside the absorbing layer it means that if a trough in field strength is excluded from the absorber region with the associated peak remaining, the average field strength inside the absorber layer will be increased. This is more pronounced for the cases with integrated nanoparticles compared to flat Mo back contact because the nanoparticles are more reflective than the Mo back contact. If the back contact is not reflective then there will not be the multiple internal reflections necessary to create the peaks and troughs for this effect to be visible. For the third case, the particle is significantly deformed from a sphere, which causes a redshifting of the resonance meaning that no absorption enhancement is observed in fig. 10.3 due to the resonance being redshifted out of the region of interest. The final point to be noted is why the particle above the interface significantly outperforms the particle at the interface at the wavelength 875 nm. As can be seen in fig. 10.4 at this wavelength, a field strength peak in the absorber layer is intersecting with the nanoparticle at the rear of the absorbing layer. Due to this the intensity peak is able to more completely cover the particle above the interface which has a slightly higher z position than the particle at the interface. This means that the particle interacts more strongly with the incident light boosting the reflectivity of the nanoparticles causing the absorption increase seen in fig. 10.3.

With regards to particle positioning the differences in simulation results are rather minimal. This is largely due to the fact that since we have a core-shell particle, the plasmonic core is isolated from the effect of the interface. The biggest difference was visible from changing the shape of the particle from a sphere to a more realistic shape. The results in chapter 6 show how important the realistic particle shape can be to accurate simulations, therefore we will base the following simulations on the more realistic shape. It should therefore be kept in mind that a slightly smaller particle may be necessary compared to the spherical shape in order to counteract the redshifting induced from moving to a more ellipsoidal shape.

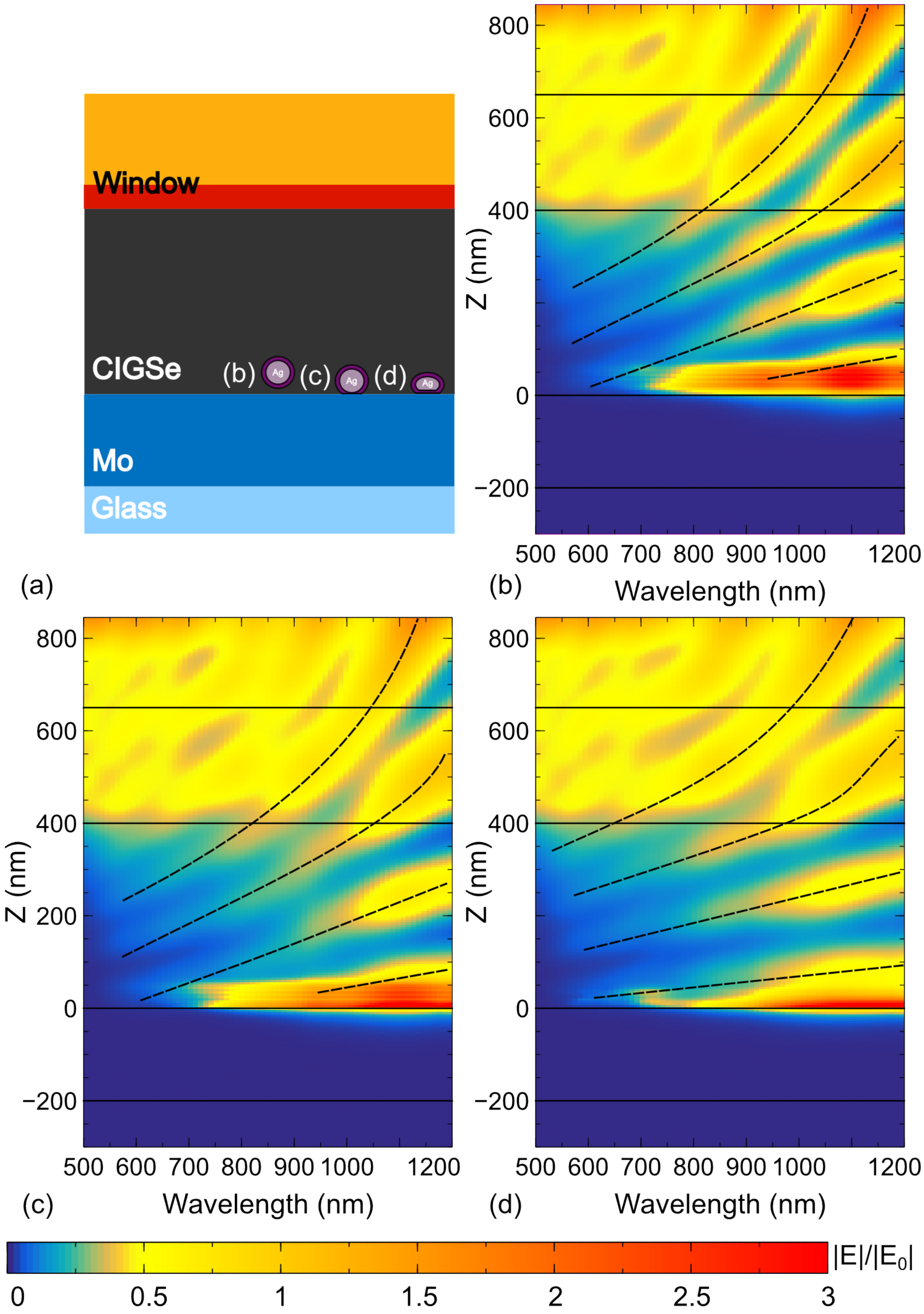

FIGURE 10.4: Part (a) shows the ultra-thin device with integrated nanoparticles. Parts (b-d) show the x-y plane averaged electric field strength inside the solar cell as a function of wavelength for the three cases shown schematically in 10.2. The layer interfaces are marked with solid black lines, dashed black lines are a guide to the eye for the dispersion of Fabry-Perot peaks inside the layers. The electric field strength is normalised to the incident field.

Despite the differences in the absorption coming from different placements of the nanoparticle at the interface, the only case that provided a marginal increase in short circuit current density was that of particle above the interface which increased J_{sc} to 24.91 mAcm^{-2} compared to without a particle (24.65 mAcm^{-2}). The other two cases decrease the overall short circuit current density to 24.30 mAcm^{-2} for the spherical particle at the interface and 24.24 mAcm^{-2} for the realistically shaped particle at the interface. This suggests that while the particles are able to increase the long wavelength reflectivity, the loss in absorption at the relatively shorter wavelengths is too large a disadvantage to be overcome. This loss in absorption is replaced not with increased Mo absorption, but with higher reflectivity of the overall device. This suggests that the particles are acting as a good reflector, but they are acting to shorten the total cavity thickness, if that thickness is measured from the top of the particle to the upper surface of the absorbing layer. This means that less light can be absorbed due to the cavity being shorter. Therefore the particles are reflecting but are not scattering into higher angle modes which would increase the path length significantly thereby reducing reflection.

The other possibility is that the shaping of the layers above the absorber layer due to the underlying nanoparticle causes there to be a higher reflection from these layers. This could be possible due to the fact that light is hitting the surface at a more oblique angle due to the curved surface there. However in the case presented here, since the particle is much smaller than the layer thickness, the effect on shape of the above layers is minimal, meaning they are very close to flat. Figure 10.5 shows the reflection of three different devices. As a reference the reflection for the case of no particle is included. The reflections for the cases of shaped and flat layers above the particle provide almost identical reflections. Especially in the wavelength region 600 to 750 nm where the reflection is higher than without a particle. Therefore we can assume that the effect of layer shaping is minimal on the overall device performance.

In order to minimise the negative impacts of incorporating the nanoparticles directly into the absorbing layer we also consider integration into a device with an ITO back contact and an Ag back reflector.

10.3 Integration with ITO Back Contact

In chapter 8 we have shown that an ITO back contact with an Ag back reflector and an optimised intermediate layer can provide a more efficient ultra-thin device than with the standard Mo back contact. We now investigate whether the inclusion of nanoparticles into this device can further boost the performance.

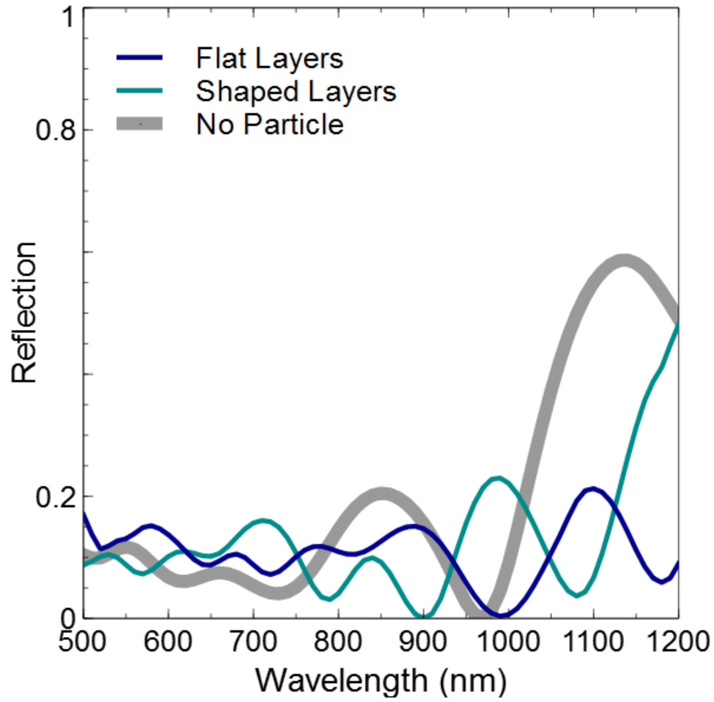

FIGURE 10.5: The reflection for three different ultra-thin film solar cell devices. Shaped layers refers to the case where the layers above the nanoparticle are deformed due to the particle presence, flat layers assumes that all layers above the particle remain flat.

We again present three different cases. In each case the particle is given a realistic shape and is in contact with the interface. The three different interfaces as well as the layer thicknesses of the CIGSe/ITO/SiO_2/Ag layers are shown in fig. 10.6. At the CIGSe/ITO interface a shell for the plasmonic particle will be necesssary as has been discussed in the previous section. Although the particles integrated underneath the ITO and SiO_2 layers would be isolated from the CIGSe layer, we include the shell also for these cases in order to maintain comparability between the different simulations.

Figure 10.7 shows the absorption curves for the three different cases compared to a reference without nanoparticles. Due to the large thickness of SiO_2 present in all cases, the spectra have an extremely large amount of resonances, however conclusions may still be drawn. When the nanoparticle is not situated inside the absorber layer, the two absorption spectra look very similar. Whether the particle is above or below the SiO_2 spacer layer does not seem to play a large role. This suggests that either the particles not situated inside the absorber layer do not interact strongly with the incident light, or that particles at the ITO/SiO_2 interface are scattering strongly into the forwards direction, so that the light can still interact with the spacer layer. Contrast this to the case of the particles integrated into the CIGSe layer, here fewer resonances are observed, this is because a significant proportion of the light is reflected back by the particles and does not reach the underlying SiO_2 spacer which would increase the number of resonances.

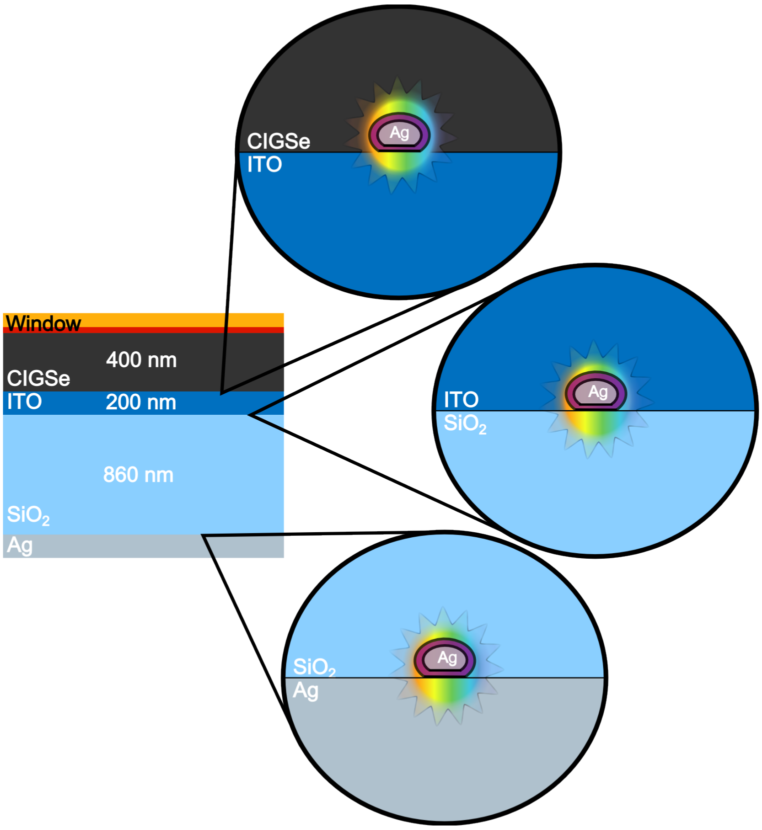

FIGURE 10.6: Nanoparticle integration into the ultra-thin device with ITO back contact can be principally applied in three different locations. The CIGSe/ITO interface, the ITO/SiO_2 interface or the SiO_2/Ag interface.

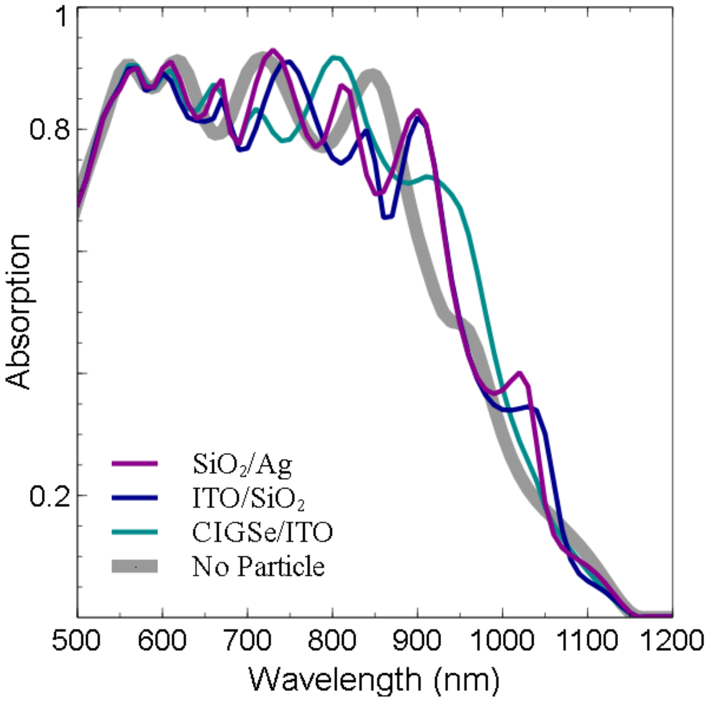

FIGURE 10.7: Absorption spectra for the three cases of integrating nanoparticles into an ITO back contact device as described in fig. 10.6. The legend indicates the two materials which form the interface where the particles are situated.

The mode structure when viewed in the form of the electric field strength distribution per wavelength gives some insight in to the absorption curves. Figure 10.8 shows intense Fabry-Perot resonance in the ITO/SiO_2 layers at wavelengths of around 840 and 1040 nm. That is because the most highly reflective interfaces are the Ag back reflector and the ITO/CIGSe interface due to the large jump in refractive index between these two materials. This will cause a cavity to form surrounding the ITO and SiO_2 layers. The mode structure makes it clear that these layers contain the intense resonance not only because the intensity in those layers is highest, but also the resonance wavelengths occur when a node in the intensity is at the CIGSe/ITO interface. Since there is always a node at the SiO_2/Ag interface due to reflection, when a node is also present at the CIGSe/ITO interface it means an exact number of half wavelengths fits inside the cavity (ITO + SiO_2) which is the Fabry-Perot resonance condition. Unfortunately these intense resonances are not contained inside the CIGSe layer and are mainly detrimental to the CIGSe absorption since a lot of light is absorbed in the ITO. Correspondingly the intensity contained in the CIGSe layer drops significantly at exactly the Fabry-Perot resonance wavelength. In contrast the nanoparticle provides a relatively broadband intensity enhancement as long as a node does not pass through the particle position meaning that almost no light can interact with the particle.

It is also visible that the mode bands bend significantly at certain wavelengths. The mode bands will tend to bend when moving from material to material based purely from the refractive index. They have a steeper gradient with respect to wavelength in lower index materials and a lower gradient in higher index materials, this is purely due to the wavelength in the material changing and the resonance either being compressed or stretched out in different materials. However other more extreme bending is visible at the Fabry-Perot resonance wavelengths. In this case the modes in the CIGSe rapidly change structure when moving through the resonance wavelength. This effect is most visible in part (b) at 1040 nm wavelength. The sudden change in the mode structure suggests a phase shift being introduced. The same general trend as with the Mo back contact is visible in that when a resonant intensity peak is on the edge of leaving the absorber layer, the total absorption also peaks at that wavelength.

The device structure without the presence of nanoparticles reaches 26.80 $mAcm^{-2}$. By including the particles this changes to 26.34, 25.93 and 25.44 $mAcm^{-2}$ for the particle inside the CIGSe, ITO and SiO_2, respectively. This points to the fact that the nanoparticle can adversely effect the delicate coherent enhancement present by slightly changing the mode structure inside the solar cell. It also appears that having the particles placed directly inside the absorbing layer is beneficial, probably due to better light trapping and the ability to exploit near field enhancement.

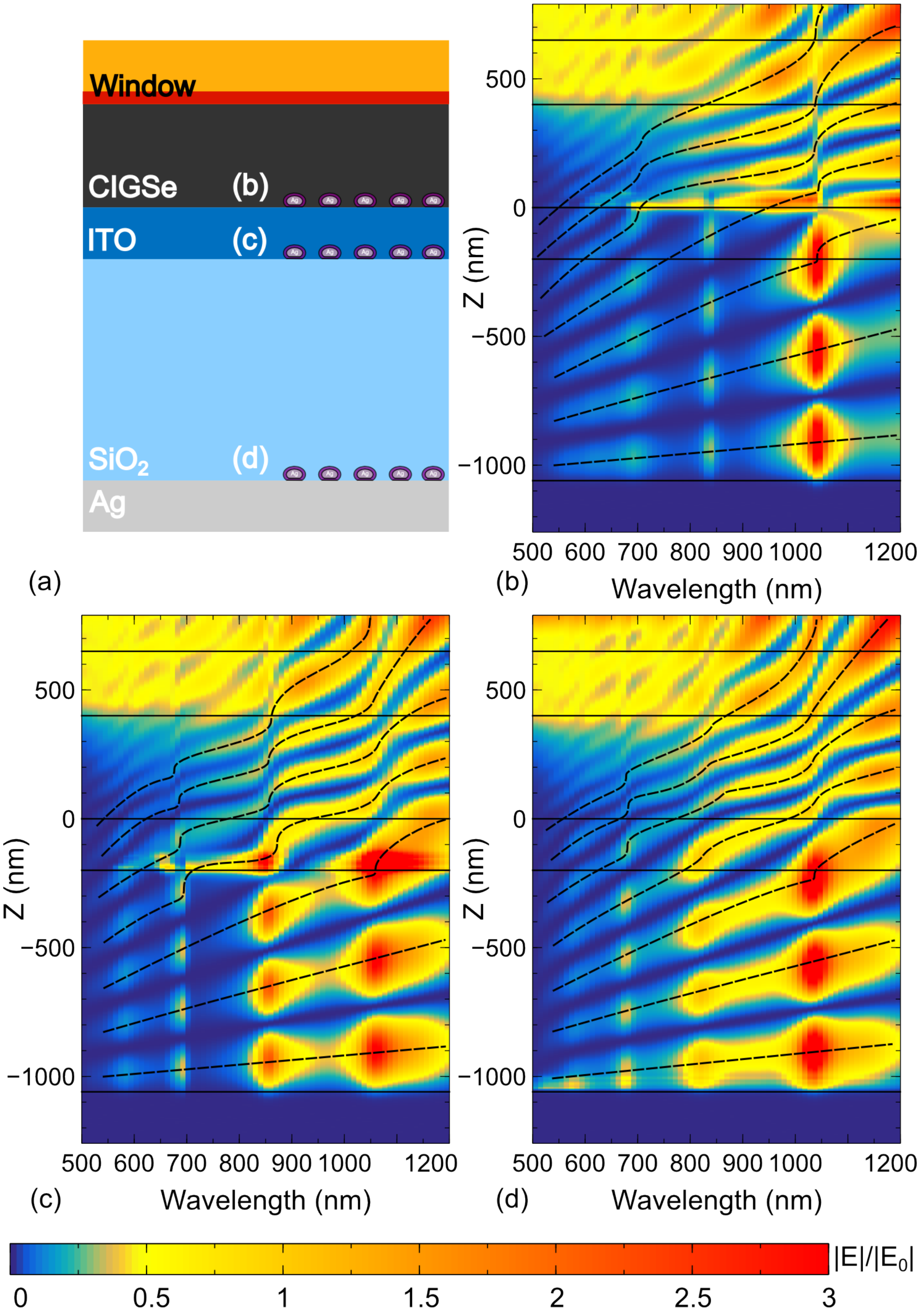

FIGURE 10.8: Part (a) shows the ultra-thin device with integrated nanoparticles and coherent back reflector. Parts (b-d) show the x-y plane averaged electric field strength inside the solar cell as a function of wavelength for the three cases shown schematically in 10.6. The layer interfaces are marked with solid black lines, dashed black lines are a guide to the eye for the dispersion of Fabry-Perot peaks inside the layers. The electric field strength is normalised to the incident field.

The results presented in this section have shown that there is a large potential gain to be made by engineering the coherency of light inside the solar cell device. The risk that comes with this potential gain is that the increase is very tightly coupled to all variables in the system. Practically speaking, small variations in layer thicknesses or even just changing the incident angle can cause the same coherency effects to instead give a decrease in absorption. Adding the nanoparticles into the equation, even in the case shown here for periodically arranged identical particles, tends to perturb the coherency effects so strongly that it is a difficult task to try and optimise for the coupled system. Furthermore, taking into account that realistic particles may be randomised in their geometrical properties as well as their positions and orientations, it seams that it may be unrealistic to aim for a coherent enhancement when nanoparticles are involved. The question still remains as to whether serious gains can be made by incorporating the nanoparticles in an incoherent fashion, which will be the topic of the following chapters.

Chapter 11

Coupling Methods

11.1 Coupling Methods for Nanooptical Simulations

In this work we have already presented multiple simulation methods (Mie Theory, FEM, Scattering Matrix) which have been able to give us useful results on their own. Now we seek to combine these simulations together by the exchange of information between the different simulations. Due to the FEM being a very general method, it is capable of simulating exactly the same things as the scattering matrix method and as Mie theory. However since the method is relatively computationally expensive, we desire to use the FEM only when strictly necessary. Therefore the proposed coupled simulations are:

- Coupling between scattering matrices and Mie theory.
- Coupling between scattering matrices and the FEM.

The first proposal is in order to dispense with the laborious FEM step altogether. This has the potential to greatly increase the speed of computation, at the risk of loosing physical accuracy. The second proposal is partly to speed up the simulation for regions where the problem is effectively one dimensional, but also to overcome a weakness of the FEM, namely the difficulty with handling length scales much larger than the wavelength.

11.2 Coupled Scattering Matrix Simulation

We first discuss the method by which a different arbitrary simulation can be coupled to a scattering matrix simulation. As we have previously seen, the scattering matrix method condenses the presence of a layered stack system into a matrix that describes how electric

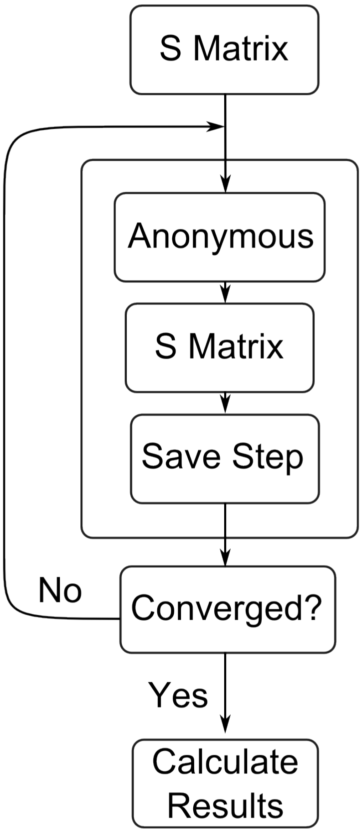

Figure 11.1: Block diagram form of the algorithm used to iteratively couple between an S matrix simulation and some other anonymous simulation.

or magnetic fields incident on either side of the layered stack are mapped to outgoing fields on either side of the layered stack. Therefore the principle method for coupling to an S matrix simulation is to provide field values on either side of the layered stack, along with the associated k vector. Likewise a scattering matrix simulation can couple to some other simulation by providing the outgoing fields and associated k vectors.

We first imagine coupling the S matrix simulation to an anonymous simulation that simply takes in field values at one edge of the layered stack and returns field values that should be used as the input for a second S matrix simulation. The process can either begin with the S matrix or the anonymous simulation, however for this example we will begin with the S matrix simulation.

Figure 11.1 shows the iterative coupling process between an S matrix simulation and an anonymous simulation. The coupling algorithm begins with an initial S matrix simulation which provides the initial conditions for the coupling process. An iterative process then begins where the S matrix and anonymous simulations are run one after the other, passing the fields from each simulation to the input fields of the following simulation. This iterative process has a termination condition, which is typically a tolerance for the total field strength being passed from one simulation to the other. When the field

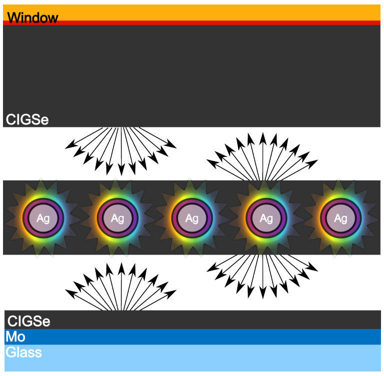

Figure 11.2: Schematic for the coupled simulation of core-shell plasmonic nanoparticles integrated into an ultra-thin CIGSe solar cell using the Mie + SM method.

strength value is below the tolerance value the coupled process terminates. During each step the results of each simulation need to be saved and the total solution is found by combining the results for each step.

The algorithm relies on the total field strength being passed between the two simulations reducing over the course of many iterative steps. This will be true as long as the total losses in the system are more than the gains in the system. For the case of solar cells and plasmonic materials, this will always be fulfilled since all materials have an imaginary refractive index (k value) greater or equal to zero. If however gain materials were included which have a negative k value, careful attention should be paid as to whether the algorithm still converges. Other sources of loss are the outgoing fields on the side of the layered stack which is not coupled to the anonymous simulation, and any losses introduced by the anonymous simulation itself. This ensures that the algorithm also converges for non-absorbing media, so long as the outgoing field from the layered stack on the non-coupled side is greater than zero.

A schematic image of the algorithm is shown in fig. 11.2 for the system of plasmonic core-shell particles integrated into an ultra-thin CIGSe solar cell. The flat layers are handled by the SM simulation, while the scattering and absorption due to the particles is handled by a Mie theory simulation. A range of coupling angles is shown for coupling between the simulations, note that these coupling angles are independent of the angle of incidence.

Given this basic algorithm, there are two methods that can be used to couple the simulations together, each with its own physical meaning. The coherent method couples the actual complex field values at edges of the layered stack. In this case the anonymous function takes on a three component complex vector field with an associated k vector for each coupling angle and returns the same. To ensure the coherency of the final result the fields inside and at the edges of the layered stack are coherently summed, with the reflection, transmission and absorption inside the layered stack being calculated from these fields. The incoherent method is a simplification to this process. We first convert the outgoing fields from the layered stack into intensities $I = |E|^2$ with an associated angle as measured from normal to the layered stack. For instance, in the initial simulation, where no light has been scattered, only one of the coupling angles will have a non-zero intensity (the one which corresponds to the angle of incidence). However after light has interacted with a scattering object, other coupling angles may contain a non-zero intensity, meaning that all of the coupling angles need to be calculated.

Since the intensity is a real valued positive scalar quantity it does not contain information on the phase or polarisation state of the outgoing wave. In this case the anonymous function takes in the intensity and returns an intensity for each coupling angle. Since phase information does not carry over between iteration steps, each S matrix simulation can separately compute the reflection, transmission and absorption, with the final result being the summation of the results for each individual simulation. It should be noted that each individual simulation is fully coherent inside of itself, only that iteration steps do not coherently interfere with each other. Additionally it is implicitly assumed that the polarisation state of the light is not changed by the anonymous simulation, meaning that each S matrix simulation step has the same polarisation.

The advantage to the incoherent coupling method is that the anonymous simulation can be simplified or even come from experimental data. Experimentally it is typical to measure intensities such as the reflection R instead of the reflected field E_r. Therefore if the anonymous function is generated from experimental data, it will likely only be able to provide intensity inputs for the S matrix simulation. The obvious downside to the incoherent coupling is that it is not able to simulate coherency effects. As a specific example, if we wish to simulate nanoparticles placed into a layered stack, the question as to whether it lies at a node or anti-node of the oscillating electric field or somewhere in between, will greatly effect how the particle reacts to the incident field. However if we consider that in realistic cases the particle position may vary quite significantly from particle to particle, the coherency effect may not be relevant to the simulation. In this case it may be appropriate to use the incoherent coupling which is significantly easier to implement without a great loss of accuracy.

11.2.1 Test Cases - Perfect Reflector and Transmitter

As test cases for the iterative coupling algorithm, we present results for two simple cases: a perfect reflector and transmitter. These cases do not require the use of an iterative coupling method, therefore we can verify the results by comparing to standard S matrix

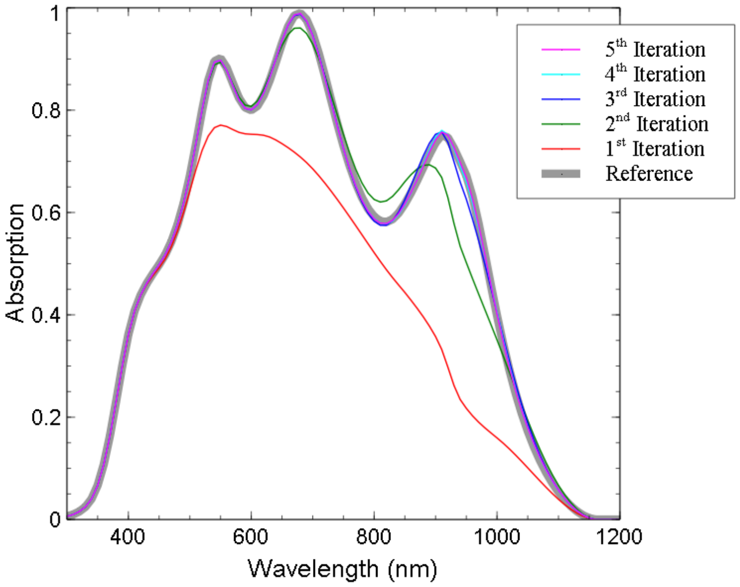

FIGURE 11.3: The absorption contribution from each iteration of the coupled SM simulation with a perfect reflector coupler and field matching boundary conditions.

simulations. To motivate the later transition to modelling solar cells, we will implement these simple cases also in a solar cell. We first consider a standard ultra-thin film chalcopyrite solar cell, the details of which are given in chapter 8. The only difference is that instead of the typical Mo back contact/back reflector used in chalcopyrite solar cells, we will instead use a theoretical perfect reflector. For the case of an S matrix simulation, this is trivially achieved by setting the refractive index of the transmission region to be $n = 0$, $k \to \infty$. This is equivalent to a perfect reflector also called perfect electric conductor, to understand this we have to look at the permittivity instead of the refractive index. The permittivity given by this complex refractive index will have a negative and infinite real part and zero imaginary part. This means that the material is able to reduce the field inside the material to zero due to the real permittivity and will have zero losses due to the imaginary part of the permittivity. In the case of the coupled simulation, the anonymous simulation will take the electric field given in the transmission region and return it to the S matrix simulation at the same angle, including a phase shift by π.

Figure 11.3 shows the different iteration steps for the absorption in a 250 nm thick CIGSe layer integrated into the aforementioned solar cell. The reference value calculated from a single S matrix simulation (i.e. without coupling) by including a perfect reflector material is also shown. The first iteration simulates only a single pass through the absorbing layer (with no reflections at the rear side) therefore the result lacks any peaks and valleys that result from multiple reflections inside the absorbing layer. The second iteration already adds significant structure to the spectrum resulting from light being reflected at the perfect reflector back contact and a small fraction being reflected at the

CIGSe/CdS interface. This means that the second iteration includes both the second and third passes of light through the solar cell. Subsequent iterations further refine the peak structure, with the peaks visibly converging to the reference value for increasing number of iterations. Due to the need for multiple iteration steps, the coupled approach reaches the result slower than the direct approach. To further test the formalism and to present an example where the coupled approach can outperform the direct approach we move on to the perfect transmitter.

The second test case is a perfect transmitter. The transmitter will be used to couple two different S matrix simulations. The algorithm presented in section 11.2 can be extended to include a further S matrix simulation below the initial one. In this case the anonymous simulation must be capable of taking input angles from 0 to π and returning output values at these angles. The inputs for the anonymous simulation on the range 0 to $\pi/2$ come from the upper S matrix simulation while the lower simulation provides the inputs from $\pi/2$ to π.

We move now to a more realistic solar cell example, using a transparent conducting oxide (ITO) as the back contact. Since the material is transparent, light will be transmitted into the glass substrate. If an Ag back reflector is then placed on the rear side of the glass substrate, it will be able to reflect the light back into the solar cell. We have already discussed in chapter 7 the fact that macroscopically thick layers such as the glass substrate here must be treated incoherently. To reiterate, a fully coherent treatment of the propagation of light through a structure with a macroscopic thickness will include the Fabry-Perot resonances that would theoretically form in such a structure. However the bandwidth of these resonances is much less than a single nanometer. There are many reasons why these resonances are not detected in practice, very slight variations in the substrate thickness, on the order of nanometer variations, will tend to shift peaks and troughs of the resonances. These peaks and troughs will tend to become blurred out since they are each shifted a small amount compared to each other. Another way to understand this incoherence is that any light source used to measured the reflection, transmission and absorption will itself have a finite bandwidth. If the bandwidth is larger than the bandwidth of the Fabry-Perot resonance, then it will not be capable of resolving this resonance.

Simulating this incoherency can be easily achieved using the coupled method we have presented. In this case we do not couple the field values between the two different S matrix simulations but the intensities. Thus we split the solar cell into an upper simulation including the layers Air/AZO/ZnO/CdS/CIGSe/ITO/Glass and a lower simulation including the layers Glass/Ag/Air. The anonymous simulation in this case couples an incoming Intensity at an angle of θ to the same outgoing angle. Therefore the input

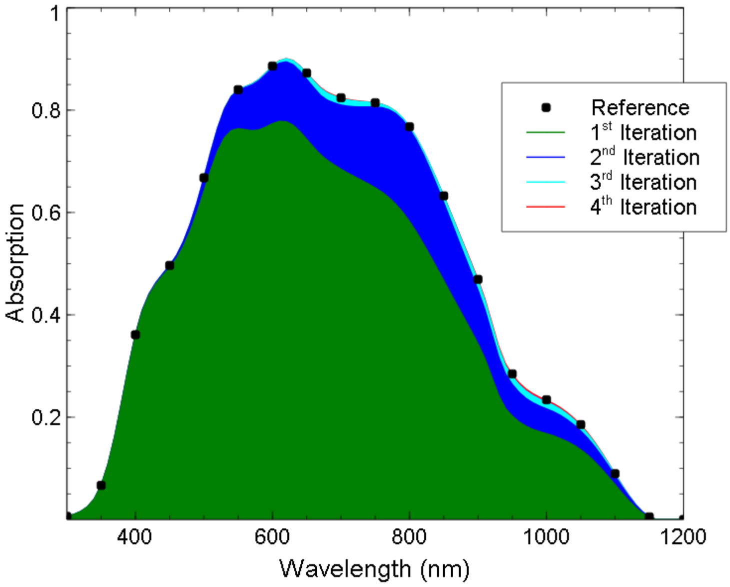

FIGURE 11.4: The absorption contribution from each iteration of the coupled SM simulation with a perfect transmitter coupler and intensity matching boundary conditions.

intensity to the interface will pass through without any change, as an analogy to the perfect reflector we call this behaviour the perfect transmitter.

The other approach to simulate incoherency which was covered in chapter 7, is to take the average of repeated simulations where each time the phase of the light inside the incoherent layer (here the glass substrate) is varied. It however requires multiple simulation steps to take into account the different phases. Therefore depending on the amount of phases necessary, and the amount of iterations necessary in the coupled approach to reach convergence, this method of achieving incoherency can be outperformed by the coupled approach.

In fig. 11.4 the absorption of the 250 nm CIGSe layer in the solar cell setup previously described is shown. The absorption calculated using the coupled method is subdivided by area into the amount of light absorbed during each iteration step. The reference dots were calculated using the phase average of multiple S matrix simulations. In contrast to the previous coherent example, the structure of the spectrum is essentially present already after the first pass through the absorbing layer (iteration 1). This is because since the iterations are incoherent with one another no coherency effects due to interference between forwards and backwards propagating waves can arise. With an increase in the number of iteration steps the total absorption converges to the reference value. This was verified at every wavelength, even though only certain wavelengths for the reference value are shown for readability.

The two results presented seem to show convergence to their respective reference values, however for a more in depth look we turn to analysing the convergence at a single

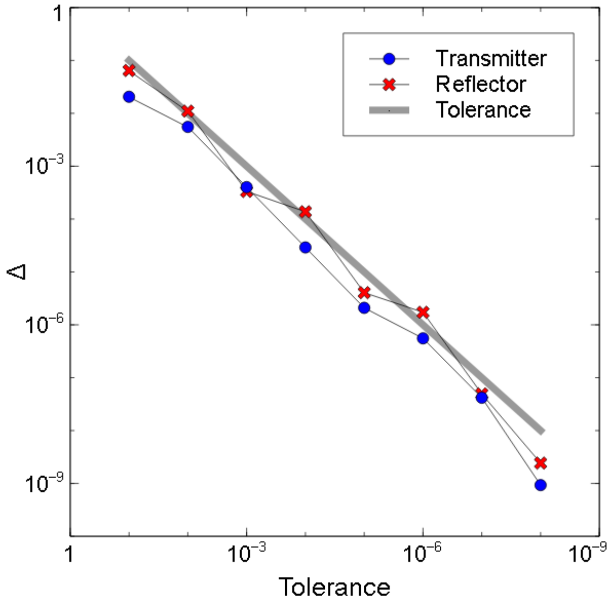

FIGURE 11.5: The convergence of the residual error for the coupled method compared to the direct method for a selected wavelength in figures 11.3 and 11.4.

wavelength. In doing so we will choose the wavelengths which seem to show the worst convergence based on figs. 11.3 and 11.4. Figure 11.5 shows the normalised residual error $\Delta = |A_{Coupled} - A_{Direct}|/A_{Direct}$, between the absorption at a particular wavelength using the coupled approach compared to the direct approach which should be exact. The x axis shows the coupling tolerance, this value determines when the iterative coupling process terminates. When the total intensity being passed from the S matrix simulation(s) to the anonymous simulation, or vice versa, is less than the tolerance, the coupling process terminates. This means that the residual error calculated should be bounded by the coupling tolerance.

In the case of the transmitter the coupling is incoherent, meaning that more iterations always increase the total value of e.g. absorption. This leads to the expected behavior that the residual stays bounded by the tolerance at all orders of magnitude. Here we show the convergence at 1000 nm wavelength which seems to required the most iterations based on the graph. In this case we do indeed see that the residual error stays below the given tolerance.

For the case of the reflector the coupling is coherent, meaning that further iterations can either increase or decrease total values e.g. absorption, due to interferences. Therefore individual iterations may not significantly move the total result closer to the reference result, even though the total coupling intensity will decrease with each iteration. This can be seen in fig. 11.3 at wavelengths around 800 nm the 2nd iteration causes the absorption to jump above the reference value meaning that the residual is not significantly decreased while the intensity will have decreased significantly due to the increased absorption. Therefore we investigate the convergence properties at this wavelength since they can be expected to be worse due to the reason just mentioned. In fig. 11.5 although the residual error for the reflector stays mainly underneath the tolerance, at certain values it can actually rise slightly above the tolerance value given. At these points the coherency effect meant that the absorption did not move significantly closer to the reference value compared to the previous value. However, in general the residuals for the reflector on average are below the given tolerance and show the same behaviour with respect to the tolerance. The important thing to note about this result is that when using amplitude coupling, a lower tolerance value should be given than for intensity coupling in order to ensure the same level of convergence.

11.3 Coupling S Matrix to FEM

The coupling between the S matrix method and the FEM is relatively straightforward [71]. The S matrix simulation requires field amplitudes and associated k vectors of incoming waves at the simulation boundaries and provides the same for the outgoing waves. Although the FEM can take arbitrary sources, it is most convenient to limit this to a plane wave incident source since that is the output of the S matrix simulation. Given this source the FEM will calculate the electric field at all points in the computational domain. In order to couple to the S matrix simulation we need to express the outgoing wave along the domain surface coupling to the S matrix in terms of plane waves. To achieve this the Fourier transform of the outgoing wave is taken, this naturally decomposes the outgoing wave into a plane wave basis.

This can then be included in the previously discussed coupling algorithm, with the FEM simulation taking the place of the anonymous simulation. Note that the iteration loop can start with either the FEM simulation or the S matrix simulation. For the case a nanostructured chalcopyrite cell, incident light will first interact with the nanostructured layers, i.e. the layers where using the FEM is necessary, therefore the coupling process will begin with an FEM domain. The iterative coupling process for which we now present results had already been implemented into the FEM software package JCMsuite which has been used for FEM simulations in this work. Due to this, the FEM simulations were not integrated directly into the previously outlined iterative coupling algorithm, however we have shown how this can in principle work and note that the actual implementation in JCMsuite is very similar to the proposed coupling method presented here.

Since the principle advantage to coupling an S matrix simulation to an FEM simulation is to be able to simulate incoherent layers, we will focus entirely on results containing such layers. Incoherent layers have already been introduced earlier in this chapter. Note that even a fully coherent modelling of such thick layers would be impossible due to the thickness being many thousands of times the wavelength. In this case a coupling between FEM and S matrices can be used in order to simulate the thick glass block.

11.3.1 Single Thin Film and Glass Substrate

We first look at an example that can be treated without use of the FEM in order to verify the approach. As our test case we look at a thin film on a glass substrate. The thin film has a thickness of 300 nm and a refractive index of $n = 3$. The glass substrate has a thickness of 1 mm and a refractive index of $n = 1.5$, and light is incident normally to the film. The FEM computational domain is 2D consisting of a layered system of PML/air/film/substrate/PML where only 200 nm of the glass substrate is included inside the FEM domain. Coupled to this is the 1D simulation of the remaining substrate e.g. 1 mm including the semi-infinite lower half space of air below the substrate. The thickness of the substrate will be varied as

$$t = t_0(\frac{9}{10} + \frac{n}{5(N-1)}), \tag{11.1}$$

$$n = 0, 1, 2, ..., N-1. \tag{11.2}$$

Where N is the total number of thicknesses to be included. This gives a variation in thickness of ±10% that includes N steps. Since the problem is effectively 1D in nature, this can be easily calculated using intensity coupling and the S matrix to obtain the phase averaged result, this provides a reference solution to compare the FEM results to.

Figure 11.6 shows the reflection from the film/substrate structure for two different phase averaging amounts. The upper image shows the reflection where only two different thicknesses are used for the phase averaging process. Due to the low number of thicknesses used, the reflection appears very noisy compared to the reference solution. This is due to the phase accumulated in passing through the 1 mm glass substrate, which interferes coherently with the light inside of the film. In reality this light would be incoherent with respect to the light in the thin film, thus the phase accumulation is unrealistic. By increasing the amount of thicknesses used to twenty as shown in the lower image, the coupled FEM reflection is in much better agreement with the reference reflection. Generally the agreement seems to be within 1%, however at certain wavelengths the agreement is as poor as 5% although these wavelengths are exceptions. It means that mean deviation between the FEM result and the S matrix result converges rapidly while

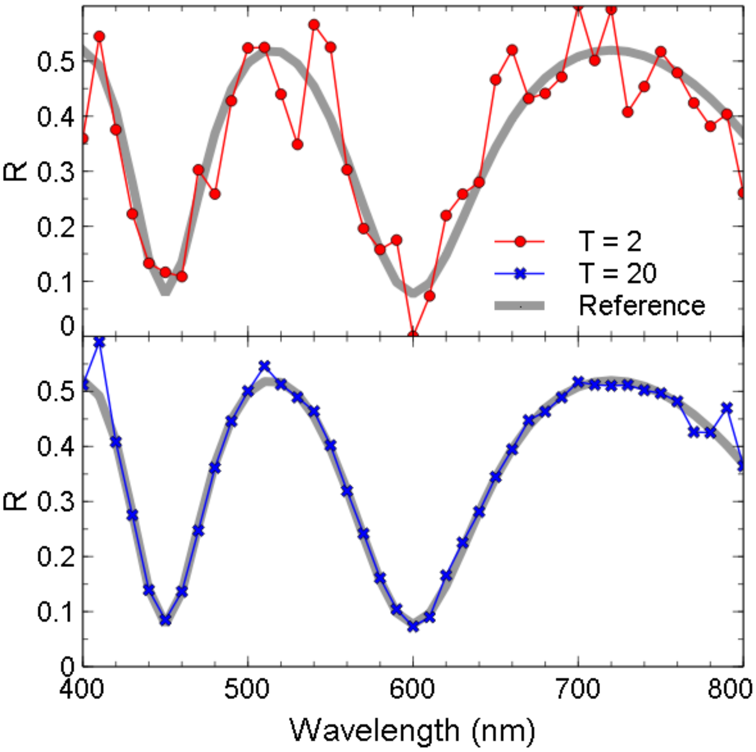

FIGURE 11.6: The reflection curve from a simple system of a single 300 nm thin film with refractive index $n = 3$ on a glass block with thickness 1 mm. T is the amount of thicknesses used in each case, the upper image shows phase averaging with two different thicknesses, the lower image uses twenty different thicknesses.

the maximum single wavelength deviation converges at a much slower rate. However this is not problematic since we are optimising for the short circuit current density J_{sc} which is derived from an integration over all wavelengths, therefore as long as the mean response for all wavelengths converges well, the value of J_{sc} will also converge well with the number of thicknesses.

11.4 Coupling S Matrix to Mie Theory

In using Mie theory as the anonymous simulation in fig. 11.1 some approximations must be made. That is because Mie theory expresses results in a spherical wave basis, while the S Matrix simulations propagate light through the layered stack in a plane wave basis. The spherical wave expansion can be approximated as a plane wave expansion in the far field limit. Therefore we assume that the far field limit can be used to obtain the angular distribution of light being scattered from the particle. This limit tells us how much light intensity is scattered into each angle, however the phase cannot be determined since the scattered light will not actually be a plane wave inside the thin film. Due to the inability to incorporate the phase of the plane waves into the simulations we instead use intensity

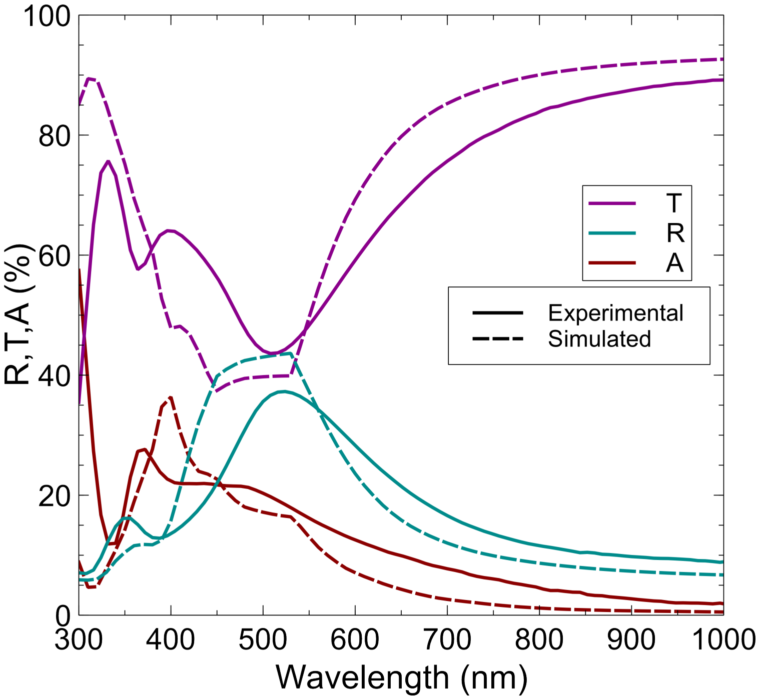

Figure 11.7: The reflection, transmission and absorption for the random array of particles introduced in chapter 6, the simulated data is calculated using the SM + Mie method.

coupling. This means that effects present due to the phase of the plane waves locally at the nanoparticle position will be neglected. However it also means that we do not need to worry about artificial periodic effects for particles having a fixed phase relationship between each other in the simulation (i.e. due to periodic boundary conditions) when no such relationship exists in reality.

Given these approximations we cannot expect that the results obtained using this method will converge towards the FEM method results, since they are simulating different physical systems. In order to justify the use of this method we instead reintroduce the experimental results from chapter 6. There we simulated the response of random particle arrays on a glass substrate. We now simulate the same situation using the SM + Mie theory. In chapter 6 we used a statistical distribution to obtain the correct resonance shape, however for the SM + Mie method we take only the mean value of the size distribution. The particle resonance is heavily influenced by the presence of the air/glass interface, however Mie theory is only valid for an isolated particle away from any interfaces. In order to bring these two factors together we simulate the particles in a thin film of $n = 1.3$ material in order to simulate the redshift induced by the glass substrate. Additionally we use the experimental coverage value of 18%. Figure 11.7 shows the comparison between the experimental values and the SM + Mie result. Although the SM + Mie result slightly overestimates the resonance intensity and does not show the broadening on the long wavelength region, many of the essential features are present in the simulated spectra. This gives us confidence that the SM + Mie method is able to semi-quantitatively predict the response of a random array of particles and can be used for the simulation of solar cells containing such particle arrays.

Chapter 12

Simulating Incoherent Light

We turn in this chapter away from abstract examples to more practical ones. One of the principle reasons for introducing coupled methods was in order to simulate solar cell devices with integrated nanoparticles and incoherent back reflectors. Therefore the first example will be a comparison of simulations for such a device using both FEM + SM and Mie + SM. Figure 12.1 shows a schematic image of the proposed solar cell device. The core-shell Ag-AlSb nanoparticles are integrated directly into the CIGSe layer close to the interface with the ITO back contact. The particle has a core radius of 50 nm and a shell radius of 60 nm meaning a 10 nm shell thickness. The layer thicknesses are the same as those given in chapter 8 for the incoherent device.

12.1 Comparing FEM to Mie+SM

Using the results of the previous section, we can predict the required number of substrate layer thicknesses to use for well converged results. We then simulate the solar cell device shown in figure 12.1. The FEM domain contains all the layers above the glass substrate and 200 nm of the glass substrate. PML boundary conditions are used along the z axis, hexagonal periodic boundary conditions are used in the x-y plane. The hexagonal domain width, i.e. the inter-particle spacing, was set to 180 nm providing a particle coverage of 18%. This is a typical value of coverage for the particle arrays presented in chapter 6.

The results from ten different substrate thicknesses equally spaced from 0.9 to 1.1 mm were used to obtain the absorption and losses found in fig. 12.2 part (a). The absorption in the CIGSe is generally high up until around 900 nm where it then begins to rapidly decrease. Although some noise is visible due to the finite number of substrate thicknesses

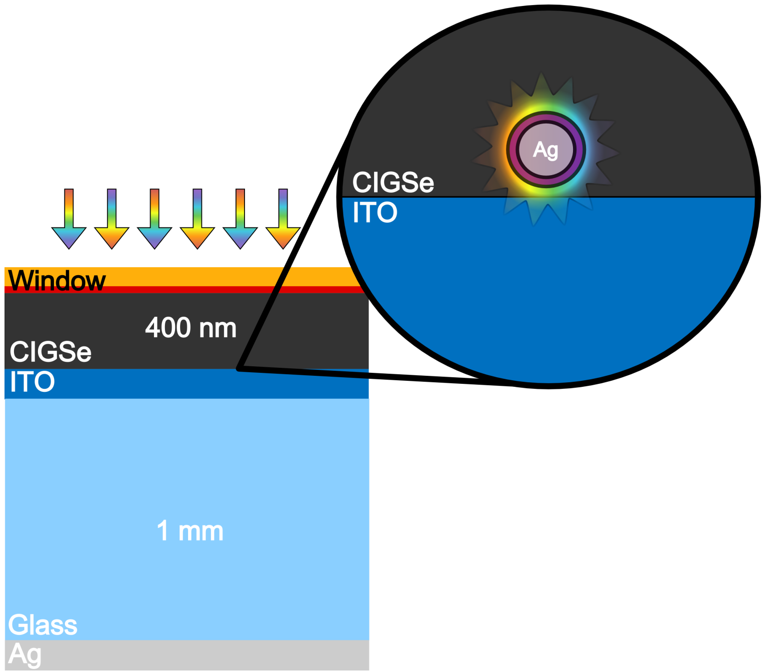

FIGURE 12.1: Schematic image of the ultra-thin solar cell with incoherent back reflector and integrated nanoparticles.

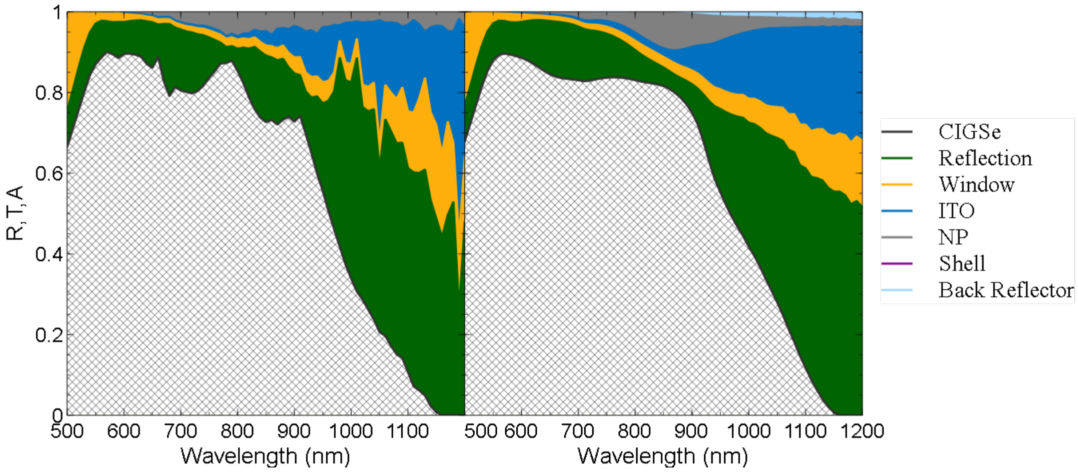

FIGURE 12.2: The reflection and absorption in a CIGSe solar cell with 400 nm thick absorbing layer. The back contact is a 200 nm ITO layer with an Ag back reflector separated by the 1 mm glass substrate. Ag/AlSb core/shell nanoparticles are integrated at the CIGSe/ITO interface. The device is shown schematically in fig. 12.1. Part (a) simulated with FEM, part (b) with the Mie+SM method.

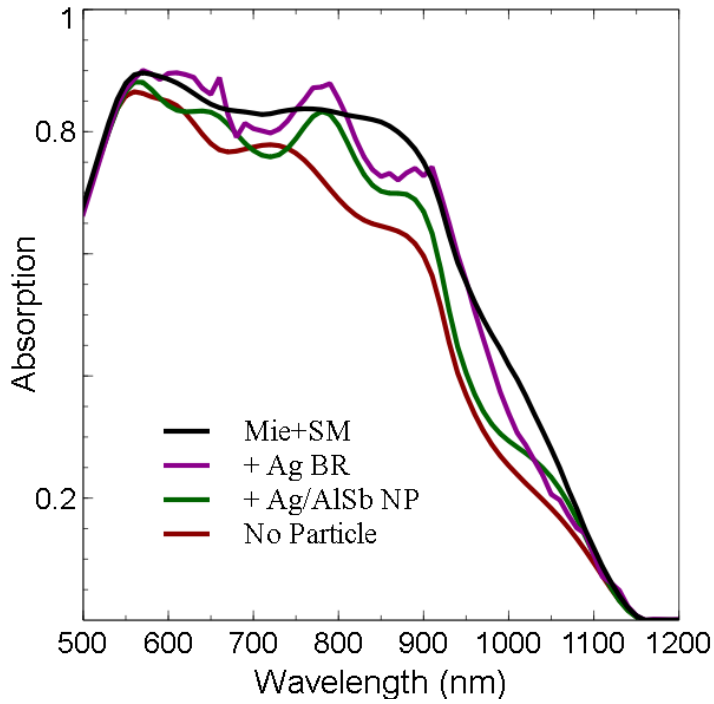

Figure 12.3: The absorption in the CIGSe layer of an ultra-thin solar cell device. The reference does not include nanoparticles or a back reflector. The Mie + SM simulation is performed on the full structure with nanoparticles and a back reflector.

used in the averaging process, the main quantity of interest is the CIGSe absorption which seems relatively free of noise. Additionally wavelength integration will tend to decrease the impact of the noise. In contrast part (b) which shows the same device simulated using the SM + Mie method proposed in this thesis is relatively free of noise. In general results for absorption and reflection appear to agree quite well with the results obtained using the FEM. The major difference is that the particle absorption at resonance is higher in the SM + Mie case but also the overall absorption enhancement due to the nanoparticle is larger. This is due to the fact that interference effects from light reflecting from the ITO interface are absent for the SM + Mie simulation, therefore at wavelengths between 700 and 850 nm where the particle is resonant, a large increase in absorption can be seen.

The differences in absorption between the FEM and Mie + SM simulations are more visible in fig. 12.2 where the absorption curves are directly compared. The curves shown in the image are the following,

1. The ultra-thin device with an ITO back contact and an infinite glass layer below, i.e. without a back reflector. Simulated using the SM method.
2. Same as in 1 but with the addition of integrated nanoparticles in the CIGSe layer. Simulated with FEM.

3. Same as in 2 but with an incoherent Ag back reflector. Simulated using FEM coupled to SM.

4. Same as in 3 but simulated using the SM + Mie coupled method.

Beginning with the device without back reflector or nanoparticles, the absorption curve shows only very slight peaks and troughs in the wavelength range between 600 and 800 nm. These are due to the slight amount of reflection at the CIGSe/ITO interface which will cause a weak Fabry-Perot resonance without the absorber layer. Due to a large fraction of light being transmitted into the infinite glass, the J$_{sc}$ for this device is only 23.59 mAcm^{-2}. When the nanoparticles are introduced, the reflection at this interface is increased significantly which increases the absorption in the CIGSe layer. The peaks and troughs also become more well defined especially around the particle resonance at 800 nm. The interaction between the particle resonance and the Fabry-Perot resonances causes two peaks at 750 nm and 850 nm to form. The effect of the nanoparticles is to increase the J_{sc} to 24.90 mAcm^{-2}. In chapter 10 we saw that combining the particles with the coherent back reflector leads to absorption spectra with a lot of different resonances, which was challenging to interpret. In this case the interpretation is much easier since the incoherent back reflector does not add any additional resonances, instead it simply increases the absorption in the CIGSe by about 5% at each wavelength compared to the case of no back reflector providing a J$_{sc}$ of 26.12 mAcm^{-2}

The result from the Mie + SM simulation does not show any of the peaks and troughs present in the FEM simulations as already stated. It can be seen that in the region 600 to 850 nm wavelength the Mie + SM result gives the average value of the FEM result if the peaks and troughs of the FEM result were removed. This gives us confidence in the Mie + SM method since it is showing the same overall enhancement just without the presence of the coherency peaks which may be the case in experimental spectra due to incoherencies introduced in e.g. the particle position. At wavelengths higher than this, the Mie + SM method shows a higher absorption in the CIGSe layer compare to the FEM. To understand why this is we need to consider the effect of coherency inside the device. Some effects of coherency are wavelength dependent, the peaks and troughs of a Fabry-Perot resonance for instance, provide an increased light interaction with the particle at some wavelengths and a decrease at others. However some effects are wavelength independent, the phase shift in reflections at the CIGSe/ITO interface will be largely independent of wavelength. This phase shift (which would be π for a perfect reflector) means that close to the interface destructive interference causes the light interaction with the particle to always be lower. This destructive interference is absent in the Mie + SM simulations due to the incoherent coupling meaning that it systematically overestimates the absorption in the CIGSe compared to the FEM. The

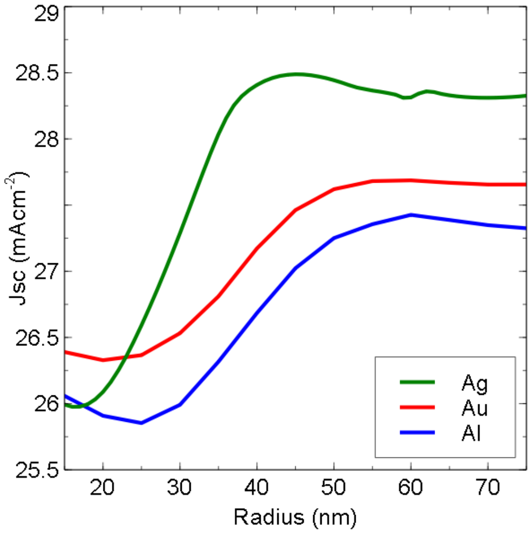

FIGURE 12.4: The J$_{sc}$ obtained from the Mie+SM method for a solar cell devices with incoherent back reflector and integrated core-shell nanoparticles. The core radius is varied by the values given on the x axis while the shell remains at a constant 10 nm thickness. The nanoparticles used are Ag/AlSb, Al/AlSb and Au/TiO$_2$. The Al core particle has an Al back reflector while the other two have an Ag back reflector.

overestimated absorption leads to a J$_{sc}$ of 26.81 which is slightly higher than the value predicted by the FEM.

Overall the SM + Mie theory gives results similar to the those produced using the FEM. Especially the resonance position of the particles is the same in both cases. The SM + Mie theory tends to overestimate the absorption in the CIGSe layer due to a lack of destructive interference close to a reflecting interface. Nevertheless, the advantage of the SM + Mie theory method is the extreme speed with which calculations can be performed. If we assume that the SM + Mie method systematically overestimates the absorption, an optimisation can still be performed, since the optimum value for the SM + Mie and for the FEM should still coincide.

12.2 Optimisation Using S Matrix + Mie Theory

Having developed the Mie+SM method and shown that it agrees fairly well with the FEM, we move to applying the method to optimising the incoherent solar cell device structure. Firstly we consider the device from the previous section with core-shell particles integrated into the absorber layer with an additional incoherent back reflector and try to answer the question of what the optimal core radius should be. This can be performed for different materials and here we revisit the materials introduced in chapter 4, namely Ag, Al and Au. The Ag device with an AlSb shell has already been discussed. Since an Al particle will need a strong redshift to bring the resonance to the optical regime, we choose again the AlSb shell since it is a high refractive index shell. The Au core on the other hand has a relatively long wavelength resonance to begin with, therefore we choose a lower refractive index shell in TiO_2 which will keep the resonance within the spectral region of the CIGSe. We vary the particle radius from 15 to 75 nm while keeping the shell thickness a constant 10 nm. For each case a coverage of 10% is used. The value was chosen since it means there should be no near field interactions between particles which would invalidate the independent particle approximation used in the SM + Mie method.

The same trend can be seen for each of the different materials, the larger particles provide a higher J_{sc} which saturates for larger radii. Apart from that the Ag outperforms the other two materials for larger radii. The reason that the J_{sc} increases for larger particles is that the resonance is redshifted to longer wavelengths. Due to the lower absorption at these wavelengths the particles can have a higher impact, also the particles interact less with the shorter wavelength (600 - 700 nm) light, which is good since the reflection from the particles in this wavelength region can reduce the path length of light in the device due to the fact that the particles are actually in the absorbing layer, assuming that the angular scattering is low. Therefore it is better for the light to be reflected by the incoherent back reflector since it is separated from the absorber layer meaning it does not reduce the path length of light.

As the size increases from 15 nm the total J_{sc} rapidly rises as the nanoparticle resonance redshifts into the region where the solar cell is poorly absorbing. This effect saturates around a value of 45 nm radius for Ag and 60 nm for Au and Al, after which the resonance becomes very broad and will slowly decrease in effectiveness for larger radii. At 45 nm radius the Ag particle with a 10 nm thickness AlSb shell in a medium of non-absorbing CIGSe has a peak dipole resonance wavelength of 1000 nm and a quadrupolar resonance at 766 nm. These two resonances both contribute to boosting the absorption of the ultra-thin solar cell.

Once the optimum resonance position has been found by changing the particle size, a further step is to try and optimise the particle coverage. Particles with a lower scattering may benefit from having a higher coverage in order to maximise their scattering.

Figure 12.5 shows the J_{sc} obtained for different values of particle coverage. The particle core sizes are taken from the maximum value found in 12.4, namely 45 nm for the Ag particle and 60 nm for the Au and Al particles. All three particle types show an increase in the J_{sc} for increasing particle coverage before saturating. The Ag and Au cases saturate quicker compared to the case of the Al particles. This is due to the strong absorption band in Al at 800 nm which means the scattering does not increase as fast relative to the parasitic particle absorption compared to the low loss Ag and Au. Again

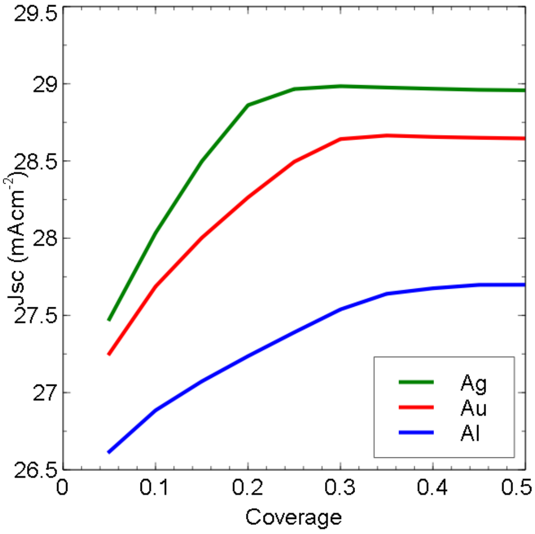

FIGURE 12.5: The J_{sc} obtained from the Mie+SM method for a solar cell device with an incoherent back reflector and integrated core-shell nanoparticles. The particle coverage is varied by the values given on the x axis. The particle core radii are taken from the maximum values found in 12.4 with a 10 nm shell thickness. The nanoparticles used are Ag/AlSb, Al/AlSb and Au/TiO_2. The Al core particle has an Al back reflector while the other two have an Ag back reflector.

Ag shows the best performance which justifies the focus on this material throughout the thesis.

Questions can be raised regarding the accuracy of the results for such high values of coverage. The Mie solution for an isolated particle is no longer valid for the case of strong particle interactions which may be present when particles have a coverage higher than 30%. In fact the saturation of J_{sc} is due to this fact. Although the particle interactions are not modeled using this method, the fact that the product of the normalised extinction cross section and the coverage cannot exceed unity is included. This means that as particles come closer together, the envelopes in which they collect light start to overlap meaning that particles cannot interact with as much light as when they are totally isolated. This effect stops the scattering from rising as the coverage keeps increasing.

The optimum device found for Ag particles reaches a J_{sc} of 28.98 mAcm^{-2} for a 60 nm Ag core radius at 30% particle coverage. Although we cannot verify that this is the maximum value using the FEM since it would be too computationally expensive, we can simulate this exact configuration using the FEM in order to compare the J_{sc} obtained.

In general other parameters may also be optimised. The coverage, particle size and material, layer thickness and material of other layers can also be optimised. The method presented here, while only being applicable in the limit of low coverage, provides a very quick method of obtaining the absorption for photovoltaics with integrated nanoparticles. It should be used in conjunction with experimental work in order to quickly appraise device designs, thus greatly reducing the experimental effort required to obtain a large absorption enhancement for ultra-thin photovoltaics.

In conclusion we present the J_{sc} for some of the most promising devices simulated. The most optimal structure was the one shown in the current chapter, that of core-shell particles embedded into the absorbing layer with an additional Ag back reflector. The reason this provides the highest absorption enhancement is that the wavelength independent absorption enhancement provided by the incoherent back reflector does not provide any strong coherency phase oscillations inside the absorbing layer where the nanoparticle is situated, which cause the nanoparticle to have a reduced intensity meaning that less light will be scattered by the nanoparticle.

Device	J_{sc} (mAcm^{-2}
standard thin film	31.16
ultra-thin film (400 nm) Mo B.C.	24.63
ultra-thin film (400 nm) Mo B.C. + Ag/AlSb Core/Shell NP	24.91
ultra-thin film (400 nm) ITO B.C. + 860 nm SiO_2 + Ag B.R.	26.84
ultra-thin film (400 nm) ITO B.C. + 860 nm SiO_2 + Ag B.R. + Ag/AlSb Core/Shell NP	26.34
ultra-thin film (400 nm) ITO B.C. + 1 mm SiO_2 + Ag B.R.	26.81
ultra-thin film (400 nm) ITO B.C. + 1 mm SiO_2 + Ag B.R. + Ag/AlSb Core/Shell NP	28.98

TABLE 12.1: The J_{sc} of various device designs presented in this work.

Chapter 13

Conclusion

The aim of this thesis was to assess plasmonics as a technology for improving solar cells via simulations. Despite the focus on technology, the work cannot be categorised as engineering in which we seek only to find the best possible device, but rather as a work of science, in which we seek to understand why some devices fail while others succeed. To this end a lot of time has been spent modelling and understanding the fundamental building blocks that go into a plasmonically enhanced solar cell. In fact plasmonic integration only begins in chapter 10. However the work that occurred previous to this was crucial to the process of understanding.

Chapters 3 and 4 focus on the fundamental questions of plasmonics. Firstly reviewing types of dielectric function, we can associate plasmonic resonances with metallic permittivities. From this starting point we move through bulk and surface plasmons to the most technologically relevant localised surface plasmon (LSPR). The LSPR can be analysed using the Mie theory framework introduced in chapter 3. The first question to be addressed is that of which metals can be used for plasmonics, therefore we weigh the relative strengths and weaknesses of commonly employed plasmonic metals. For the application of chalcopyrite solar cells, Ag is shown to be the optimal material since it has a plasmonic resonance in the optical region and low optical losses. After the choice of material has been made, the two further levers available in order to control the LSPR are the surrounding material refractive index and particle radius. Increases in both of these factors cause a redshift in the LSPR, but for very different reasons: damping charges for the surrounding material and retardation effects for the particle radius. The main contribution of these chapters (apart from the mathematical framework revisited in chapter 12) is the study of metallic particles with dielectric shells. Although these systems have already seen use in the literature, the optical optimisation of the complete three material system of metal core/dielectric shell/dielectric outer medium system has seldom been performed. We present results which support the position that the choice of shell material, even for thin shells, is of paramount importance to the device. The interplay between the modes of the dielectric shell and the plasmonic core means that if the shell has a higher refractive index than the surrounding medium, the plasmonic activity of the core will be enhanced, while the opposite is true if the shell has a lower refractive index compared to the outer medium. Since plasmonic particles typically need a shell material in order to electrically and chemically isolate them from the surrounding optoelectronic device, this is a key insight for device optimisation which has not been presented in a clear manner in the literature.

Chapters 5 and 6 move from the idealised case of the single spherical particle to more general cases. Firstly identifying the effects due to distortions in the shape of spherical particles. Moving onto the interaction between two particles and finally simulating experimentally fabricated arrays of nanoparticles. The most important contribution in this chapter is the novel approach to simulating arrays of random nanoparticles. Due to the presence of a size distribution it can be expensive to construct a simulation large enough to accurately reflect this distribution. We instead took the approach of simulating isolated particles and averaging the response of different particles using the experimentally obtained size distribution. This proved to be successful for reproducing the resonances of the particle array when assuming a certain particle shape, as long as substrate corrections were included.

In order to extend these results the shape of the particles should be obtained via surface topology measurements, this would allow the results to be truly predictive instead of fitting the particle shape to the resonance. Furthermore the effect of light trapping in the substrate should be included in a more rigorous manner, this could be achieved by iterative coupling of the particle simulations to a layered media simulation for the substrate. This would mean extending the coupling to include isolated FEM simulations since it is currently only available for FEM simulations with periodic boundary conditions in the x-y plane.

Chapters 7 and 8 introduce the ultra-thin film device structure and the S matrix technique for modelling layered media. The necessity of a different back contact for the ultra-thin device is demonstrated due to poor reflection from Mo even in the presence of nanoparticles. This leads to replacing the back contact with a transparent conducting oxide with a back reflector behind the back contact. The distance between back contact and back reflector could be optimised in order to increase the absorption in the absorber layer. This is the first example of an optically optimised flat layer ultra-thin CIGSe device with a transparent back contact and extra back reflector.

The step of integrating plasmonic nanoparticles into the solar cells is reached in chapters 9 and 10. It was shown that the resonance of particles at an interface may be slightly detrimental due to a lower field intensity close to the interface due to the interference between incident and reflected light. Different positions for integration inside the device with a transparent contact were compared, with the result that integration directly within the absorbing layer offers the highest overall enhancement, due to better light trapping and utilisation of near field effects.

The final set of chapters 11 and 12 is the culmination of the thesis, bringing together the different parts that have previously been presented. First the general framework for coupling between different kinds of simulations in an iterative manner is established. This framework is then used to extend the finite element method used in chapters 6 and 10 to incoherent layers. Furthermore the coupling of Mie theory first introduced in chapter 3 with the scattering matrix method from chapter 7 is presented in order to reach qualitatively similar results to the more rigorous approach in a fraction of the time. This novel approach can be used to quickly estimate the impact of plasmonic integration to solar cell devices which is hugely important given the vast number of parameters which need to be optimised for successful absorption enhancement.

In order to extend the work presented in these chapters we recommend extending the coupled approach in order to take into account light coherency effects inside the solar cell which proved to be the major difference between the FEM and Mie theory + S matrix results. Ultimately the approaches presented here for modelling solar cells with integrated plasmonics must also be verified by experiements, which means fabricating the devices proposed.

Chapter 14

Publications List

Here I present a summary of publications in which I have published my work.

1. P. Manley, S. Burger, F. Schmidt, M. Schmid, *Design principles for plasmonic nanoparticle devices*, in “Progress in Nonlinear Nano-Optics”, Editor R. Grunwald, Springer (2015)
2. M. Schmid, P. Manley, *Enhancing solar cell efficiency by lenses on the nano- and microscale*, Proc. SPIE, Next Generation Technologies for Solar Energy Conversion V 9178, 91780K (2014)
3. M. Schmid, P. Manley, *Nano- and microlenses as concepts for enhanced performance of solar cells*, Journal of Photonics for Energy, 5, 057003 (2015)
4. P. Manley, F. Schmidt, M. Schmid, *Light Extraction from Plasmonic Particles with Dielectric Shells and Overcoatings*, Proceedings of 2013 OSA Congress Renewable Energy and the Environment, Optics Info Base (2013)
5. M. Schmid, P. Andrae, P. Manley, *Plasmonic and photonic scattering and near fields of nanoparticles*, Nanoscale Research Letters, 9, 50 (2014)
6. G. Yin, A. Steigert, P. Andrä, M. Goebelt, M. Latzel, P. Manley, I. Lauermann, S. Christiansen, M. Schmid, *Integration of plasmonic Ag nanoparticles as back reflector in ultra-thin Cu(In,Ga)Se2 solar cells*, Applied Surface Science, 355, 800 (2015)
7. P. Manley, F. Schmidt, M. Schmid, *An efficient method for calculating the absorption enhancement in solar cells with integrated plasmonic and photonic nanoparticles*, 9th International Congress on Advanced Electromagnetic Materials in Microwaves and Optics - Metamaterials, (2015)

8. G. Yin, P. Manley, M. Schmid, *Influence of substrate and its temperature on the optical constants of CuIn1-xGaxSe2 thin films*, Journal of Physics D: Applied Physics, 47, 135101 (2014)

9. P. Manley, G. Yin, M. Schmid, *A method for calculating the complex refractive index of inhomogeneous thin films*, Journal of Physics D: Applied Physics, 47, 205301 (2014)

14.1 Design Principles for Plasmonic Nanoparticle Devices

Many of the results in chapters 3-6 were presented in a contribution to the book *Progress in Nonlinear Nano-Optics*, which despite the name, also included results from linear nano-plasmonics. The contribution focuses on the finite element method and uses this to explain a lot of fundamental physical concepts involved in plasmonics, in the context of controlling the plasmonic resonance for optical applications, in particular absorption enhancement in ultra-thin film solar cells. Figure 14.1 shows the spectral absorption profile for both a standard thin film and an ultra-thin film solar cell. The thin film has a high absorption (above 80%) for most of the spectral region from 300 to 1100 nm wavelength. The ultra-thin film has a much reduced absorption, particularly at longer wavelengths due to the reduced path length of light in the absorbing layer. The

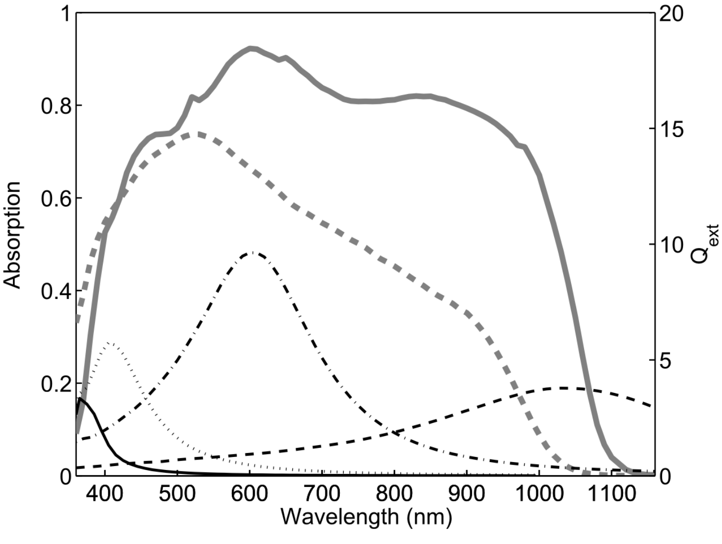

FIGURE 14.1: The absorption curves for a solar cell with CIGSe thickness 2μm (solid grey curve) and 450 nm (dashed grey line). Also shown are the normalised scattering cross sections for four different Ag nanoparticles: a 60 nm diameter particle in air (solid black curve), a 100 nm diameter particle in air (dotted black line), a prolate ellipsoid with axis lengths 200/100/100 nm in air (dot-dash black line) and an oblate ellipsoid with axis lengths 200/200/100 at an air/Al:ZnO surface (dashed black line). Left hand axis is for the absorption curves while the right hand axis is for the cross sections.

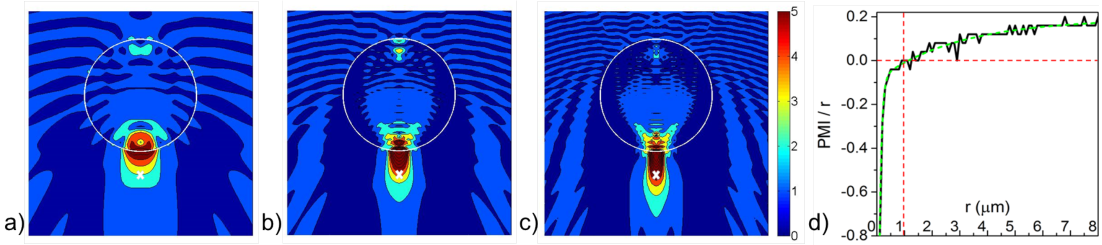

FIGURE 14.2: The normalised electric field distribution for an SiO_2 particle with radius values of a) 1 μm, b) 2 μm and c) 3 μm at a wavelength of 700 nm. The shape of the sphere is marked for clarity as well as the back focal length calculated from geometrical optics (cross); d) gives the point of maximum intensity with respect to the sphere's rear surface normalised to its radius and plotted as a function of the radius.

same figure shows the normalised scattering cross sections of various Ag nanoparticles. In order for the plasmonic resonance of the particle to match the spectral region in which it is needed, we should consider the geometrical and material properties of the nanoparticle and surrounding. The initial small nanoparticle with only 60 nm diameter is first increased to a 100 nm diameter in order to show the redshifting effect induced by this. By replacing this particle with an ellipsoidal particle which is elongated parallel to the polarisation such that the axis length is now 200 nm, the resonance is further redshifted and increases in intensity. Considering now the application to a front side scatterer, we take an oblate ellipsoidal particle with axis lengths of 200 nm parallel to the electric and magnetic polarisation and 100 nm parallel to the wave vector. This particle is then placed at an inteface between air and Al:ZnO to act as an anti-reflection layer with added light trapping properties. This causes the resonance to be further redshifted due to the higher index of Al:ZnO compared to air. In this image we can see the seeds of the coupled method presented in chapter 12 where a layer stack simulation is combined with Mie theory simulations to rapidly predict the absorption enhancement due to light scattering from integrated nanoparticles.

14.2 Enhancing Solar Cell Efficiency by Lenses on the Nano- and Microscale

Previous work had already described the major optical differences between metallic and dielectric nanoparticles, here we extend this comparison to larger dielectric spheres which may be used as micro-lenses. Since the lenses have a size which is larger than the wavelength in the optical region, we look at the comparison to geometrical optics which is valid for objects much larger than the wavelength. Figure 14.2 shows the near field distribution for three different dielectric sphere radii. The field above the sphere is clearly a plane wave distorted due to back scattering from the sphere. The width of the peaks and troughs of the plane wave becomes smaller in each image because the wavelength remains constant while the image is effectively zoomed out to make the particle have equal size in each image. Below the particle the field distribution is drastically different, the light is converted to a high intensity beam. for the smallest sphere the maximum intensity point of the beam resides at the particle boundary. For smaller particles (near field not shown) this point shifts inside the particle while for larger particles it shifts to outside the particle as shown in part (d) where the point of maximum intensity (PMI) normalised to the particle radius is shown as a function of the particle radius. In all of the images there is a deviation between the geometrical optics focal point and the point of maximum intensity. In chapter 10 of the current work we discussed the possibilities for plasmonic nanoparticle integration, ruling out front side integration due to strong losses in metals for shorter wavelengths. The work from this paper shows that dielectric particles may well offer an alternative to plasmonic particles with the localised forward scattering shown in fig. 14.2.

14.3 Nano- and Microlenses as Concepts for Enhanced Performance of Solar Cells

The concept of the dielectric nano- or microparticle as a lense for solar applications was further explored in this paper. The major difference compared to macroscopic lenses is exemplified in fig. 14.3 where the Poynting flux lines are shown for a plane wave incident onto a microparticle lense on top of a nano solar cell. The flux lines show the diffraction of light around the particle, smaller particles can diffract light which is not directly incident onto the particle. This is equivalent to having a normalised extinction cross section (introduced in chapter 4) larger than unity. As the particle becomes larger the effect lessens; in the macroscopic limit, only light which is directly incident to the particle will be diffracted. The trade-off then becomes: the larger sphere leads to a higher intensity inside the solar cell, whereas the smaller sphere provides a lower intensity but is able to guide light from a larger area compared to its size. This might mean that an array of smaller particles is able to achieve the same overall focusing effect as the larger spheres but at a reduced weight. The relationship between a particle's normalised extinction cross section and the envelope of light with which that particle interacts was a crucial part of the Mie + SM model presented in chapter 12. The model assumes that the particles are low enough concentration that these envelopes do not overlap, allowing the particles to be considered isolated.

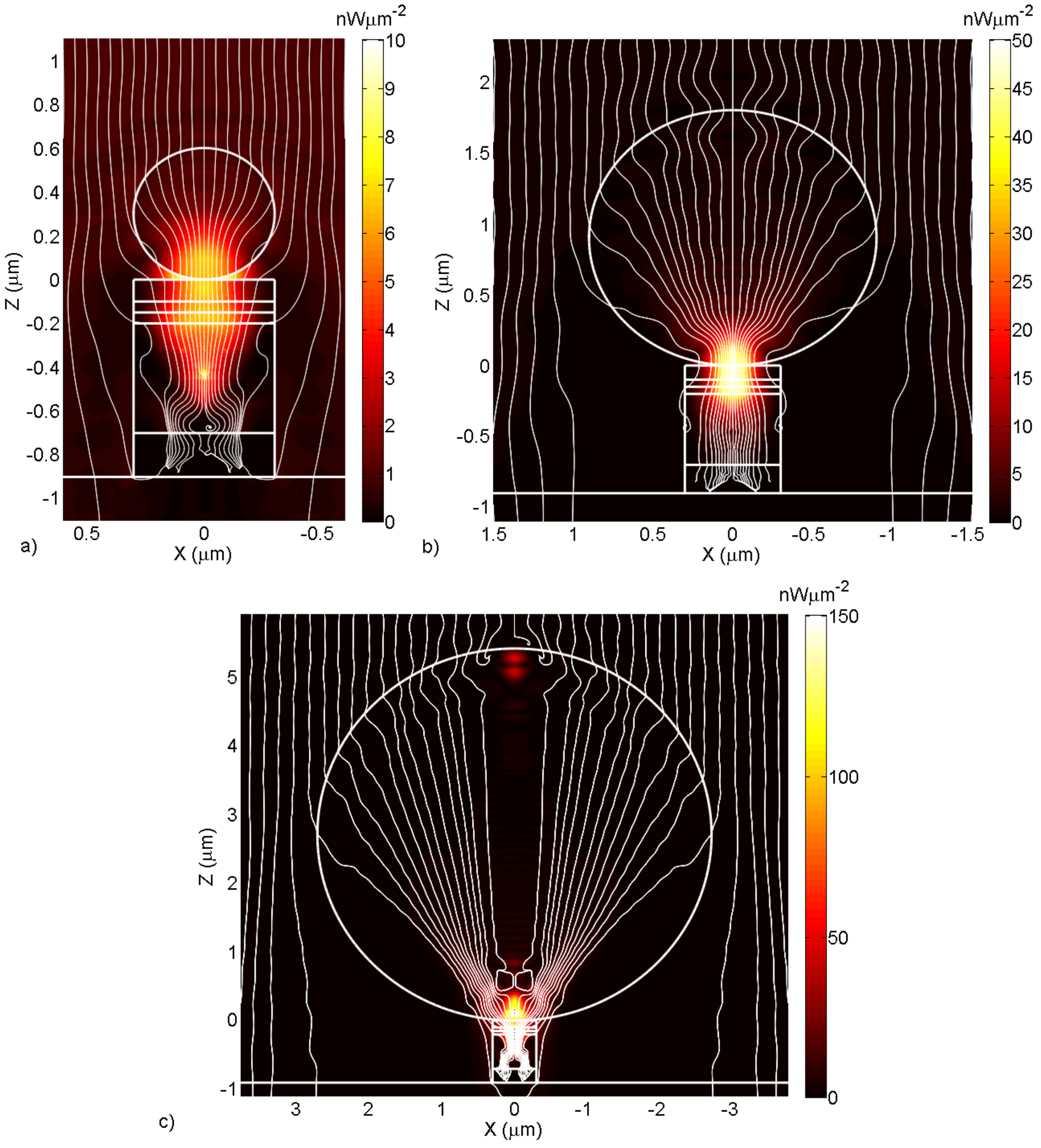

FIGURE 14.3: Heat map of the Poynting flux density for a plane wave incident to an SiO_2 sphere on top of a micro chalcopyrite solar cell. White lines show the geometrical boundaries of the particle and solar cell layers but also the Poynting flux lines. The diameters of the particles are a) 0.5 μm, b) 1.5 μm and c) 3 μm, the solar cell diameter is kept at 0.5 μm for each case.

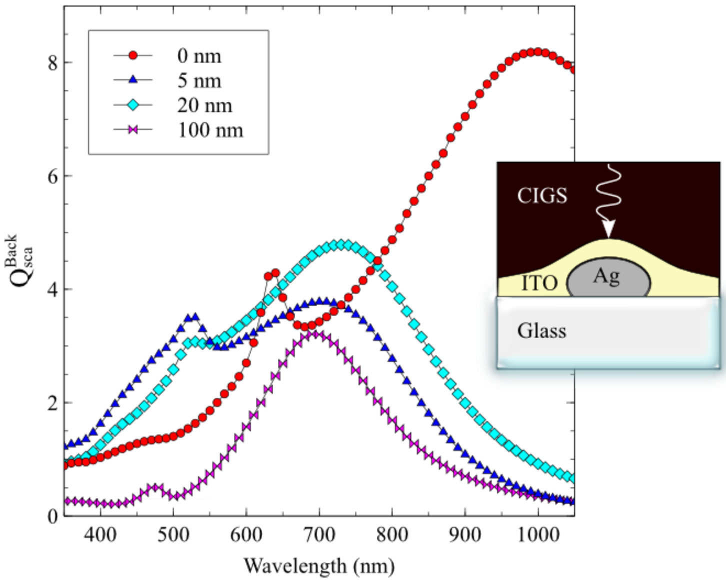

FIGURE 14.4: The normalised back scattering cross section for an Ag nanoparticle at a CIGSe/glass interface with different thicknesses of ITO overcoating (as shown in the inset). The thicknesses of the ITO overcoats are 0 nm (circles), 5 nm (triangles), 20 nm (diamonds) and 100 nm (ties). The wavelength range shown is the operational wavelength of a CIGSe solar cell.

14.4 Light Extraction from Plasmonic Particles with Dielectric Shells and Overcoatings

The results presented at the end of chapter 4 surrounding core-shell particles and their integration into chalcopyrite solar cells went towards this publication. In particular the specific near field decay of the dipole mode for different shell/surrounding combinations was investigated. This lead towards the explanation for why a shell with a higher refractive index than the surrounding medium is beneficial for plasmonics which is presented in chapter 4. Additionally overcoatings were simulated as a possible replacement for core-shell particles as shown in fig. 14.4. It was found that coherency effects could be utilised to increase the back reflection of nanoparticles for very thin ITO layers. This concept was revisited in chapter 10 where nanoparticle integration inside the ITO layer is simulated.

14.5 Plasmonic and Photonic Scattering and Near Fields of Nanoparticles

Not only plasmonic particles but also dielectric particles may be useful for light management in solar cells. In order to understand the fundamental differences between the two, both kinds of particles were investigated theoretically in this work. The theoretical

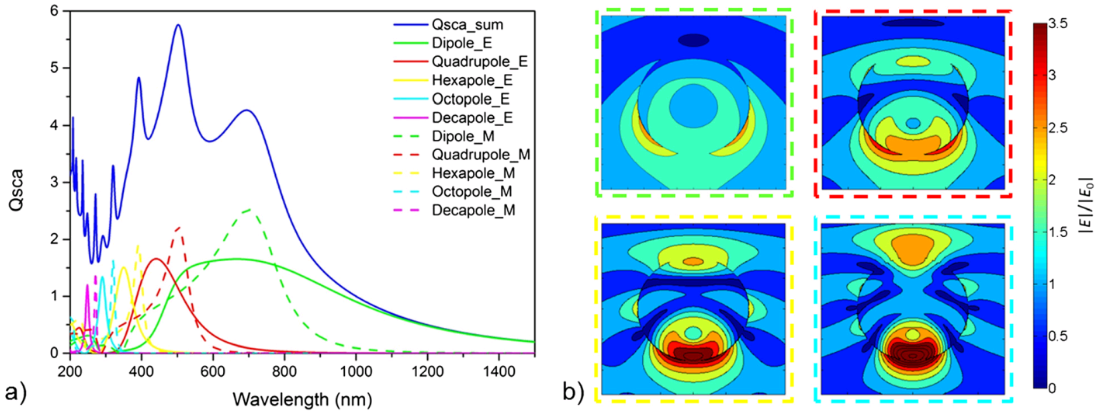

FIGURE 14.5: Part (a) shows the normalised scattering cross section for a radius 170 nm dielectric particle with a constant refractive index of 2 in air. The scattering is decomposed into the component multipole orders. Part (b) shows the near fields at the peak of the resonances in part (a) given by the same line markings.

frameworks of Mie theory (chapter 3) and the FEM (chapter 5) were both used, Mie theory being able to decompose the scattering in different multipole orders while the FEM being able to simulate particles placed at an interface. This modal decomposition is shown in fig. 14.5 for a radius 170 nm dielectric particle with a constant refractive index of 2. The near fields show a mix of electric type behaviour, which has been presented in chapter 6 but also magnetic type behaviour which is unique to dielectric particles. The results in chapter 6 detailing the angular scattering distribution for plasmonic particles at interfaces with different refractive indices were widened in this work to include dielectric particles at the same interfaces. Dielectric particles at a planar interface were shown to have similar or even better high angle scattering, but with a reduced scattering cross section compared to plasmonic particles. Semiconducting particles were also investigated, however for typical semiconductors the free carrier response is in the deep infrared, meaning that the plasmonic type response is not able to be exploited in the visible regime. Highly doped semiconductors may offer a way to combine dielectric and plasmonic scattering.

14.6 Integration of Plasmonic Ag Nanoparticles as Back Reflector in Ultra-Thin CIGSe Solar Cells

In order to verify plasmonics as an optical concept for CIGSe solar cells we fabricate devices with integrated plasmonic nanoparticles. Figure 14.6 (a) shows the device in question, an ultra-thin film CIGSe solar cell which will have plasmonic Ag nanoparticles integrated at the Al_2O_3/glass interface. Part (b) then compares the absorption in the CIGSe layer and in the solar cell overall with and without the particles from simulations

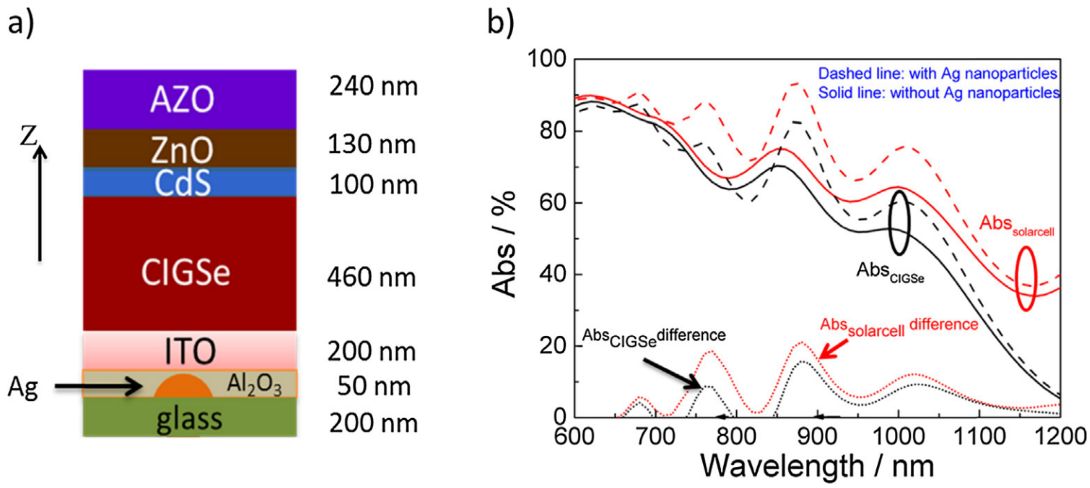

FIGURE 14.6: Part a) shows the device structure simulated with a hemispherical Ag nanoparticle in a hexagonal lattice. Part b) shows the absorption in the CIGSe layer and in the solar cell overall, for the two cases of with integrated nanoparticles and without.

based on the work in this thesis. The wavelength dependent increase in absorption has been shown in chapter 10 to be caused by the interaction between Fabry-Perot resonances inside the layered stack and the nanoparticles. The integration of the nanoparticles was able to show an absorption increase, in this case it did not translate to an increase in device performance due to poor electric properties. It is not suspected that this comes from the diffusion of the particles since measurements of the chemical composition of the CIGSe surface after deposition do not indicate the presence of Ag. However the patterning of the layers above the particles is believed to have caused the poor electric properties. This was a successful demonstration of the optical benefits of plasmonic nanoparticles, but it also emphasises the need for complete optimisation of the entire device not just the optical properties.

14.7 An Efficient Method for Calculating the Absorption Enhancement in Solar Cells with Integrated Plasmonic and Photonic Nanoparticles

This paper presents the coupling method which combines layer stack simulations with Mie theory which was detailed in chapter 12. Figure 14.7 part (a) shows a schematic image of the coupling method. Light incident to the layer stack is first incorporated into an S matrix simulation that handles the propagation of light up until the nanoparticles. The transmission from this stack is then handed to a Mie theory simulation which determines how much light is absorbed by the particle and also the angular distribution

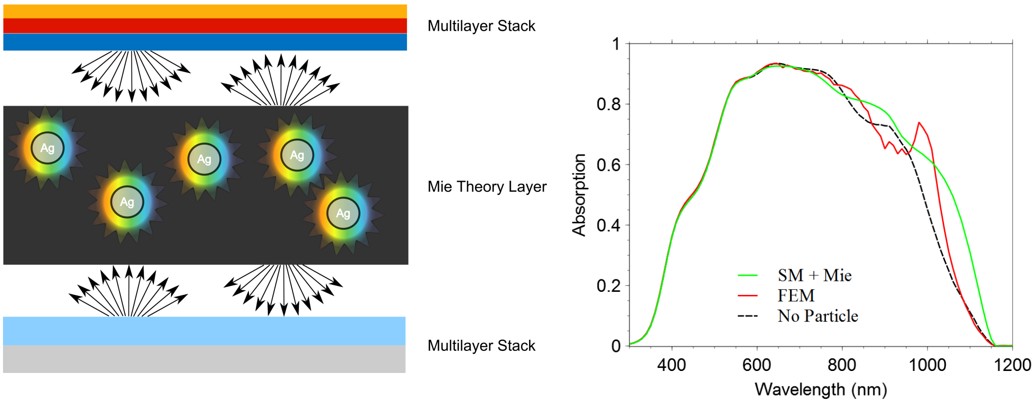

(A) (B)

FIGURE 14.7: (a) Schematic of the simulation procedure for coupling together S matrix and Mie theory calculations. (b) Simulated absorption in the chalcopyrite layer of a solar cell. The reference absorption without integrated nanoparticles is calculated via the S matrix. The plasmonically enhanced absorption is calculated via either the finite element method or the coupled Mie theory + S matrix method.

of light scattered by the particle. This then acts as an input for S matrix simulations both above and below the nanoparticles. This process is iterated until all the light has been reflected or absorbed inside the solar cell. Part (b) shows results obtained using this method compared to results obtained using the finite element method. Both of these methods predict a slight absorption enhancement compared to the reference without nanoparticles (but still having an incoherent back reflector). The Mie theory + SM method predicts a larger absorption enhancement likely due to the incoherent coupling between simulations used. This may accurately reflect the enhancement achieved by particles with a range of z center positions, which could be achieved also by particles of different sizes. Experimental data is needed to confirm the validity of each approach.

14.8 Influence of Substrate and its Temperature on the Optical Constants of CIGSe Thin Films

The method presented in appendix A for obtaining the refractive index of layers in a multilayer stack via reflection and transmission measurements was used in this work. The ability to obtain the refractive index of a material inside the layer stack using a destructive process was invaluable to investigating the difference compared to the same material outside of the layer stack. Figure 14.8 highlights the kind of difference that this can make for a CIGSe layer where the n and k values have been measured for different substrates. The deposition on ITO produces films with a higher absorption (k value) and associated slightly different n values. Being able to obtain accurate refractive index values for use in the simulations containing layered media in chapters 8,10 and 12 was

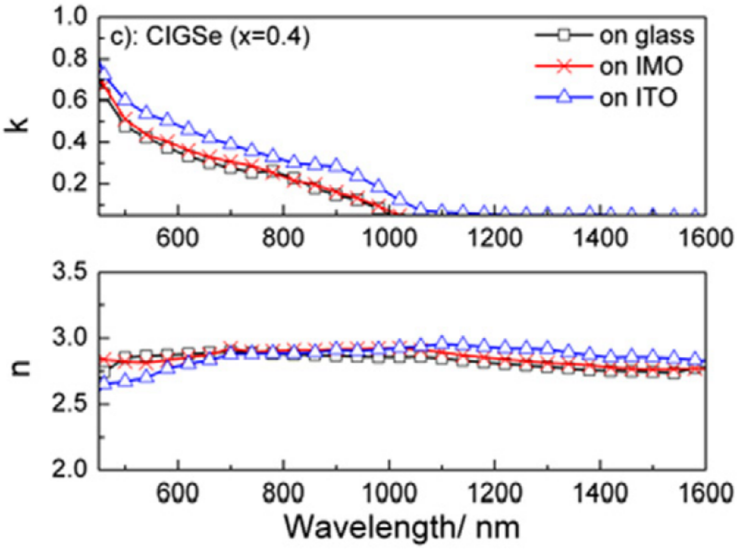

FIGURE 14.8: The n and k values for a CIGSe film deposited on three different substrates.

crucial to making these simulations realistic. Although this paper is mainly experimental in nature, my main contribution was the analysis tool used to obtain the refractive index results.

14.9 A Method for Calculating the Complex Refractive Index of Inhomogeneous Thin Films

This work builds on the results of the previous publication on refractive index determination. Here we extend the previous methods for dealing with rough surfaces, which were already common in the literature, to dealing with voids inside of a thin film. The model relies on statistical data gathered from SEM images of the surface of the sample in order to generate a 3D distribution of voids inside the layer. Figure 14.9 shows the result of applying image analysis to a SEM image of the voids: a 3D distribution which is statistically similar to the original SEM image. The 3D distribution is used to generate a series of layer stack simulations which, if combined with the correct weightings, correctly describe the propagation of the specular beam inside the layer. This can be used to determine the homogeneous refractive index of an inhomogeneous material. While no inhomogeneous materials were used in this thesis, the use of many different materials has been proposed. Typically new materials are difficult to prepare in a homogeneous film and extracting the homogeneous refractive index from an inhomogeneous film is extremely useful. This is true for materials such as the chalcopyrite system discussed in chapter 7 but also the popular Perovskite material which has shown incredible growth

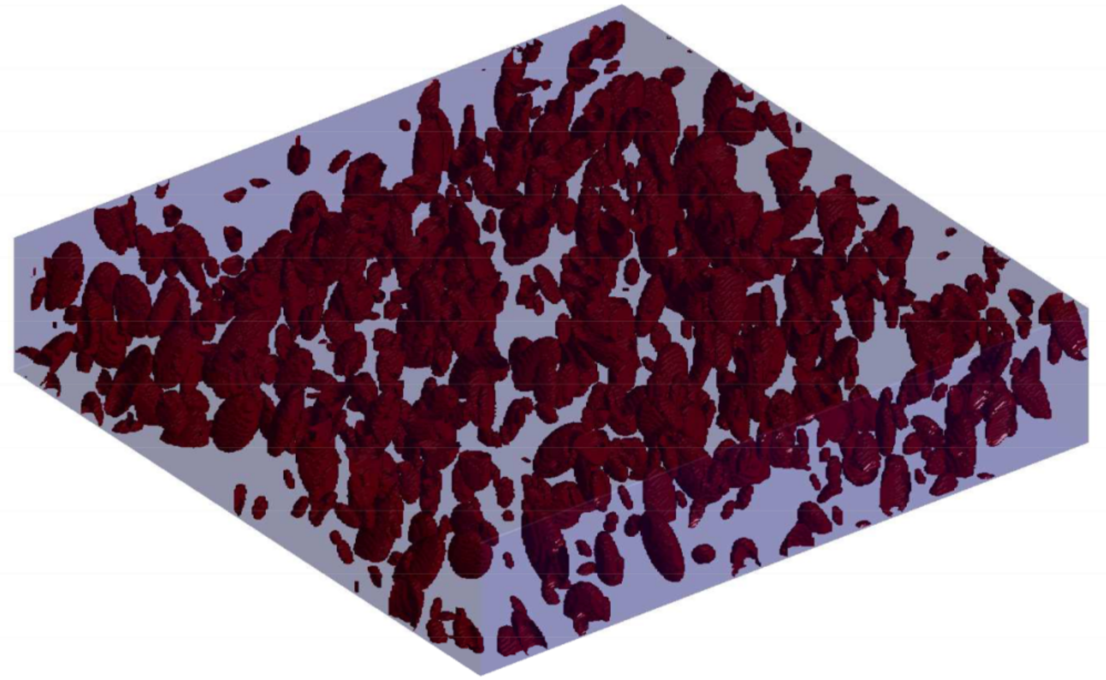

Figure 14.9: The 3D distribution of voids inside a thin film layer. The red objects represent the voids while the translucent bounding box is the thin film.

in solar cell research in recent years. A more detailed explanation of the method is given in appendix A.

Chapter 15

Curriculum Vitae

For reasons of data protection, the Curriculum vitae is not published in the online version

Appendix A

Modelling the Refractive Index of Materials

All the simulations presented in this work require the refractive index or permittivity of the materials contained inside the simulation to be known. Since all our simulations use the time harmonic ansatz, meaning that we solve in the frequency domain instead of the time domain, we do not necessarily need an analytical model for the permittivity which would be necessary for time domain simulations. This is very beneficial from the point of view of obtaining simulations which come as close as possible to reality. That is because we can use experimental data to obtain the permittivity of materials directly without fitting a specific model to the data. This is important because many of the most important materials used in this work, such as Ag and CIGSe, have very complicated optical responses. Finding an analytical model which is able to represent the response for these materials could be the subject of an entire thesis. In this appendix we present the methods by which the permittivity can be extracted from experimental data, as well as the innovations developed in order to obtain the permittivity in non-ideal samples. Although the permittivity and complex refractive index are equivalent, we will work with the refractive index during this appendix.

A.1 Obtaining the Refractive Index of a Thin Film

In order to obtain the complex refractive index of a thin film, we can compare the experimentally obtained reflection and transmission of the film to simulated values. The scattering matrix method presented in chapter 7 allows the propagation of light through a thin film stack to be simulated if the refractive indices of the constituent layers are already known. If a single thin film is simulated, the only inputs to the simulation would

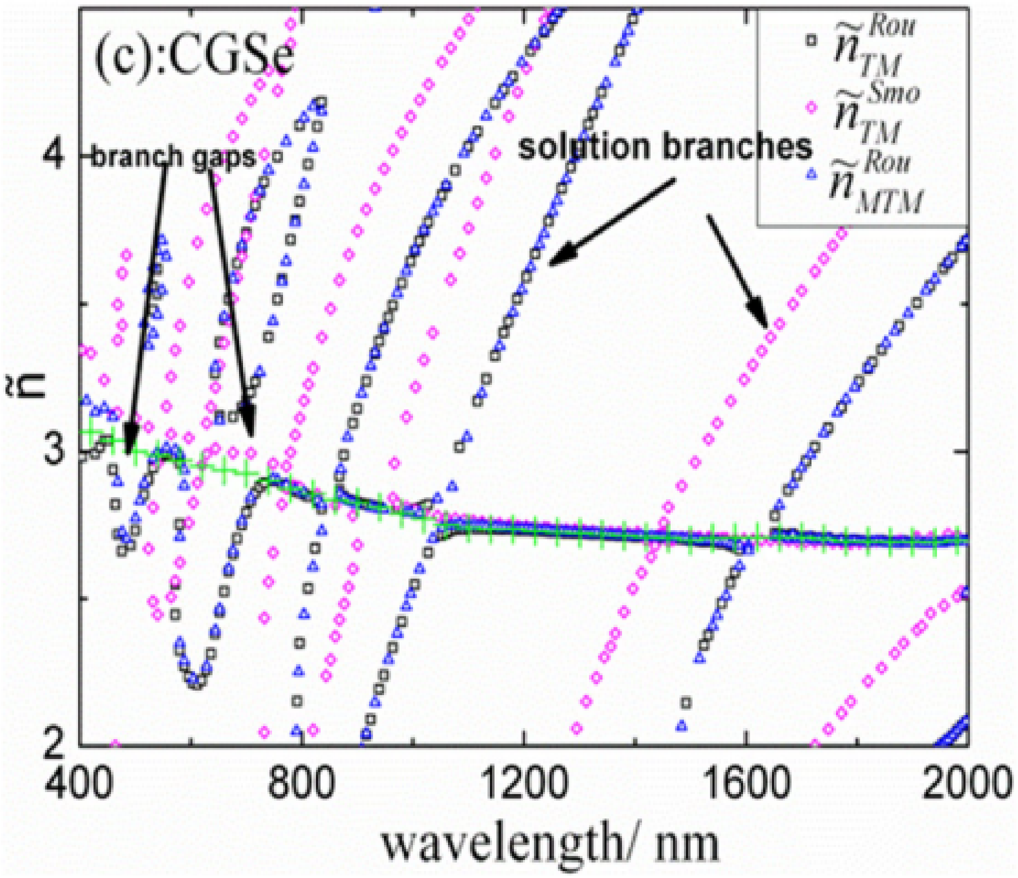

FIGURE A.1: The multiple solution branches that appear when determining the refractive index $\tilde{n}$ by comparison to experimental measurements. Three solution sets are shown, one for a smooth sample, one for a rough sample, and one for a rough sample with surface roughness included in the model. The green symbols represent the extracted physically meaningful solution.

need to be the n and k of the thin film (assuming air above and below). Using the S matrix method the reflection and transmission (R_{sim} and T_{sim}) can be obtained from the thin film. These can be compared to the reflection and transmission measured from an actual sample of the material (R_{exp} and T_{exp}). By varying the real and imaginary parts of the permittivity of the film in the simulation until the R and T match those obtained in the experiment, we can determine the refractive index of the thin film

$$\text{find } n \text{ and } k \text{ such that } |R_{exp} - R_{sim}(n,k)| + |T_{exp} - T_{sim}(n,k)| \to 0. \tag{A.1}$$

Practically speaking, we use a minimisation routine that minimises the difference between the experimental and simulated reflection and transmission by varying n and k.

This is repeated at each wavelength in order to obtain the wavelength dependent response. The drawback to this method is that the solution to equation A.1 is not unique, there may be mathematically many different solutions for n and k at a certain wavelength, while only one of them is physically reasonable. It is not possible beforehand to know which solution is the physically correct one. In order to select the correct solution, we first compute all the solutions for each wavelength and then select those which appear physically reasonable. Figure A.1 shows the complicated nature of the pattern of solutions for the n value of a CGSe layer, taken from [72]. Although many solution branches exist with a strong anomalous dispersion, the weak normal dispersion of the central line which is highlighted with green symbols is clearly the physical n value. The green symbols also represent the extracted values for the n value, note that at certain wavelengths, the extracted values do not overlap with any of the values determined by the minimisation routine. These so called branch gaps appear at extrema of Fabry-Perot resonances where the model fits particularly poorly due to sample imperfections being magnified by multiple internal reflections. However we assume that the real n value is a function which varies slowly with wavelength, therefore interpolating the physical n value in these regions between two different regions where the model fits well. The criteria used to select the correct solutions can be summarised as,

- Those solutions which give the refractive index in the correct magnitude (e.g. the refractive index for CIGSe may be between 2.7 and 3.0, but it cannot be 0.8 or 6.8).
- Normal dispersion away from resonances (i.e. if the k value is zero, the n value should show normal dispersion).
- k begins to increase at a wavelength around the band gap if the band gap is known.

We developed a unique interface in which the originally calculated n and k solutions are plotted and a user may place nodes directly on the graph in order to choose the correct n and k data. Using this interface the physical complex refractive index (equivalent to the permittivity) can be extracted quickly and easily.

Another factor which should be considered is that this method relies on having both the reflection and the transmission from the layer. If the layer is absorbing and all of the light is absorbed resulting in zero transmission, this method will not give accurate results for the refractive index. This can be remedied by either fabricating ultra-thin samples in order to reduce the absorption, or by using the method of spectroscopic ellipsometry. Ellipsometry measures the phase and amplitude of the reflected beam, therefore only reflection is required to obtain the refractive index. The ability to fit ellipsometric measurements has also been implemented into the available program.

A.2 Substrate

In reality a thin film is always supported by a substrate. The method we have presented for determining the refractive index of a layer can only work for a single unknown layer. However arbitrarily many other layers may be included as long as their refractive index is already known. Therefore the process involved in obtaining the refractive index of a thin film is thus:

- Measure R and T for a bare transparent substrate (e.g. glass).
- Use equation A.1 to determine n and k for the substrate.
- Deposit the thin film onto the substrate.
- Measure R and T for the thin film on the transparent substrate.

Using this process, the refractive index of layers integrated into a multilayer stack (which may be different to the layers isolated from other layers) can be determined. for more information on this process we refer the reader to our previous publication on the topic [73].

A.3 Surface Roughness

When light propagation through a layered stack is calculated analytically, it is assumed that the interfaces between layers are perfectly flat. In reality a certain amount of surface roughness is usually unavoidable. This surface roughness will tend to scatter the light which will affect the R and T spectra. If the model does not take this light scattering into account then an incorrect value for the refractive index will be obtained. To take the light scattering into account we use the scalar scattering theory. This theory assumes that the surface roughness height distribution is a random process that can be described analytically. Typically a Gaussian distribution is used. Furthermore we assume that the gradient of height distribution is small, i.e. that the surface roughness is small compared to the wavelength, this justifies the use of a scalar theory of diffraction [74]. In this case the Fresnel coefficients (r_{12},r_{21},t_{12} and t_{21}) for reflection and transmission at an interface between layers with subscripts one and two can be replaced by the following terms [72]

$$r'_{12} = r_{12}\mathrm{exp}\left(-2\left[\frac{2\pi n_1\sigma}{\lambda}\right]^2\right), \tag{A.2}$$

$$r'_{21} = r_{21}\mathrm{exp}\left(-2\left[\frac{2\pi n_2\sigma}{\lambda}\right]^2\right), \tag{A.3}$$

$$t'_{12} = t_{12}\mathrm{exp}\left(-\frac{1}{2}\left[\frac{2\pi(n_1 - n_2)\sigma}{\lambda}\right]^2\right), \tag{A.4}$$

$$t'_{21} = t_{21}\mathrm{exp}\left(-\frac{1}{2}\left[\frac{2\pi(n_2 - n_1)\sigma}{\lambda}\right]^2\right). \tag{A.5}$$

$$\tag{A.6}$$

Where n_1 and n_2 are the real parts of the refractive index of layers one and two, σ is the root mean square (rms) roughness at the interface and λ is the wavelength. This models the loss of light from the specular reflection/direct transmission which will be present instead as diffuse reflection and transmission or trapped/absorbed inside the layered stack. Therefore it is important to compare the values of R and T calculated using these modified coefficients to measurements of the specular reflection and direct transmission, instead of the total values.

A.4 Inhomogeneous Layers

The simple analytical expression for the scattering of light given in the previous section allows for rapid calculation of light propagation in the presence of surface roughness. We turn now to the problem of internal roughness, if a layer has voids or inclusions of another material inside it, this violates the assumption present in the S matrix method that the layers are homogeneous. One method to deal with this problem is to assume an effective medium, one which has a permittivity based on the permittivities of the host and inclusion. This approach was not applicable for the samples investigated in the current work due to the following reasons,

- Effective medium is fully coherent, it does not take into account the partial coherency caused by scattering of light from the voids.

- Effective medium changes the host n value to the effective n value which will change the peak positions of Fabry-Perot oscillations. In fact we do not expect these peak positions to shift compared to a homogeneous medium, since light does

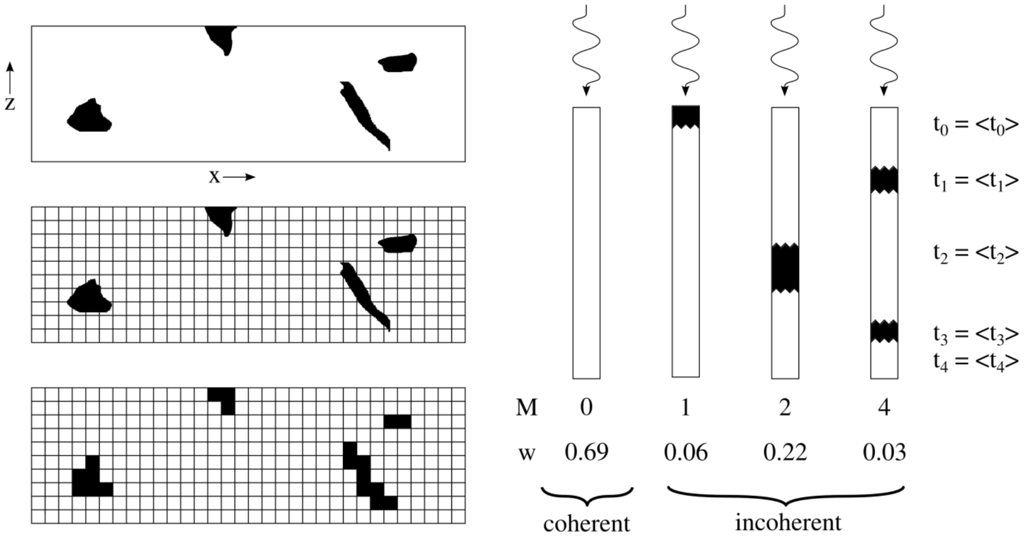

FIGURE A.2: Schematic image of the method for simulating an inhomogeneous layer. Upper left shows an image of a possible void distribution viewed in the x-z plane. The two images underneath show how this distribution is then discretised onto a rectangular grid. Each unique column of the grid must then be simulated via scattering matrix simulations. The voids are included as separate layers with rough interfaces modelled using the scalar scattering theory.

not travel through the voids but is scattered by them, meaning that the n value determined from the peak positions should be the homogeneous one.

Due to this a method needs to be developed which can take these factors into account. Rigorous simulation of light propagation in an inhomogeneous sample would be preferable, however given the fact that during minmisation process, the reflection and transmission will be calculated hundreds of times per wavelength with different refractive index values in the inhomogeneous film, rigorous approaches are not applicable in this case due to the extremely slow speed compared to analytical techniques. Therefore we seek an analytical technique that can simulate the light propagation in inhomogeneous thin films.

We consider a thin film which is extended in the x-y plane, light will be normally incident to the film in the z direction. The distribution of voids in a 2D slice in the x-z plane is shown in the upper left of fig. A.2. This distribution is then discretised onto a rectangular grid with the process of discretisation shown in the two images underneath. Each column of the final discretised distribution is then extracted to be used as an S matrix simulation. A key distinction may now be drawn between the columns with the presence of voids and those without. The columns that do not contain voids are treated normally as fully coherent simulations, however columns which do contain voids can be treated incoherently. This is because the scattering of the randomly positioned voids causes the light which interacts with the voids to become incoherent with respect to the

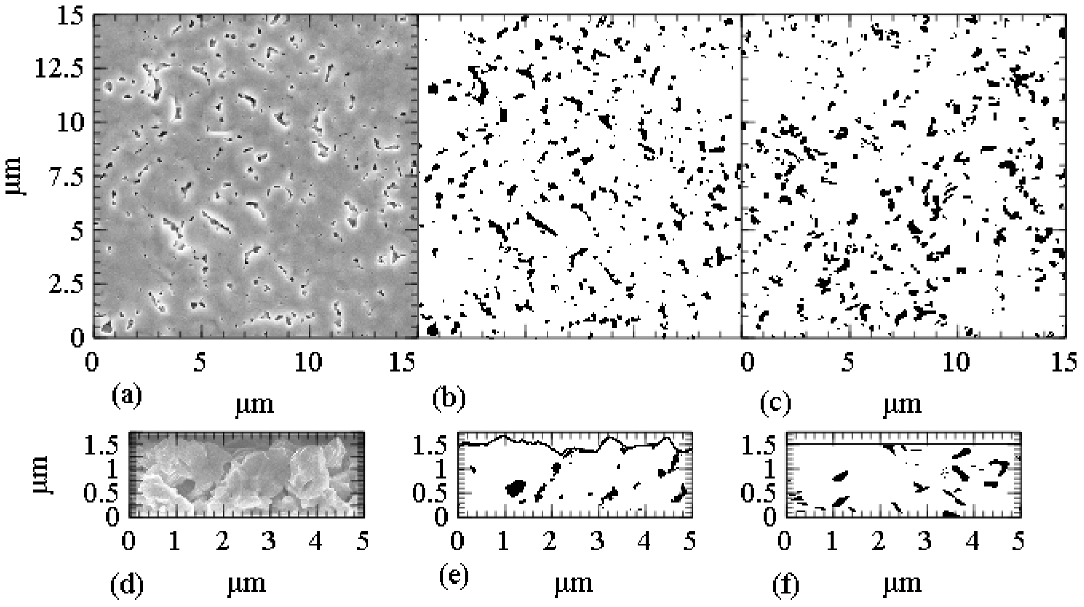

FIGURE A.3: The process of obtaining a statistical distribution from SEM images of the sample. Part (a) shows the original SEM image of the top and side surfaces of a sample containing voids. Part (b) shows the same image with void regions identified in black and all other regions in white, allowing for the statistical distribution to be measured via image analysis. Part (c) shows the top and side surface taken from a 3D model which uses the same statistical distribution as obtained from part (b).

incident light. Due to this, it will not matter if a 1 μm film is divided into 300/200/500 film/void/film or 500/200/300 film/void/film, the end result will be the same due to the simulation being incoherent. Additionally the layered stack 400/200/400 film/void/film will also give the same result, this is because the total amount of film and void has been conserved. Therefore we only need to determine the average amount of film to void, or to put it another way, the average void size. Note that the layered stack 300/100/200/100/300 film/void/film/void/film would not give the same result, since the total amount of interfaces has not been conserved, and each interface brings significant losses due to scattering. Therefore we must perform one simulation for each number of interfaces (fig. A.2 shows the cases for 1, 2 and 4 interfaces) using the average layer thicknesses determined from the discretised grid, and weight each simulation by the total frequency with which that number of interfaces occurred, which is also extracted from the discretised grid. For more detailed information on the method we refer the reader to the relevant publication [75].

The void distribution inside the layer and also the roughness at void/film interfaces is given by a 3D model of the void distribution inside the layer, based on the distribution visible at the top and side surfaces. Figure A.3 shows the process of obtaining the statistical distribution from SEM images. Each part shows the top surface view above

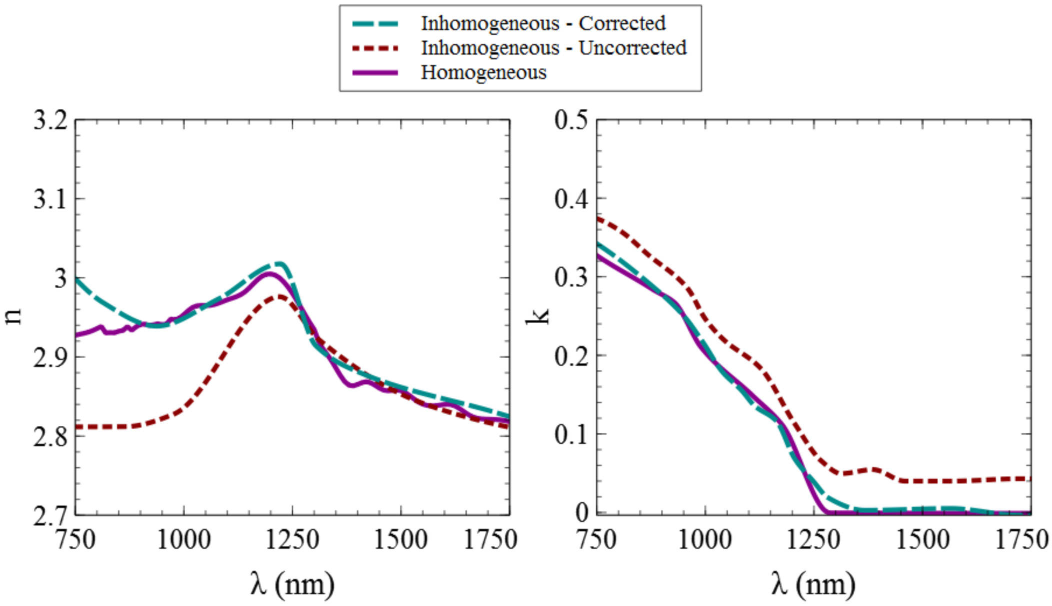

FIGURE A.4: The n (left) and k (right) value extracted from experimental measurements of reflection, transmission and absorption of a thin film sample. For each value three different results are shown, the values obtained from a homogeneous sample (homogeneous), the values for the inhomogeneous sample of the same material using standard methods (uncorrected) and the values for the inhomogeneous sample of the same material using the method presented here (corrected).

with the side surface view below. Part (a) shows an unmodified SEM image of the experimental sample. Part (b) shows the result of image analysis applied to the image in part (a). A threshold technique for the pixel brightness is used in order to determine the areas containing voids which are shown in black. From this an edge finding algorithm can determine the size shape and orientation of the void slices present. These can then be binned into a parameter range producing a histogram. The histogram can then be fitted by a statistical distribution. The distribution is then used to generate an artificial surface which is statistically similar to the experimental one which is shown in part (c).

The total 3D distribution must also be constructed in order to obtain the required void distribution inside the thin film. Constructing this 3D distribution is typically the most time consuming step in the simulation process, depending on the fraction of voids present. However this step typically takes only a few minutes and is therefore still quicker than rigourous methods. Additionally this step must only be performed once before any S matrix simulations. That means that the speed of determining the refractive index of materials is not significantly reduced when using this method.

A comparison of this model to standard methods can be seen in fig. A.4. Here we plot the results of the n and k value of a thin film layer determined using the method described in section A.1. Firstly the results for a homogeneous film are shown, these results are taken as the reference for the inhomogeneous sample. The inhomogeneous sample has an almost identical chemical composition to the homogeneous one, therefore it is assume that the refractive index of the crystal itself is identical to the homogeneous case. Using the standard methods where we only take into account the front surface roughness, we see a large difference between the n and k values of the homogeneous and inhomogeneous samples. The inhomogeneous sample predicts a higher k value at all wavelengths, even for wavelengths below the band gap. This is because light which has been scattered by the voids will not reach the transmission detector meaning that less light is detected. The standard method interprets this as absorption meaning a higher k value. Secondly the n value in the spectral region 750-1250 nm is underestimated compared to the homogeneous case. This is because the reflection of the experimental sample is reduced in this region due to scattering from voids at or near the surface. The standard approach interprets the reduction in reflection as a lower n value. In the transparent spectral region (>1250 nm) this effect is not pronounced, this is because the n value is more strongly determined by the period of Fabry-Perot oscillations in the sample than for the total reflection values. These oscillations are not present when the film is absorbing because no light is able to reflect from the rear side due to high absorption. The period of these oscillations will agree with the homogeneous case since only light which did not hit a void will contribute to the Fabry-Perot oscillation (void scattering makes the light incoherent with the incident light), therefore the reflected light which contributes to the oscillations only sees the homogeneous parts of the sample.

The final set of results shown in fig. A.4 are the n and k values determined using the model for inhomogeneous layers presented in this chapter. By using this model we obtain n and k values much closer to the homogeneous values. This is because the optical effect of void scattering is directly included in the model. This reduces the overall transmission, meaning that the k value agrees with the homogeneous case and it reduces the reflection in the absorption region which gives good agreement with the homogeneous case. In the short wavelength region the homogeneous and corrected inhomogeneous cases start to differ in n value. This could be due to the scalar scattering theory breaking down since the size of the voids is becoming comparable to the wavelengths of light incident onto them. However as long as the scalar scattering theory remains valid, this approach is able to correctly determine the refractive index of inhomogeneous materials.

Bibliography

[1] T.A. Boden, G. Marland, and R.J. Andres. Global, regional, and national fossil-fuel CO_2 emissions. Technical report, Carbon Dioxide Information Analysis Center, Oak Ridge National Laboratory, U.S. Department of Energy, Oak Ridge, Tenn., U.S.A, 2011.

[2] J. Hansen, R. Ruedy, M. Sato, and K. Lo. Global surface temperature change. *Rev. Geophys.*, 48:RG4004, 2010.

[3] P. Campbell and M. A. Green. Light trapping properties of pyramidally textured surfaces. *J. App. Phys.*, 62:243, 1987.

[4] F. R. S. Rayleigh. Polish. *Nature*, 64:385, 1901.

[5] T. K. Chinmayanandam. On the specular reflection from rough surfaces. *Phys. Rev.*, 13:96, 1919.

[6] H. Davies. The reflection of electromagnetic waves from a rough surface. In *Proceedings of the IEE - Part IV: Institution Monographs*, volume 101, page 209, 1954.

[7] P. Beckmann and A. Spizzichino. *The scattering of electromagnetic waves from rough surfaces*. Artech Print, 1987.

[8] B. Harbecke. Coherent and incoherent reflection and transmission of multilayer structures. *Appl. Phys. B-Photo.*, 39:165, 1986.

[9] J. Müller, B. Rech, J. Springer, and Vanecek M. TCO and light trapping in silicon thin film solar cells. *Sol. Energy*, 77:917, 2004.

[10] O. Kluth, B. Rech, L. Houben, S. Wieder, G. Schöpe, C. , Beneking, H. Wagner, A. Löffl, and H.W. Schock. Texture etched ZnO:Al coated glass substrates for silicon based thin film solar cells. *Thin Solid Films*, 351:247, 1999.

[11] K. Yamamoto, A. Nakajima, M. Yoshimi, T. Sawada, S. Fukuda, T. Suezaki, M. Ichikawa, Y. Koi, M. Goto, T. Meguro, T. Matsuda, M. Kondo, T. Sasaki, and Y. Tawada. A high efficiency thin film silicon solar cell and module. *Sol. Energy*, 77:939, 2004.

[12] E. A. Schiff. Thermodynamic limit to photonic-plasmonic light-trapping in thin films on metals. *J. App. Phys.*, 110:104501, 2011.

[13] T. Söderström, F.-J. Haug, X. Niquille, V. Terrazzoni, and C. Ballif. Asymmetric intermediate reflector for tandem micromorph thin film silicon solar cells. *App. Phys. Lett.*, 94:063501, 2009.

[14] D. Dominé, P. Buehlmann, J. Bailat, A. Billet, A. Feltrin, and Ballif C. Optical management in high-efficiency thin-film silicon micromorph solar cells with a silicon oxide based intermediate reflector. *Phys. Stat. Sol. (RRL)*, 2:163, 2008.

[15] L.V. Mercaldo, P. Delli Veneri, E.M. Esposito, and G. Fameli. Micro-raman investigation of silicon nitride embedding Si nanostructures. In *25th European Photovoltaic Solar Energy Conference / 5th World Conference on Photovoltaic Energy Conversion*, 2008.

[16] F.-J. Haug, M. Boccard, R. Biron, B. Niesen, M. Despeisse, and C. Ballif. Advanced intermediate reflector layers for thin film silicon tandem solar cells. In *Photovoltaic Specialists Conference (PVSC), 2013 IEEE 39th*, page 0914, 2013.

[17] V. E. Ferry, M. A. Verschuuren, H. B. T. Li, E. Verhagen, R. J. Walters, R. E. I. Schropp, H. A. Atwater, and A. Polman. Light trapping in ultrathin plasmonic solar cells. *Opt. Express*, 18:A237, 2010.

[18] U. Palanchoke, V. Jovanov, H. Kurz, P. Obermeyer, H. Stiebig, and D. Knipp. Plasmonic effects in amorphous silicon thin film solar cells with metal back contacts. *Opt. Express*, 20:6340, 2012.

[19] Z. Yu, A. Raman, and S. Fan. Fundamental limit of light trapping in grating structures. *Opt. Express*, 18:A366, 2010.

[20] Z. Yu, A. Raman, and S. Fan. Thermodynamic upper bound on broadband light coupling with photonic structures. *Phys. Rev. Lett.*, 109:173901, 2012.

[21] C. Battaglia, C.-M. Hsu, K. Soöderstroöm, J. Escarre, F.-J. Haug, M. Charriere, M. Boccard, M. Despeisse, D. T. L. Alexander, M. Cantoni, Y. Cui, and C. Ballif. Light trapping in solar cells: Can periodic beat random? *ACS Nano*, 6:2790, 2012.

[22] S. Solntsev and M. Zeman. Optical modeling of thin-film silicon solar cells with submicron periodic gratings and nonconformal layers. In *Energy Proceedia*, volume 10, page 308, 2011.

[23] K. Q. Le, A. Abass, B. Maes, P. Bienstman, and A Alù. Comparing plasmonic and dielectric gratings for absorption enhancement in thin-film organic solar cells. *Opt. Express*, 20:A39, 2012.

[24] J. N. Munday, D. M. Callahan, and H. A. Atwater. Light trapping beyond the $4n^2$ limit in thin waveguides. *Appl. Phys. Lett.*, 100(12):121121/1, 2012.

[25] D. M. Callahan, J. N. Munday, and H. A. Atwater. Solar cell light trapping beyond the ray optic limit. *Nano. Lett.*, 12(1):214, 2012.

[26] E. Garnett and P. Yang. Solar cell light trapping beyond the ray optic limit. *Nano Lett.*, 10:1082, 2010.

[27] M. Yao, N. Huang, S. Cong, C.-Y. Chi, M. Ashkan Seyedi, Y.-T. Lin, Y. Cao, Povinelli. M. L., P. D. Dapkus, and C. Zhou. Gaas nanowire array solar cells with axial p–i–n junctions. *Nano. Lett.*, 14(6):3293, 2014.

[28] E. R. Martins, J. Li, Y. Liu, J. Zhou, and T. F. Krauss. Engineering gratings for light trapping in photovoltaics: The supercell concept. *Phys. Rev. B*, 86:041404, Jul 2012.

[29] H. Ding, L. Lalouat, B. Gonzalez-Acevedo, A. Harouri, and R. Orobtchouk. Pseudodisordered structures for light trapping improvement in mono crystalline Si thin films. In *Photovoltaic Technical Conference - Advanced Materials and Processes to Innovative Applications*, 2015.

[30] H. A. Atwater and A. Polman. Plasmonics for improved photovoltaic devices. *Nat. Mater.*, 9:205, 2010.

[31] K. R. Catchpole and A. Polman. Plasmonic solar cells. *Opt. Express*, 16(26):21793, 2008.

[32] K. R. Catchpole and A. Polman. Design principles for particle plasmon enhanced solar cells. *Appl. Phys. Lett.*, 93(19):191113/1, 2008.

[33] M. L. Brongersma, Y. Cui, and S. Fan. Light management for photovoltaics using high-index nanostructures. *Nat. Mater.*, 13(5):451, 2014.

[34] P. Spinelli, M. A. Verschuuren, and A. Polman. Broadband omnidirectional antireflection coating based on subwavelength surface Mie resonators. *Nat. Commun.*, 3: 692, 2012.

[35] A. I. Kuznetsov, A. E. Miroshnichenko, Y. H. Fu, J. Zhang, and B. Luk'yanchuk. Magnetic light. *Sci. Rep.*, 2:492, 2012.

[36] H. Tan, R. Santbergen, A. H. Smets, and M. Zeman. Plasmonic light trapping in thin-film silicon solar cells with improved self-assembled silver nanoparticles. *Nano. Lett.*, 12(8):4070, 2012.

[37] E. Moulin, J. Sukmanowski, P. Luo, R. Carius, F. X. Royer, and H. Stiebig. Improved light absorption in thin-film silicon solar cells by integration of silver nanoparticles. *J. Non-Cryst. Solids*, 354(19):2488, 2008.

[38] James R. Nagel and Michael A. Scarpulla. Design principles for light trapping in thin silicon films with embedded dielectric nanoparticles. *Prog. Photovoltaics Res. Appl.*, 21(3):319, 2013.

[39] N. Kalfagiannis, P. G. Karagiannidis, C. Pitsalidis, N. T. Panagiotopoulos, C. Gravalidis, S. Kassavetis, P. Patsalas, and S. Logothetidis. Plasmonic silver nanoparticles for improved organic solar cells. *Sol. Energ. Mat. Sol. C.*, 104:165, 2012.

[40] G. Mie. Beiträge zur Optik trüber Medien speziell kolloidaler Goldlösungen. *Ann. Phys.*, 25:377, 1908.

[41] C. F. Bohren and D. R. Huffmann. *Absorption and Scattering of Light by Small Particles.* Wiley, 1998.

[42] B. J. Messinger, K. Ulrich von Raben, R. K. Chang, and P. W. Barber. Local fields at the surface of noble-metal microspheres. *Phys. Rev. B*, 24:649, 1981.

[43] J. D. Jackson. *Classical Electrodynamics.* Wiley, 3rd edition, 1998.

[44] C. Kittel. *Introduction to Solid State Physics.* Wiley, 8th edition, 2004.

[45] S. Maier. *Plasmonics: Fundamentals and Applications.* Springer, 2007.

[46] D. W.. Juenker, L. J. LeBlanc, and C. R. Martin. Optical properties of some transition metals. *J. Opt. Soc. Am.*, 58:164, 1967.

[47] P. R. West, S. Ishii, G. V. Naik, N. K. Emani, V. M. Shalaev, and A. Boltasseva. Searching for better plasmonic materials. *Laser Photonics Rev.*, 4(6):795, 2010.

[48] V. Myroshnychenko, J. Rodrıguez-Fernandez, I. Pastoriza-Santos, A. M. Funston, C. Novo, P. Mulvaney, L. M. Liz-Marzan, and F. Javier Garcıa de Abajo. Modelling the optical response of gold nanoparticles. *Chem. Soc. Rev.*, 37:1792, 2008.

[49] D. D. Jr. Evanoff and G. Chumanov. Synthesis and optical properties of silver nanoparticles and arrays. *Chemphyschem*, 6(7):1221, 2005.

[50] M. D. Brown, T. Suteewong, R. S. Kumar, V. D'Innocenzo, A. Petrozza, M. M. Lee, U. Wiesner, and H. J. Snaith. Plasmonic dye-sensitized solar cells using core-shell metal-insulator nanoparticles. *Nano. Lett.*, 11(2):438, 2011.

[51] C. Clavero. Plasmon-induced hot-electron generation at nanoparticle/metal-oxide interfaces for photovoltaic and photocatalytic devices. *Nat. Photonics*, 8:95, 2014.

[52] W. L. Liu, F. C. Lin, Y. C. Yang, C. H. Huang, S. Gwo, M. H. Huang, and J. S. Huang. The influence of shell thickness of Au@TiO_2 core–shell nanoparticles on the plasmonic enhancement effect in dye-sensitized solar cells. *Nanoscale*, 5:7953, 2013.

[53] S. D'Addato, D. Pinotti, M. C. Spadaro, G. Paolicelli, V. Grillo, S. Valeri, L Pasquali, Bergamini L., and S. Corni. Influence of size, shape and core–shell interface on surface plasmon resonance in Ag and Ag@MgO nanoparticle films deposited on Si/SiO_x. *Beilstein J. Nanotechnol.*, 6:404, 2015.

[54] Q. Xu, F. Liu, W. Meng, and Y. Huang. Plasmonic core-shell metal-organic nanoparticles enhanced dye-sensitized solar cells. *Opt. Express*, 20(S6):A898, 2012.

[55] D. Qu, F. Liu, J. Yu, W. Xie, Q. Xu, X. Li, and Y. Huang. Plasmonic core-shell gold nanoparticle enhanced optical absorption in photovoltaic devices. *Appl. Phys. Lett.*, 98(11):113119/1, 2011.

[56] P. Monk. *Finite Element Methods for Maxwell's Equations.* Oxford University Press, 2003.

[57] J. Pomplun, S. Burger, L. Zschiedrich, and F. Schmidt. Adaptive finite element method for simulation of optical nano structures. *phys. status solidi (b)*, 244(10): 3419, 2007.

[58] J. Berenger. *Perfectly Matched Layer (PML) for Computational Electromagnetics.* Morgan & Claypool, 2007.

[59] C. A. Schneider, W. S. Rasband, and K. W. Eliceiri. NIH image to ImageJ: 25 years of image analysis. *Nat. Meth.*, 9(7):671, 2012.

[60] H. M. Reid. *Introduction to Statistics: Fundamental Concepts and Procedures of Data Analysis.* SAGE, 2013.

[61] M. Schmid, R. Klenk, M. Ch. Lux-Steiner, M. Topic, and J. Krc. Modeling plasmonic scattering combined with thin-film optics. *Nanotechnology*, 22(2):025204/1, 2011.

[62] R. Santbergen, S. Solntsev, and M. Zeman. Modelling plasmonic solar cells. *Proceedings of EU PVSEC*, 25th European Photovoltaic Solar Energy Conference:533, 2010.

[63] R. C. Rumpf. Improved formulation of scattering matrices for semi-analytical methods that is consistent with convention. *Prog. Electromagn. Res. B.*, 35:241, 2011.

[64] R. Santbergen, A. H. M. Smets, and M. Zeman. Optical model for multilayer structures with coherent, partly coherent and incoherent layers. *Opt. Express*, 21: A262, 2013.

[65] J. S. C. Prentice. Coherent, partially coherent and incoherent light absorption in thin-film multilayer structures. *J. Phys. D Appl. Phys.*, 33:3139, 2000.

[66] M. C. Troparevsky, A. S. Sabau, A. R. Lupini, and Z. Zhang. Transfer-matrix formalism for the calculation of optical response in multilayer systems: from coherent to incoherent interference. *Opt. Express*, 18(24):24715, 2010.

[67] J. Nelson. *The Physics of Solar Cells.* Imperial College Press, 2003.

[68] J. Kaneshiro, N. Gaillard, R. Rocheleau, and E. Miller. Advances in copper-chalcopyrite thin films for solar energy conversion. *Sol. Energ. Mat. Sol. C.*, 94 (1):12, 2010.

[69] R. Klenk. Characterisation and modelling of chalcopyrite solar cells. *Thin Solid Films*, 387:135, 2001.

[70] M. Sever, B. Lipovsek, J. Krc, A. Campa, G. S. Plaza, F.-J. Haug, M. Duchamp, W. Soppe, and M. Topic. Combined model of non-conformal layer growth for accurate optical simulation of thin-film silicon solar cells. *Sol. Energ. Mat. Sol. C.*, 119:59, 2013.

[71] F. Magoules. *Mesh Partitioning Techniques and Domain Decomposition Methods.* Saxe-Coburg, 2007.

[72] G. Yin, C. Merschjann, and M. Schmid. The effect of surface roughness on the determination of optical constants of $CuInSe_2$ and $CuGaSe_2$ thin films. *J. Appl. Phys.*, 113(21):213510/1, 2013.

[73] G. Yin, P. Manley, and M. Schmid. Influence of substrate and its temperature on the optical constants of $CuIn_{1-x}Ga_xSe_2$ thin films. *J. Phys. D Appl. Phys.*, 47(13): 135101, 2014.

[74] C. K. Carniglia. Scalar scattering theory for multilayer optical coatings. *Opt. Eng.*, 18(2):104, 1979.

[75] P. Manley, G. Yin, and M. Schmid. A method for calculating the complex refractive index of inhomogeneous thin films. *J. Phys. D Appl. Phys.*, 47(20):205301, 2014.